MPhil Thesis

Development of novel 3D model of motor neuron disease (MND) by use of aligned polymer fibre scaffolds

by Candy Ho
Material Science and Engineering

Development of novel 3D model of motor neuron disease (MND) by use of aligned polymer fibre scaffolds

(MPhil Report)

Candy Ho

Material Science and Engineering

Supervisors:
Dr. Ke Ning (SITraN),
Prof. John W. Haycock (KRI)
and Prof. Pamela J. Shaw (SITraN)

Acknowledgements

I wish to thank all my supervisors, Prof John W. Haycock (Kroto), Dr Ke Ning (SITraN) and Prof Pamela J. Shaw (SITraN), for their patience and time with me. Thanks must also go to Dr Katie Smith (now in Barcelona), Dr Celia Murray-Dunning (Kroto) and Dr Adrian Higginbottom (SITraN) for helping me set-up the initial experiments and helping me get to grips with the biological aspects of the project. In addition, I am also in debt to Fauzi Daud (Kroto) and Ross Kaewkhaw (now in Maryland) for bits of help and advice here and there and also to Juliet Bell (Kroto), Frazer Bye (Kroto), Amanda Harvey (Chemistry) and Christopher Pateman (Kroto) for lending me their time to bounce ideas with. Lastly, I must also thank Dr Peter Monk (Department of Infection and Immunity) without whom this project would not have been in existence.

Abstract

Background Motor Neuron Disease (MND) is a group of complex neurodegenerative disorders that affects primarily the motor functions. Current limitation of existing MND models are either their ability to replicate *in vivo* architecture/cell-cell interactions or to be of the relevant species to enable better translation of laboratory results towards the clinic.

Aims In order to improve transferability of laboratory results, this project aims to develop an alternative *in vitro* bioengineered three-dimensional motor neuron disease model. Electrospun aligned ultrafine fibre scaffolds have previously been shown to encourage axon alignment and elongations with submicron fibres found to be the best. The application of these scaffolds would provide a good foundation in the development of potential *in vitro* human MND models.

Results NSC34 cells cultured on a range of both micro- and nanofibre scaffolds identified nanofibres to be best at supporting neurite differentiation and growth. Subsequent analyses via the use of primary murine spinal cord dissociates indicated good association between neurons and glia akin to natural nervous tissue. However, weak immunolabelling of astrocyte and oligodendrocyte markers (ALDH1L1 and MBP respectively) suggested that they were immature cells. Relatively consistent aligned submicron fibre scaffolds were found to be difficult to obtain. As a result, multivariate ANOVA was conducted on the recorded parameters against fibre diameter distributions to find a simpler method of controlling the electrospinning of submicron fibres. Using previously established mathematical models of electrospinning as a basis, it was possible to reduce the number of parameters from 11 measurable parameters to 5 composite parameters. However, it was also noted that it may be possible to decrease the number of parameters further.

Conclusions Aligned nanofibre scaffolds were found to be good at controlling the differentiation of NSC34 and primary murine spinal cord dissociates. In addition, using a theoretical approach to electrospinning it is possible to simplify the control of parameters in the generation of aligned submicron fibre scaffolds.

Abbreviations

αMN	alpha motor neurons
ALS	Amyotrophic Lateral Sclerosis
ALS-FTD	ALS-Frontotemporal Dementia
ALS/PDC	Amyotrophic Lateral Sclerosis / Parkinsonism Dementia Complex
AMPA	α-amino-3-hydroxy-5-methyl-4-isoxazolepropionic acid
ARE	Antioxidant Response Element
ATP	Adenosine triphosphate
BMAA	β-methylaminoalanine
CNS	Central Nervous System
CSF	Cerebrospinal Fluid
DAO	D-Amino Acid Oxidase
EAAC1	Excitatory Amino Acid Carrier 1
ECM	Extracellular Matrices
ESC	Embryonic Stem Cells
fALS	Familial Amyotrophic Lateral Sclerosis
FUS/TLS	Fused in Sarcoma/Translocated in Liposarcoma
γMN	Gamma Motor Neurons
GLAST	Glutamate Aspartate Transporter
GLT1	Glutamate Transporter 1
IVF	In Vitro Fertilization
iPSC	Induced Pluripotent Stem Cells
LMN	Lower Motor Neurons
MIS	Mitochondrial Intermembrane Space
MN	Motor Neurons
MND	Motor Neuron Disease
MSC	Mesenchymal Stem Cells
NFH	Heavy Neurofilament Subunit
NMJ	Neuromuscular Junctions
NO	Nitric Oxide
OPC	Oligodendrocyte Progenitor Cells
PCL	Polycaprolactone
PBP	Progressive Bulbar Palsy
PLLA	Poly-L-lactic acid
PLS	Primary Lateral Sclerosis
PMA	Progressive Muscular Atrophy
PNS	Peripheral Nervous System
PP	Pseudobulbar palsy
PPIs	Polyphosphoinositides
ROS	Reactive Oxygen Species
sALS	Sporadic Amyotrophic Lateral Sclerosis
SMA	Spinal Muscular Atrophy
SMN	Survival Motor Neuron protein
snRNPs	Small Nuclear Ribonucleoproteins
SOD	Superoxide Dismutase
SOD1	Cu-Zn Superoxide Dismutase
SOD2	Mn Superoxide Dismutase
TAR	TARDP encoding transactive response
TDP-43	TAR DNA-binding protein 43 kDa
UMN	Upper Motor Neurons
VAPB	Vesicle-Associated membrane Protein associated protein B
VCD	Volumetric Charge Density

Contents

1. Introduction

Motor Neuron Disease (MND) is a complex and incompletely understood group of neurodegenerative disorders affecting primarily the motor functions (muscular responses)[1,2]. At present, there are five main subgroups classified according to their site of onset with Amyotrophic Lateral Sclerosis (ALS) being the most predominant form; accounting for approximately 80% of all cases. Depending on the type of MND, patients are often diagnosed with presenting symptoms of muscle weakness, spasticity and decline in ability to carry out daily functions[3]. Survival of sufferers is typically in the range of 3-5 years from the onset of symptoms, with respiratory failure being the most common cause of mortality.

The motor system of any living organism is the response branch of their nervous network following external stimuli; such as the instant limb retraction following heat sensation. Due to the need for instantaneous reactions the motor system is evolutionarily developed to be highly receptive of signal transductions. However, this also results in a higher risk of neurodegeneration brought about by either physical trauma or disease.

The nervous system of higher order species is typically divided into the central and the peripheral nervous systems which comprise the brain and the spinal cord (CNS), and the nerve fibres and the ganglia (PNS), respectively. Although the maintenance strategies of both the CNS and PNS are relatively similar, the PNS is typically more capable of repair and/or regeneration following stress. However, in patients with MND the innate maintenance and repair/regeneration capabilities of the nervous system are compromised with the motor system particularly affected. Although the underlying causes are not completely understood, current knowledge derived from traditional model systems used in biological research (such as genetic screening, *in vitro*, *in vivo*, *ex vivo* and/or epidemiological models) point towards multiple factors contributing to motor neuron injury. The potential factors identified that can lead to MND include genetic mutations[4], mitochondrial dysfunction[5], glutamate excitotoxicity[6,7] and many more. However, current research has yet to provide transferability of laboratory results towards a positive clinical outcome.

Peripheral nerve regeneration is a developing branch within tissue engineering that focuses on the development of guidance conduits which aims to bridge the nerve gaps generated following trauma. This is achieved by the development of materials and

constructs that can induce and enhance the natural features of native PNS regeneration. Microporous sponges[8] or collagen hydrogels[9] are some of the materials that are being used to mimic natural three-dimensional structures within which neurites normally reside. Although these structures lack directional control, small tubular conduits[10] have been developed to be of similar dimensions and morphologies to the extracellular matrices of natural nerve fibres to support the repair of nerve gaps of up to 25 mm. Minor improvements[11,12] to the regenerative potential of tubular constructs have been obtained by modifications such as the incorporation of microchannels[13] or the use of aligned microfibers[14,15] wrapped within a spongy fabric[16].

A major limitation to the transferability of laboratory results towards the clinic is sometimes attributed to the predominant use of animal models. The inherent species differences of such models restricts their ability to replicate human MND pathophysiology. In addition, with the advances made in the generation of patient-derived functional human motor neurons[17] there are increasingly vociferous calls for the reduced use of animal models. In previous years, this may have been hindered by the technologies available to establish structural characteristics of *in vitro* models akin to native neural tissues. However, given the progress made in peripheral nerve regeneration, there is potential for the development of an *in vitro* neural tissue model for the study of human MND.

1.1. Motor Neuron Disease

Motor neuron disease (MND) is a group of neurodegenerative disorders characterized by the selective loss of motor neurons with minimal deficits towards any other physiological functions[1,2,3]. The principle form of MND is amyotrophic lateral sclerosis (ALS), accounting for approximately 80% of all cases. Alternative forms of MND are identified by their site of onset or the affected subsets of motor neurons. An overview of what is currently known about MND is given below.

1.1.1. Motor Neurons

Classic features of MND are specific degeneration of motor neurons, which are one of the largest cells found within the human body. Motor neurons collectively form the bulk of the motor system and are responsible for relaying processed signals from the CNS allowing the brain to control movement by activation of skeletal muscle. Structurally, a single motor neuron is composed of dendrites, a soma, an axon and an axon terminus[18] (fig 1.1). The soma (or the cell body) is the principal site for protein syntheses in motor neurons and it is also where neuronal functions are predominantly regulated. They chiefly reside within the motor cortex, the motor nuclei of the brainstem and the ventral horns of the spinal cord along with the dendrites; whose function is to inflate the somatic membrane surface area for signal reception and processing. The axon on the other hand is responsible for signal filtering and the transmission of action potentials from the soma towards muscle targets[19]. There, axonal termini branch into structures known as end-plates which are dispersed throughout muscle fibres making synaptic contact with muscle fibres at the neuromuscular junction (NMJ).

The structure of motor neurons, like most other neurons, is maintained by a framework of actin, microtubules and neurofilaments. During development, actin reorganisation at growth-cones following environmental cues and inter-neurite (a generic term identifying neuronal processes) competition results in neuronal polarity (differentiation of neurites into dendrites and axon)[20]. The mature neuronal microarchitecture of microtubules and neurofilaments acts as the exchange framework for proteins, vesicles and mitochondria between and within the different neuronal compartments for normal motor neuron function[21]. In addition, actin filaments

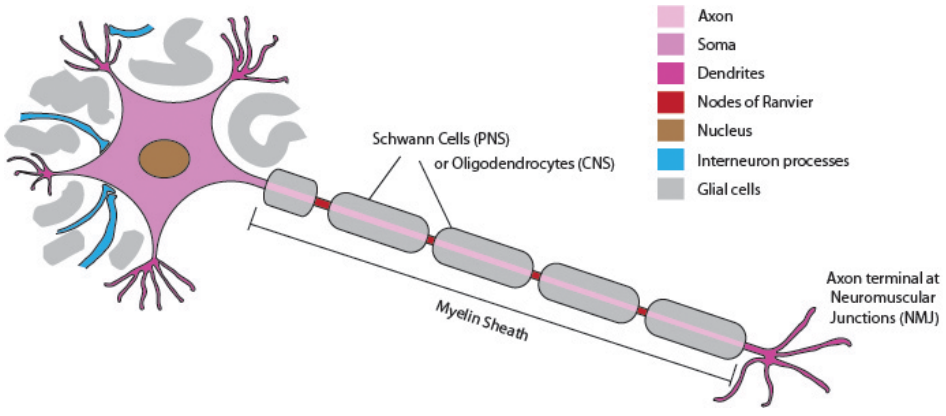

Figure 1.1: A Motor Neuron as can be found in the Nervous system

are involved in homeostatic regulation of motor neurons as well as their dynamic reorganisation of neuronal structure in response of stress[22,23].

In motor neurons an action potential is typically initiated following the activation of post-synaptic α-amino-3-hydroxy-5-methyl-4-isoxazolepropionic acid (AMPA)-kainate glutamate receptors[24] and/or the N-methyl-D-aspartate (NMDA) receptors[25] distributed about the dendrites or soma[18]. AMPA receptors of motor neurons predominantly lack the glutamate receptor-2 (GluR2) subunit which significantly increases the rapid influx of Ca^{2+} ions into the motor neuron soma following AMPA receptor activation. This influx of ions leads to a change in local membrane potential[26] which facilitates the opening of the voltage-dependent ion channels to enhance the exchange of Na^{+}, K^{+} and Cl^{-} ions. When the degree of depolarisation reaches a threshold an ionic current is driven across the soma and down the axon towards the axonal terminus[27]; thus forming the action potential. When the ionic current reach the nerve terminus it stimulates the exocytosis of the neurotransmitter acetyl choline into the synaptic cleft of specialised synapses known as neuromuscular junctions (NMJ). The transmission is complete when sufficient receptors in the post-synaptic muscle membrane have been activated to induce muscle contraction[28].

Motor neurons are classified into either the visceral or somatic subclasses depending on their function. Visceral motor neurons either directly innervate branchial muscles (which support the face and neck muscles in land vertebrates) or indirectly to cardiac and smooth muscles (e.g. for the involuntary control of blood circulation and the gastrointestinal tract). However, it is the somatic motor neurons that degenerate in MND patients. These neurons principally control skeletal movements and there are two main types: the upper and lower motor neurons[18,29]. Upper motor neurons are found in the CNS; the cell bodies are located within the motor cortex of the brain. They collectively direct the activation of lower motor neurons and the acquisition of new motor skills.

The other somatic neurons, lower motor neurons, can be found within the brainstem and the ventral horn of the spinal cord with extension of axons into the peripheral nervous system. Lower motor neurons directly innervate myofibres (the microstructures responsible for muscle contraction) via the NMJ[29]. These neurons can be further divided into alpha (αMN) or gamma motor neurons (γMN). The αMN innervates the extrafusal (contracting) myofibres for slow muscle contractions normally associated with voluntary movements. The γMN, on the other hand, innervates the intrafusal

(sensing) fibres within muscle spindles that are responsible for rapid involuntary stretch reflexes and muscle tone.

1.1.2. Neuroglia (otherwise known as Glia)

Neuroglia (or simply glia) are a group of cells found within the nervous system that support and regulate neural functions. During embryogenesis they appear after the generation of neurons following the closing of the neural tube in higher vertebrates. Their specific roles include electrical insulation for action potentials, protection against pathogens and toxins, regulation of homeostasis and of free neurotransmitters plus many more[30]. Astrocytes, oligodendrocytes and Schwann cells are the primary glia directly associated with the survival and functions of motor neurons.

Astrocytes are the most abundant glia found within the CNS and their most well-known role is in the regulation of CNS homeostasis[31] in support of neuronal survival[32]. In addition, they have been found to be involved in the maturation of neurofilaments[33], stimulation of synaptic formation[34] and in the regulation of the excitatory amino acid glutamate[7]. The full extent of astrocytic involvement in motor neuron survival and therefore MND will be discussed later.

Schwann cells and oligodendrocytes are the myelinating, or insulating, cells in the PNS and CNS respectively. Although derived from two different lineages[35] the respective functions of Schwann cells[36] and oligodendrocytes[37] are relatively similar. Apart from providing electrical insulation the process of myelination increases the level of phosphorylation of the dynamic neurofilaments[36]. This serves three principle roles: 1) to stabilise the neuronal architecture; 2) to increase the calibre of neurites; and 3) to aggregate ion channels thus driving the formation of nodes of Ranvier (features of mature axons). A stable neuronal architecture facilitates high efficiency and systematic intracellular molecular transportation[21]. A high calibre neurite increases its cross-sectional area which improves molecular transport and signal transmission[38]. Along with the formation of the nodes of Ranvier, these features of myelination collectively improve the conduction velocity of action potentials along neurites.

Another important function of myelinating glia is in neuroregeneration[39,40]. Between Schwann cells and oligodendrocytes, the former in peripheral nerve regeneration

is the better known. Assuming that CNS regeneration follows a similar pattern, neural regeneration following injury is initiated by the demyelination and degeneration of the distal ends of neurites, furthest away from the soma. This process releases a gradient of factors (chemotactic or chemical guidance) that guides the recruitment of macrophages or microglia to engulf and remove debris to leave behind an empty neural tract (for thigmotactic, or physical, guidance for nerve regeneration). At the same time, dormant glial progenitors are activated and guided towards the site of injury following similar chemotactic and thigmotactic cues. Whilst migrating, these glial progenitors secrete neurotrophic factors and extracellular matrix proteins that stimulate the formation of growth cones of regenerating neurites[41-43]. In healthy tissues this will result in the re-establishment of the neural network.

1.1.3. Clinical Features of Motor Neuron Disease

Motor neuron disease (MND) is an umbrella term for a group of neurodegenerative disorders affecting primarily motor neurons. Categorised according to the site of onset there are four main clinical subtypes: 1) primary lateral sclerosis; 2) progressive bulbar palsy; 3) progressive muscular atrophy and 4) amyotrophic lateral sclerosis (ALS).

Primary lateral sclerosis (PLS) is characterised by early upper motor neuron degeneration localised in the bilateral corticobulbar tracts (motor neuron clusters supplying the face, tongue, pharynx and larynx) and corticospinal tracts (that supply the body and limbs). Degeneration of upper motor neurons typically presents with muscle weakness associated with spasticity (muscle stiffness), hypertonia (increased muscle tone) and hyperreflexia (hyperactive reflexes).

Progressive bulbar palsy (PBP) describes MND caused by the degeneration of the branchial, visceral and lower motor neuron; localised within the cranial nerves, which control facial and neck muscle movements. Progressive muscular atrophy (PMA) on the other hand is characterised by degeneration of lower motor neurons in the spinal cord that supply the muscles in the rest of the human body. Degeneration of lower motor neurons is typically characterised by muscle wasting (atrophy), weakness and flaccidity. Muscle fasciculation (twitching) may also be observed.

Amyotrophic lateral sclerosis (ALS) is the most common form of MND. Sufferers

of ALS commonly show signs of degeneration of both upper and lower motor neurons. For an ALS classification the patients should exhibit early symptoms suggestive of α-motor neuron degeneration in the anterior (or ventral) horn of the spinal cord and in the motor cortex. Individuals presenting with the other clinical subtypes of MND will frequently show signs of ALS in the later stages due to the spread of neurodegeneration.

The aetiology of MND has yet to be completely understood. However, results from existing research are pointing towards a combination of various risk factors rather than a single cause that can eventually lead to MND. The predominant forms of MND are sporadic (non-familial) in nature while ~5% of cases are attributed to familial forms which, though heterogeneous, and better understood. An overview of the current understanding of the pathology and aetiology of MND is provided below.

1.1.4. Pathophysiology of Motor Neuron Disease

MND patients are often identified by an electromyographic assessment (a test of electrical activity as an indication of muscle health) showing features of denervation with fasciculation and enlargement of motor units[1]. Biopsies of wasted muscles from MND patients would present histological features of denervation with grouped atrophy of muscle fibres and thinning of the motor nerve roots. However, sensory nerve fibres and units would appear to be unaffected.

Major pathological features of post-mortem CNS tissues of MND patients are often shrinkage, sclerosis and pallor of the corticospinal tracts within the brain stem and the descending motor pathways of the spinal cord[44,45]. Atrophy of the precentral gyrus (part of the motor cortex) is also commonly seen in post-mortem MND brains[46]. In addition, significant increases in end-plate branching can be observed.

Histological examination of MND tissue samples frequently display a reduction of more than 50% of all spinal motor neurons. In addition, diffuse astrogliosis (excessive multiplication of astrocytes) are often observed within the grey matter of the spinal cord, motor cortex and the underlying subcortical white matter[47]. Surviving motor neurons in MND have been found to exhibit cytoplasmic protein aggregates which can be positively immunolabelled for ubiquitin[48,49]. These ubiquitinated inclusions are often positive for TAR DNA-binding protein 43 kDa (TDP-43)[49]. Alternatively, some histological samples

of MND cases display the presence of Lewy-like bodies which are fused with swollen mitochondria[5,50]. Morphological changes reflecting atrophy of the degenerating axons may also be observed[21,51].

1.1.5. Molecular Mechanisms Contributing to Motor Neuron Degeneration

Inter- and intracellular molecular interactions govern the micro and macro processes that enable species survival. In MND, hereditary genetic mutations found in familial ALS (fALS) are the better understood molecular contributors although they only account for ~5-10% of all MND cases. However, MND is not a purely genetic disease and current understanding of its molecular pathophysiology is explored below.

1.1.5.1. Genetic Factors

Over the years, multiple hereditary genes had been identified to be associated with the pathophysiology of MND[52,53]. A recent review by Ferraiuolo *et al*[46] highlighted eighteen, primarily autosomal dominant, genes linked with fALS that were classified into 8 different subsets according to their principle molecular functions.

The most well-known toxic gene mutation in MND is found in the copper-zinc (Cu-Zn) superoxide dismutase (*SOD1*), located on 21q22, that is associated with oxidative stress. Lesser known genetic contributors of fALS include genes for proteins associated with glutamate excitotoxicity (D-amino acid oxidase, encoded by *DAO*[54], and localised on 12q24), endosomal trafficking and cell signalling (Vesicle-associated membrane protein associated protein B, *VAPB*[55,56], on 20q13.3; Optineurin, *OPTN*[57,58], on 10p13; and Alsin, *ALS2*[59], on 2q33), RNA processing (Fused in sarcoma, *FUS*[60,61], on 16p11.2; and TAR DNA-binding protein, *TARDBP*[62,63], on 1p36.2), ubiquitin/protein degradation (Ubiquilin 2, *UBQLN2*[64], on Xp11) and cytoskeletal regulations (Microtubule-associated protein tau, *MAPT*[21], on 17q21).

A recent discovery in MND is the hexanucleotide (GGGGCC) expansion in the first intronic region of the *C9ORF72* (chromosome 9 open reading frame 72). Normal individuals can have up to 30 repeats, but in ALS cases there are more than 30 and

often several thousand repeats[65-67]. The presence of these repeat units accounts for approximately 10% of all ALS cases (40-50% of fALS and approximately 7% of apparently sporadic disease)[65]. However, the precise pathogenesis has yet to be determined.

1.1.5.2. Glutamatergic Excitotoxicity

A notable epidemic of ALS/Parkinson disease complex (ALS/PDC) found within the Chamorro tribe in Guam provided an early indicator to a potential aetiology of MND[68]. By secondary ingestion of β-methylaminoalanine (BMAA, of cyanobacterial origin found in cycads) from Guam fruit bats (*Pteropus tokudae* and *P. Mariannus* and a source of protein for the Chamorro tribe) an over-stimulation of the AMPA receptors, normally activated by pre-synaptic glutamate release, was proposed as a pathogenic mechanism[6].

Glutamate is a common amino acid that is frequently used as an excitatory neurotransmitter in the CNS. Post-synaptic signal transduction following glutamate activation is principally regulated by AMPA and NMDA receptors. In motor neurons, AMPA receptors are the predominant regulator of signal transduction. This is due primarily to the low expression levels of the GluR2 subunit of AMPA receptors in motor neurons which increase their permeability to Ca^{2+} ions[69]. Calcium ions are responsible for a vast array of downstream processes. However, excessive activation, by glutamate or similar molecules like BMAA, could lead to toxic levels of Ca^{2+} influx which is collectively known as glutamatergic excitotoxicity[7].

Extracellular glutamate levels in the human CNS are regulated by glutamate transporters, or excitatory amino-acid transporters (EAATs) 1-5, via a sodium-coupled active uptake[70]. In rodents EAAT1-3 are known as glutamate aspartate transporter (GLAST), glutamate transporter 1 (GLT1) and excitatory amino acid carrier 1 (EAAC1) respectively[71]. EAATs exhibit distinct localisations such that only one form can exist per neuronal or glial cell type[44]. EAAT3-5 are largely expressed in neurons, whereas EAAT1-2 are more commonly associated with astroglia[72]. EAAT1 is predominantly expressed in developing astroglia while mature astrocytes mostly express EAAT2 (known as GLT-1 in rodents). Selective inhibition and knock-out studies of GLAST, GLT1 and EAAC1 have identified astroglial EAATs to be primary regulators of extracellular glutamate[73]. Using porcine astrocytes it was found that EAATs regulate glutamate levels by active uptake then release across the blood-brain barrier for removal[74]. A body of evidence

has emerged that decreased expression and function of EAAT2 may contribute to the glutamatergic excitotoxicity found in ALS[7].

1.1.5.3. Mitochondrial Dysfunction

Due to their significant size and niche motor neurons require disproportionately higher levels of energy provided by greater amounts of mitochondria (a common organelle of all mammalian cell types). However, this importance also highlights the susceptibility of motor neurons to neurodegeneration if mitochondria were to dysfunction.

In neurons mitochondria are mostly distributed within the soma, at nodes of Ranvier, presynaptic and postsynaptic terminals, active growth cones and axonal/ dendritic branches where there are high metabolic demands. Mitochondria are typically recruited from the soma (anterograde, or forward, transport) by the activation of glutamate receptors and/or elevated Ca^{2+} levels[75] (high levels of which can induce apoptosis). In healthy mitochondria contact with high concentrations of Ca^{2+} stimulates the production of adenosine triphosphate (ATP, which is the principle energy source for cellular functions) as well as functions enabling the reduction of cytosolic Ca^{2+} levels. At the same time, these processes initiate the docking and release of mitochondria from transport molecules[76]. When docked mitochondria become exhausted or dysfunctional, retrograde (backward) transport molecules latch on to its membrane receptors and return the mitochondria back to the soma for degradation.

A typical degradation pathway of dysfunctional mitochondria is thought to be via the autophagy-lysosomal system located within the soma. However, they have also been known to undergo fission to remove damaged compartments which can fuse with travelling lysosomes[77]. In some MND cases these mechanism behave unusually and swollen dysfunctional mitochondria have been observed to fuse with lysosomes forming Lewy-like bodies. The increased stress of the significantly enlarged Lewy-like bodies create expansion fractures on their membranes which releases cytochrome c into the cytosol leading to premature apoptosis[50,78].

1.1.5.4. Oxidative Stress

Following post-synaptic membrane activation, elevated calcium levels stimulate oxidative phosphorylation of adenosine diphosphate (ADP) to form ATP; to supply energy for downstream responses. The synthesis of ATP accounts for up to 98% of total oxygen consumption[79] and carbon dioxide production of all cells. However, the remaining 2% of oxygen consumed in respiration is converted into reactive oxygen species (ROS, such as superoxide, O^{2-}, nitric oxide, NO, and related species e.g. OH•) via the electron transport chain associated with the inner membranes of mitochondria[80].

ROS, including free radicals[81], are a group of oxidising species that have a short half-life. As they are very unstable and highly reactive, elevated levels can potentially lead to indiscriminate attack towards the genome and proteome resulting in irreversible molecular insults to proteins, lipids and nucleic acids that affect cell survival[82,83], known as oxidative stress. More recently ROS have been identified as physiological regulators and downstream signalling species of redox homeostasis, metabolism, immunological defence and tissue regeneration/repair. They are frequently produced as catalytic initiators or as facilitators to the removal of molecular debris during inflammation[80]. However, extensive physical insults or repetitive micro traumas, often experienced by football players[5,84] or any other contact sports, may result in a sustained state of inflammation as their tissues are under constant repair; leading to a higher susceptibility to molecular damage, and tissue pathologies including MND[85]. This can often be detected by specific biochemical markers of oxidative stress which were found to be elevated in some CNS tissue biopsies and/or cerebrospinal fluid (CSF) of MND patients[86,87].

In living organisms ROS levels are regulated by free radical scavenging enzymes which are predominantly members of the superoxide dismutase (SOD) enzyme family, and also involves the glutathione system (glutathione-s-transferase, reductase, oxidase). In humans, the principle SODs are the cytoplasmic Cu-Zn superoxide dismutase (SOD1) and mitochondrial manganese (Mn) superoxide dismutase (SOD2) and extracellular SOD (SOD3). SOD2 predominantly resides within the mitochondrial matrix to help regulate the disproportionately higher levels of ROS from mitochondrial activity[88]. Although mutations in *SOD2* have not been found as a major contributor in fALS[89], Ala-9Val mutations in SOD2 had been found to be a risk factor in female patients with sporadic ALS (sALS)[90].

At high levels of oxidative stress mitochondrial forms of copper chaperones recruit and activate cytosolic SOD1 to support SOD2 functions in the mitochondrial intermembrane space (MIS)[88]. SOD1 is a protein dimer that removes ROS by catalysing the reduction of superoxide (O^{2-}) into hydrogen peroxide (H_2O_2) via its copper-zinc centre[82]. Structural comparisons between the SOD1 protein and its common familial ALS mutants, which accounted for approximately 20% of fALS cases[91], identified conformational changes of the mutant protein dimers which increased the catalytic distance between the Cu-Zn centres[92]. This resulted in decreased binding of catalytic Zn-centres which mediated the gain of non-specific, yet toxic, redox reactions[93]. However, it had also been shown that glycation (addition of reactive glucose species) of SOD1, rather than their mutations, that accelerated aging of motor neurons by inactivating SOD1[94].

An additional artefact of SOD1 mutations is their role in stimulating the upregulation of nitric oxide synthase (NOS)[95] leading to the generation of an excess of nitric oxide[96,97]. Nitric oxide is a highly membrane-permeable but relatively stable non-toxic small molecule with principle roles as a vasorelaxant and a neurotransmitter[98]. Within the central nervous system NO is commonly released by astrocytes during periods of high metabolic demand to boost local nutrient supplies as well as to regulate synaptic signal transmissions. It is a strong competitor with SOD1 for superoxide and its toxicity is derived from its reaction product peroxynitrite (NO_3^-) when it is in excess of the capacity of SOD, either due to SOD1 mutations or dysfunctional NO regulatory pathways[98,99].

Peroxynitrite is a selective oxidative species with a strong affinity for thiol groups. It had been implicated in the deamination of guanosine and cytosine which affect healthy processing of the genome[100] by increasing the rate of mutagenesisis. Its toxicity had also been attributed to its role as an intermediate in lipid peroxidation[101] which affects membrane integrity.

Within the proteome peroxynitrite principally attacks tyrosine residues due to its thiol content; thus forming its nitration product 3-nitrotyrosine. Tyrosine is a major component in structural proteins, such as neurofilaments and actin, with the thiol groups contributing towards their stability. As a result, the presence of 3-nitrotyrosine affects monomer-packing which results in fragile cytoskeletal architecture[99]. As 3-nitrotyrosine is highly stable with a lack of native degradation pathway, it is commonly used as a biomarker of oxidative stress[98,102].

Glutathione peroxidase is a downstream regulator of ROS. Its primary role is in the degradation of hydrogen peroxide into water via its reaction with the small molecule glutathione. It is also involved in the reduction of lipid hydroperoxides to their respective alcohols. Glutathione peroxidase and its selenoprotein cousins had been implicated as potential regulators of peroxynitrite[103]. However, the inactivation of its selenocysteine catalytic centre on contact with peroxynitrite limits their possible contributions towards the regulation of oxidative stress[104].

In other oxidative stress models, an established G93A-SOD1 mutant motor neuron cell line (a neuroblastoma x spinal cord hybrid, NSC-34) identified a decrease in the levels of the antioxidant response elements (ARE) and nicotinamide adenine dinucleotide phosphate (NADPH)[5,105], which are both regulators of ROS[106]. However, the cause and consequence of such changes have yet to be fully understood.

1.1.5.5. Protein Aggregation/Malformation

Protein aggregation is a common feature in neurodegenerative disorders. In MND, aggregates are often compact or skein-like ubiquitinated inclusions. Ubiquitin is a relatively common small molecule protein indicator for proteosomal degradation[107]. In certain cases, X-linked mutations of Ubiquilin 2 (*UBQLN2*), a ubiquitin-like protein, has been implicated in interfering with the protein degradation pathways leading to aggregation of misfolded proteins[64]. Another observation was the high proportion of TDP-43-associated cytoplasmic aggregates in MND. TDP-43 is usually found predominantly within the nucleus in healthy motor neurons although the cause for its re-distribution in some cases of MND has yet to be determined[22,78].

Pathophysiological studies of mutant SOD1 models of ALS in mice and some human MND post-mortem tissues have exhibited aggregates of the usually cytoplasmic SOD1 within the intermembrane space of mitochondria. Adhesion of the aggregates to mitochondrial membrane were also observed and this phenomenon appeared to increase with age[52,108]. In combination, these abnormalities affect portions of the electron transport chain eventually culminating in dysfunctional mitochondria which are likely to contribute to motor neuron injury.

1.1.5.6. Cytoskeletal Abnormalities

Actin filaments play a critical role throughout neuronal development and survival[22]. The production and dynamic reorganisation of actin facilitates environmental sensing[109] for growth cone motility in neurite elongation[110], synapse formation and function[111], vesicle[112] and mitochondrial[76] trafficking, as well as structural support for the development of the microtubule and neurofilament networks. In addition, a review by Janmey in 1994[113] implicated cytoplasmic Ca^{2+} levels and downstream phosphoinositide signalling, specifically of phosphatidylinositol (3,4,5)-triphosphate (PtdIns(3,4,5)P_3 or PIP_3)[114,115], in actin filamentous gel-sol (solid-liquid) transitions that are necessary for cytoskeletal reorganisation, although both are also known to affect neuron survival. However, actin filaments are also regulators of ROS and apoptosis by directing the recruitment of mitochondria[76] and lysosomes, as was demonstrated in studies of yeast (*Saccharomyces cerevisiae*)[75,76].

During development or regeneration, neurofilaments are the first structural proteins of neurons to form. As neurites grow and elongate, the myelination process of glia facilitates the exclusive phosphorylation of axonal neurofilaments as a means of stabilising axon structure. Mature neurofilaments are predominantly composed of the three main subunits: heavy (NF-H, 200-220kDa in an SDS-PAGE); medium (NF-M, 145-160 kDa) and light (NF-L, 68-70 kDa). Although current studies have yet to confirm the contribution of mutant neurofilaments to MND, deletion mutants of NFH had been found to be a potential contributor[116]. In addition, some pathological studies of MND models have exhibited phosphorylated somal neurofilaments[117] while selective loss of neurofilaments were found in cases of SOD1 mutant models[118] (potentially caused by the presence of 3-nitrotyrosine, see section 1.1.5.4).

Microtubules are major structural proteins in neurons formed by cross-linkages of α- and β-tubulin on actin networks. They are highly dynamic during development to enable remodelling. As neurites mature into axons microtubules are stabilised by the binding of the small molecular weight protein tau (encoded by *MAPT*) which enables cargo transportation between neuronal compartments[21]. Genetic mutations in *MAPT*[119] had been implicated in the loss of tau-mediated stabilisation of microtubules which resulted in the strangulation of axons; potentially contributing to the development of ALS, dementia and Parkinsonism[52].

Supported by the microtubule network, cytoplasmic dynein and microtubule-dependent kinesin aid retrograde and anterograde transport, respectively. In mutant SOD1 ALS models decreased expression of *KIF3B* (a kinesin-like protein)[91] had been observed which appeared to disrupt axonal transport. However, the disruptions were found to be cargo-specific as only anterograde mitochondrial transport appeared to be affected[76,120]. Interestingly, additional mutations in the dynein motor protein alleviated the interruptions resulting in extended motor neuron survival[121].

1.1.5.7. Abnormal RNA Processing

Disruptions to RNA processing are common features in MND. The earliest known forms of such are genetic defects to the survival motor neuron 1 gene (*SMN1*), or its loss, that contributed towards the pathogenesis of spinal muscular atrophy (SMA, an autosomal recessive form of motor neuron degeneration usually of childhood onset). SMN proteins along with partner molecules to form small nuclear ribonucleoproteins (snRNPs) that are involved in pre-mRNA splicing[122]. Although the exact pathophysiological features of *SMN1* mutations or loss of the SMN protein in SMA are not yet fully understood abnormal *SMN1-2* copy numbers, the latter of which is an alternative but less critical gene for SMN, had been implicated in some ALS cases[123].

TDP-43, as previously mentioned, is a predominantly nuclear protein that has a high affinity for UG/TG dinucleotide repeats in RNA, which suggests an involvement in RNA processing[63]; such as transcription, alternative splicing and the maintenance of RNA stability. Genetic defects in *TARDBP* that code for TDP-43 only accounts for 1-4% of all ALS. However, the redistribution of TDP-43 from nuclear localisation to within cytoplasmic aggregates in ~90% of all cases, including sporadic ALS, suggests an important involvement in the pathophysiology of ALS.

FUS, also known as translocated in liposarcoma (TLS), is a nuclear protein associated with post-transcriptional RNA splicing. Genetic mutation of the *FUS* gene accounts for approximately 4% of fALS and < 1% of sALS cases[61]. The most common forms of mutations are located in the C-terminals of FUS, important for its recognition by transportin for nuclear uptake, which resulted in its elevated presence within the cytoplasm and their subsequent recruitment to stress granules in ALS[124].

1.1.5.8. Glial Cell Dysfunction

Recent developments in the study of MND are the identification of neuron-glia interactions that led to selective motor neuron degeneration. Within the CNS, motor neurons primarily interact with astrocytes (the general regulatory glia), oligodendrocytes (supporter of neuronal function and survival) and indirectly with microglia (resident macrophages of the CNS).

Astrocytes are the most predominant glial cell type found within the central nervous system. They act as environmental, metabolic and homeostatic regulators, as well as part of the blood-brain barrier to protect neuronal function[59,125-127]. However, when astrocytes no longer function normally they can become toxic[32,127]. In astrocyte-motor neuron co-culture models, this toxicity was demonstrated by the recovery observed when isolated fALS and sALS post-mortem patient astrocytes[128] or ALS-linked mutant SOD1 astrocytes[29,100] was replaced with healthy astrocytes[129]. However, there is evidence to suggest that astrocytes were themselves resistant to such toxicity[130].

Under normal circumstances, reactive astrogliosis within the brain stimulates neural stem cell (NSC) differentiation for neuroregeneration following injury or re-patterning[131]. However, within the brain stem and spinal cord, where NSCs are sparse, or when astrocytes differentiate atypically[132], proliferation of astrocytes occupies the cavity where degenerating neurons once resided. This results in the formation of glial scars and the loss of localised innervation as can be seen in some MND cases[51].

Oligodendrocytes are glia cells which promote axon development[37] and CNS myelination[133,134]. Like neurons, oligodendrocytes are post-mitotic and their regeneration is via the differentiation of either of two types of progenitors (oligodendrocyte precursor cells in the subventricular zone of the brain or Sox10/Olig1-positive cells in the ventral spinal cord. 'OPC' for simplicity)[35]. During mild CNS axonal injury, like Schwann cells, oligodendrocytes cause demyelination and undergo apoptosis to signal for the differentiation of OPC for regeneration[40]. However, the mechanism or extent of repair has yet to be determined. In addition, there are still uncertainties as to whether dysfunction of oligodendrocytes has any contributing role to the pathogenesis of MND. Given that astrocytes are the primary regulators and supporters of oligodendrocytes against oxidative stress[135] it raises an interesting question on how the resulting diminished capacity of oligodendrocytes could exacerbate MND pathophysiology.

Elevated levels of neuroinflammatory response are often observed in ALS[136]. This can present itself by increased microglia activity that is stimulated by the presence of pro-inflammatory cytokines, ROS, nitric oxide (NO) and other inflammatory mediators. Following activation, these microglia proceed on to a phagocytic state which initiates the immune response[137]. Similarly, during neuroregeneration following injury microglia are activated to mediate the removal of cellular debris[39]. However, in MND the sustained cell stress can potentially maintain a continuous inflammatory state, leading to a vicious cycle of neuronal injury. Although this is still a hypothetical assumption, it may account for the higher levels of inflammatory response observed in MND[137].

1.2. Models of Motor Neuron Disease

Motor Neuron Disease is a group of neurodegenerative disorders with multiple clinical phenotypes, contributing factors and pathophysiological features affecting primarily the motor neurons. These neurons are themselves one of the most difficult subclasses of mammalian cell types to study due to their inability to divide mitotically following specialisation. Primary motor neuron cultures are commonly derived from embryonic rodents and require careful culture conditions and support from neurotrophic factors to promote *in vitro* survival.

Motor neurons are the first class of neurons to appear during embryogenesis; throughout the neural patterning stage as the neural plate begins to fold. They are produced following asymmetrical differentiation of neural stem cells (NSC)[138]. Their differentiation is dependent on neurotrophic factors secreted by target cells, which also provide chemotactic guidance for neurite growth. In addition, neighbouring neurons and glia (which have a regulatory role in homeostasis) play very important roles towards their maturation and survival. This reliance makes them highly sensitive to minute changes in their environment; thus, further increasing the level of difficulty of obtaining and generating long-term viable models to observe the disease progression in MND. Although significant progress has been made in deciphering the underlying molecular mechanisms with current MND models, positive laboratory results have yet to be successfully translated into beneficial clinical outcomes. An overview of these current models is reviewed below.

1.2.1. *In Vitro* Models

Simple models in the study of MND typically use *in vitro* monocultures of motor neurons derived from either healthy animals or biopsies of patients. As the simplest form of model, they provide isolated as well as relatively modest conditions for the study of the physiological and the molecular functions of motor neurons. Although the optimal period of isolating pure cultures of viable motor neurons are during development, their source is limited to the biopsies of the adult spinal cord (where the cell bodies of motor neurons reside). The process of extraction itself is highly dangerous as it creates lesions in the spinal cord, which is effectively removing localised innervation. At the same time, the health of the extracted motor neurons is not guaranteed. Embryonic motor neurons are the most able to cope with *in vitro* culture conditions but the ethics behind the use of human embryos are highly complex. As a result, most models are presently conducted using embryonic rodent motor neurons, as the hosts are sacrificed whilst the procedures were less ethically challenging.

An alternative to the use of primary cells for *in vitro* model use is the motor neuron cell line NSC-34, which is a neuroblastoma x spinal cord hybrid. This murine cell line closely resembles the early stages of motor neuron development and retains many of the features of mature motor neurons. In addition, their ability to multiply in culture allows for the generation of large numbers of motor neurons for experimentation[139]. The use of NSC-34 models had been beneficial in the understanding of motor neuron-like glutamate sensitivity[140], neurotoxicity[141], mitochondrial dysfunction[108] and genetic susceptibility to MND[105]. However, as with all other cell lines, the results obtained, while useful, are limited due to the inherent abnormal phenotype of these cells.

1.2.2. *In Vitro* Co-Culture Models

Co-culture systems are increasingly being employed in research as more is understood about the interdependent intercellular interactions. Motor neurons are some of the largest cells found in nature (potentially more than 1m in length in humans) and as they are also under a constant state of readiness (in preparation for signal transduction), they have high metabolic demands. In order to cope with all the stresses generated as a result of their normal role, surrounding glial cells provide paracrine signalling and homeostatic

regulation to enhance motor neuron survival in addition to providing supportive roles in repair/regeneration.

Glia support motor neurons in a number of different ways. During neurite development and regeneration Schwann cells and oligodendrocytes deposit extracellular matrix proteins (such as laminin, poly-L-lysine etc.) to provide topographical cues for neurite differentiation and growth[41,142]. At the same time, they also secrete neurotrophic factors which support neuronal polarisation[20] and survival[143]. As axons develop (or regenerate), physical contact between the membranes of axons and oligodendrocytes/ Schwann cells drives the process of myelination[144,145] and the generation of nodes of Ranvier[36]; thus enabling axon maturation in preparation for signal transmission. Astrocytes, on the other hand, serve multiple other regulatory functions (reviewed in 1.1.5.8, and below). As techniques in co-culture systems are gaining maturity, the role of astrocytes in motor neuron disease is becoming more evident[32,146].

In the study of MND the rodent astrocyte-motor neuron co-culture model developed by Nagai *et al*[147] is of particular importance. In their study, it was identified that the presence of Cu-Zn superoxide dismutase (SOD1) mutations within motor neurons in itself was insufficient to cause motor neuron degeneration. It was specifically the toxic soluble factors (generated from a Bax-dependent pathway), secreted by astrocytes with SOD1 mutations, which stimulated the degeneration *in vitro* of both primary and stem cell-derived motor neurons.

In another astrocyte-motor neuron co-culture model reported by Jacquier *et al*[59] the dysfunction of Als2/alsin (a transmembrane protein transporter subunit associated with some juvenile forms of ALS, PLS and infantile-onset ascending hereditary spastic paralysis) was investigated. From their research it was discovered that astrocytes did not express alsin and were able to release a >500 Da neuroprotective (but relatively unstable) factor which selectively improved lower motor neuron survival.

In a less disease-specific study Nishida and Okabe[33] developed neuron-astrocyte co-culture models and *ex vivo* rodent brain slice models to investigate dendritic arborisation (formation of branches or spines) and maturation. It was found that the stabilisation of dendritic protrusions of neurons was dependent on the Rac-1 signalling involved in astrocyte motility. In addition, it was found that via the ephrin/ Eph signalling pathway physical contact between astrocytic processes and primitive

dendritic protrusions facilitated maturation of dendritic spines as well as the formation of synapses at dendritic termini.

In a different *in vitro* model Das *et al*[148,149] developed a serum-free co-culture of myocytes and embryonic motor neurons. From this study they were able to demonstrate that early and short-term application of neurotrophic factors was sufficient to drive the maturation of motor neurons, myocytes and functional neuromuscular junctions (NMJ).

However, despite the developments of these alternative *in vitro* models for the study of MND, such co-culture models are still restricted in their ability to replicate native intercellular interactions. One of the principal factors are their lack of structural similarities to natural nerves or the distinctive spatial segregation of cell types found in the nervous system. For such evaluations *ex vivo* or *in vivo* models had been used instead.

1.2.3. *Ex Vivo* Tissue Models

An alternative to *in vitro* co-culture models is the use of *ex vivo* nervous tissues which retain the majority of native features[150]. The most commonly used forms of such MND models are post-mortem tissue samples from either laboratory animals pre-disposed to genetic and/or epidemiological risk factors[151,152] or human MND patient autopsies with consent[44].

Depending on the time since death and the stage of disease progression nervous tissue slices could be evaluated in two ways. The classical method is by spatial immunohistochemical studies after formaldehyde or cryo-preservation treatments as used by Kersatis *et al*[48] in the determination of ubiquitin-positive inclusions of frontotemporal dementia with MND. Samples prepared via this method have a very long shelf-life, but they are limited in their ability to inform on metabolic processes.

A different method is the explantation of live nervous tissue slices which are commonly used in the study of glutamatergic excitotoxicity[153-155], synaptic responses[156], dendritic arborisation[33] and astrocyte toxicity[59,73,152]. Carefully prepared explanted spinal cord slices can survive in culture for months, which made them a common choice as a therapeutic model[150,157].

Unfortunately, as live *ex vivo* models are still derived from post-mortem sources they are often not healthy enough to study the molecular mechanisms of disease progression in MND. In addition, the stress imposed upon extraction may have been sufficient to influence the observed behaviours of the tissues themselves as well as limit any observable pathogenesis following the induction of further neuronal stress factors.

1.2.4. *In Vivo* Models

For the study of more complex behaviours of MND, animal *in vivo* models are primarily used. The intact nervous system as well as the presence of peripheral biological interactions in *in vivo* models allow researchers to study the disease progression, phenotypical expression and the pathophysiology of MND. Likewise, they are used as the final stage models to identify potential adverse events before therapeutic treatments could be put forward towards clinical trials. However, animal models are fundamentally different to humans biologically. Similarly, they are also unable to present generic systemic data as they have limited genetic and metabolic diversity[158]; due to potential inbreeding in sterile artificial habitats. In addition, there have yet to be successful translation of *in vivo* therapeutic treatments for MND towards positive clinical outcomes.

To generate *in vivo* models of MND, experimental animals are genetically modified or pre-exposed to potential risk factors to express similar traits or symptoms. The simplest *in vivo* models are of invertebrates due to their relatively short gestation period and lifespan. Similarly, their relatively better known cell differentiation patterns during embryogenesis permitted the tracking of the lifecycle of target neurons. However, they are only able to provide information on fundamental biomolecular interactions of human MND due to the lower phylogeny of these species. At present, the most common invertebrates used are nematodes (i.e. roundworm, *Caenorhabditis elegans*)[159] and arthropods (i.e. fruit fly, *Drosophila melanogaster*[160]).

Caenorhabditis elegans is frequently used in mechanistic studies as these invertebrates have gene homologs of approximately 42 % of human genetic disorders. In terms of MND they have been used to study *SMN1/2* (gene ortholog, *smn-1*), *SOD1* (*sod-1*), *MAPT* (*ptl-1*)[159] and *TARDBP* (*tdp-1*)[161]. In addition, their translucent bodies have allowed morphological studies of neurons as they undergo neurodegeneration once

selected cells have been transfected to express green fluorescent proteins (GFP) or a related marker protein.

As they share almost 74% of their genome with human, *Drosophila melanogaster* have previously been employed in genetic screening for potential mutations of human neurodegenerative disorders[160]. One such study in Drosophila identified novel *VAPB* mutations[56] which resulted in increased aggregate deposition, changes in endoplasmic reticulum function and pathological up-regulation of protein chaperones, which were found to be similar to some cases of MND.

Going up the evolutionary tree and as 'next step' platforms for MND research following *in vitro* models rodent (e.g. mouse, *Mus musculus*[50]; and rat, *Rattus norvegicus*), fish (e.g. zebrafish, *Danio rerio*[162]) and non-human primate (e.g. cynomolgus monkeys, *Macaca fascicularis*[163]) models have been developed.

Mice are the most predominant animal models used in MND research[164] as they require the smallest of housing facilities and are fairly docile due to an extensive history of laboratory breeding. The experience and knowledge that came with decades of research using mice also allowed for better experimental flexibility as the biological correlations between mice and human systems are well known. The most common strains of mice used in MND research are transgenic Cu-Zn superoxide dismutase mutants with mice exhibiting SOD1-G93A mutations showing the greatest degree of similarity to human ALS-like pathophysiology[50]. Studies conducted using these strains of mice have informed researchers on downstream motor neuron degeneration pathways[165], irregularities in mitochondrial function[5] and axonal transport[120] amongst many others as contributing towards MND. However, despite significant advances, neuroprotective therapies developed in mouse models have yet to be successfully translated into treatment benefits for MND patients in the clinic.

Zebrafish, on the other hand, are less commonly employed in the study of MND as they require a much bigger facility due to the need for water tanks and specialised filtration systems. However, the translucent bodies of zebrafish enable the use of fluorescent proteins in macroscopic studies. Along with the vast quantities of potential offspring as well as their amazing regenerative properties, zebrafish are a popular choice among researchers. In the study of MND SOD1-G93R mutant zebrafish line had been developed and was shown to exhibit developmental NMJ changes as well as late stage

motor neuron loss typical of MND[162]. However, normal metabolic functions of zebrafish occur at 28°C as opposed to 37°C in the mammalian systems, which along with their relatively distant genetic composition make them less suitable as human MND models.

Non-human primates are the closest animal models that have recently been employed to study human MND. Cynomolgus monkeys (*Macaca fascicularis*) with mutant versions of TDP-43, developed as an alternative model of MND, were observed to display pathophysiology synonymous with the human form of the disease. This included α-motor neuron degeneration as well as TDP-43 re-distribution into the cytoplasm[163]. However, the much greater interactive capability of non-human primates demands much greater ethical clearance and there are still no guarantees of clinical transferability of results from research using non-human primates.

1.2.5. Stem Cell-Derived Motor Neuron Disease Models

Although still in its infancy, stem cell-derived disease models are rapidly emerging as alternatives to traditional *in vitro* and *in vivo* MND models[166]. When given the right stimuli, stem cells, with their pluripotency, could be induced to develop into motor neurons[167]. This is a promising method as vast quantities of human motor neurons could be derived from a single source. In addition, as human cells could be used it would significantly improve the transferability of experimental results towards a clinical outcome. At present there are three primary sources of stem cells: i) embryonic; ii) mesenchymal; and iii) somatic cells with induced pluripotency.

Christou *et al*[168], Jordan *et al*[169], Erceg *et al*[170] and Soundararajan *et al*[171] are examples of research groups that focused on the use of embryonic stem cells (ESC) with the last group successfully generating motor neurons characterised to be typical of those from the medial motor column. However, there are many ethical concerns regarding the use of ESC, especially those of human origin. The main discontent regarding their use are their supply as the only legally accepted source in the UK are generous donations of excess embryos from IVF treatments.

Mesenchymal stem cells (MSC) are multipotent cells derived from biopsies of adult patients. Unlike ESC, MSC are restricted by their source location to the range of cells that they could differentiate into. Although adipose-derived MSC have been successfully

differentiated into Schwann cells[172] due to the same lineage, there are still only limited successes in generating motor neurons from bone marrow stem cells[173].

Fibroblasts are one of the most common somatic cells found in the body as their primary function is as regulators of extracellular matrices. By controlled gene expression (or transfections of select transcription factors) they have been shown to convert into functioning motor neurons. At present there are two routes employed with varying success in generating human motor neurons, specifically those derived from ALS patients[17]. The most common and with better conversion rates are via the intermediary induced pluripotent stem cells (or iPSC)[174,175]. The other, with increasing development, is the direct conversion of fibroblasts into motor neurons, thereby skipping the iPSC stage entirely[176]. Although, like MSC, these somatic cells are primarily derived from patient biopsies, the amount of useful cells are much more significant.

1.3. The 3Rs in Biomedical Research

While there have been extensive research towards an understanding of the pathophysiology of MND, limitations of current models, both *in vitro* and *in vivo*, are caused by their restricted transferability towards a clinical setting either due to structural or species relevance. In addition, due to ethical concerns, there are increasingly vociferous calls for the refinement, reduction and replacement (3Rs) of animal models within the research community. There is, therefore, a need for an alternative type of *in vitro* model where the complexity and the three-dimensional structure of human neural tissues could be replicated to improve current understanding of human MND.

Neural regeneration is a field in tissue engineering where biodegradable polymer scaffolds are being tailored to support the repair of damaged nerves following injury[177]. As such, it specialises in the design and production of guidance conduits to mimic the natural structures of nervous tissues. By understanding the developments and current techniques employed in nerve regeneration their application could be further extended into potential designs for more advanced and relevant *in vitro* MND models.

1.3.1. Neural Regeneration Scaffolds for PNS

Early nerve regeneration studies focused on the repair of peripheral nerves following injury as it is the most common form of nerve damage[178]. As such they are responsible for a significant proportion of current understanding in nerve recovery following injury. As long as damage did not extend into the soma within the CNS, repair is initiated by demyelination, then the regeneration of growth cones at the proximal end of the damage for neurite re-growth; as in development. Subsequent activation of Schwann cells facilitates the degradation and removal of distal axons away from the injury site. However, unlike in development, the guidance of PNS regeneration following minor injury (such as natural wear-and-tear) is controlled by a combination of chemotactic (neurotrophic factors secreted by differentiating Schwann cells) and thigmotactic cues (fine tubular structures known as the Bands of Büngner). Ultimately, this results in the reconnection of the nervous network[39]. However, in major nerve injury, such guidance mechanisms are lost resulting in permanent damage.

Traditionally, minor gaps between peripheral nerve fibres are surgically stitched together by either allografting or autografting of low priority nerves for major gaps. Although surgical sutures connecting both ends of the nerve fibres facilitates nerve regeneration, if the gaps were too wide there may be restriction to muscle movements. In allografting, tissue rejection is a constant threat that would require permanent use of immunosuppressant therapy. In autografting, on the other hand, tissue rejection is unlikely but it will lead to donor site morbidity[16].

Early guidance conduits in peripheral nerve regeneration, as an alternative to nerve grafts, are small tubes with internal diameters of up to 5 mm. Due to a lack of internal structure these conduits are limited to the support of nerve regeneration between gaps of up to 25 mm[12].

Next generation guidance conduits incorporate the use of inner microchannels of less than 100 μm diameter to provide additional thigmotactic guidance[13]. The associated increase in surface area allowed for better control of Schwann cell migration and secretion of neurotrophic factors in a uniform direction. However, dimensions of microchannels similar to that of the endoneurium (typically of no greater than 5-6 μm in human) are difficult to construct, as they are dependent on the manufacturing methods and the chemistry of materials used. In addition, the reduction in exposed membrane

surface area (due to the channel walls acting as physical barriers) would limit any potential cell-cell interactions.

A different approach of introducing internal structures to guidance conduits is the use of aligned ultrafine fibres (of either micro or nanometre diameters)[14,15,179]. Rather than spatial controls as in the microchannels, the fibres control neurite growth by restricting the surface area available for environmental sensing. Although the processing parameters for the control and construction of ultrafine fibres are highly complex, the manufacturing costs are significantly lower. In addition, the increased exposure of membrane surfaces – as a result of the decreased total contact points or channel wall coverage – would improve intercellular interactions.

In some peripheral nerve regeneration models the introduction of Schwann cells into bioactive conduits[180] of fibre scaffolds has been seen to improve axonal regeneration. Significant improvements have also been observed in the guidance of axon growth of explanted rat dorsal root ganglia by aligned fibre scaffolds[14,181]; although there have yet to be studies investigating their effects on motor neuron regeneration.

1.3.2. Scaffolds of CNS Regeneration

Neural regeneration in the CNS is much more complex and is only just beginning to be understood[182]. As the neural network within the brain and spinal cord are highly intricate, regeneration following damage are typically very slow.

Following injury, reactive astrocytosis (or astrogliosis) signals for microglia activation to support the degradation and removal of localised extracellular matrix (ECM), disconnected neuronal components and damaged glial cells. However, due to the different regeneration rates of glia and neurons, astrocytes quickly proliferate and occupy the empty regions thus forming glial scars. This results in localised sclerosis (scarring and thickening) in the region of injury which creates a hostile environment for regeneration of nerve processes. To restrict such growth as well as to re-introduce pre-damage structures sponge-like materials[8] and hydrogels[9] have been assessed *in vitro* that have shown promise.

There are a number of techniques to introduce microporosity within a biomaterial

scaffold. The most technologically straightforward techniques involve Solvent Casting & Particulate Leaching (SCPL), Gas Foaming and Freeze-drying to produce sponge-like materials. Additionally, a versatile and accessible technique to produce a micro- or nano-porous fibre mat is electrospinning. One of the major benefits of these scaffolds is the ease with which they could be batch processed and kept in storage before use. However, for them to function as both a barrier to astrocytosis and support for neural regeneration, there must be a control of pore size which can vary significantly between batches.

Additionally, hydrogels can be used as scaffolds to embed neural stem cells[9] or Schwann cells[183] to enable regeneration. The cross-linking density of the hydrogel is an important factor in the control of cell growth as heavily cross-linked hydrogels generally retards neurite growth. However, unlike sponges hydrogels are physically and mechanically more similar to the extracellular matrix found within the CNS.

Unfortunately, it must be noted that despite significant advances, such technologies are still in development and it is likely to take several years before they could be translated into clinical studies.

1.4. Scaffold Fabrication

A major component in the development of a three-dimensional *in vitro* model is the fabrication of the scaffolds. Aligned micro or nanofibre scaffolds are good constructs in the control of neurite growth[14,15] to support nerve regeneration. The restrictions imposed by the small surface area of the ultrafine fibres limit environmental sensing during neurite elongation thus maximising guidance. For the same reasons, the reduced membrane surface coverage allows for greater cell-cell interactions, specifically those between glia and motor neurons. This makes them suitable structures for the development of three dimensional *in vitro* human MND models (simplified to 'MND models' from henceforth).

1.4.1. Material Selection

Biocompatibility and biodegradability are two principle properties that warrant significant

thought in the development of biological scaffolds. The biocompatibility of a material is its ability to co-exist within a biological system[184]. Although there are still ambiguities in its definition, the most important properties of any biocompatible material are their lack of immunogenicity, toxicity, as well as tolerance of biological stresses. For a material to be well suited for the development of an MND model it must ideally have a similar mechanical property as nerve tissue. In addition, the surface chemistry[185] of the material must also be well adapted to allow for cellular environmental sensing[109] which affects cell adhesion, differentiation and axonal guidance of the motor neurons.

Biodegradability, on the other hand, is a material's ability to degrade under physiological conditions into non-toxic or readily resorbable by-products. Although not essential for the development of MND models, the incorporation of this property into the design process can broaden the applications of the final model. This can include potential therapeutic CNS / PNS tissue replacement or in the traditional application as scaffolds for nerve tissue regeneration following injury.

With known biocompatibility, biopolymers are the most common of all the materials currently used in the generation of aligned fibre scaffolds for nerve regeneration. Complex biopolymers such as collagen[181,186] and cellulose[187] are commonly found *in vivo* as they typically form the extracellular matrices (ECM) of many mammalian organs. Along with silk fibroin[188], of *Bombyx mori* (silkworms), and chitosan[189], of crustaceans, they form the main bulk of materials used in this group. However, they are expensive to obtain as well as difficult to electrospin[190] due to their complex molecular structures and their relative insolubility in solvents of reasonable volatility (explained further below). In addition, these biopolymers have immunogenic potential if they are not thoroughly cleaned before culture with cells, as they are often xenogeneic in origin.

Simple organic polymers are gaining increasing popularity in nerve regeneration research due to their much cheaper relative costs, non-biological origin and the fact that they are relatively easy to electrospin[191] (explored below). Two of the most commonly used simple organic polymers are poly-L-lactic acid (PLLA)[15,192] and polycaprolactone (PCL)[179,181], primarily because of their known biocompatibility and biodegradability.

Of the two polymers, PLLA is the earlier polymer to be employed in the development of aligned ultrafine fibre scaffolds for nerve regeneration. The free acid groups on the polymer chains allow for better hydrophilicity (adsorption of water), which in turn improves cell adhesion. A previous study using electrospun aligned PLLA

micro and nanofibre scaffolds as nerve guides found that, apart from neurite guidance, it also improved the differentiation of neural stem cells (or NSC). In addition, evidence also suggested a preference of NSCs for nanofibre scaffolds, with better differentiation rates, as well as more pronounced maximum neurite length[15]. However, the mechanical properties of PLLA (tensile modulus = 3-4 GPa[193]) are not well matched to simulate ECM of *in vivo* nerve tissues (tensile modulus ~ 0.1 MPa[194]), which limited their use for nerve regeneration.

PCL (a long chain polyester separated by $-(CH_2)_5-$) is another very popular simple organic polymer which is closer mechanically (tensile modulus = 7-22 MPa[195]) to the ECM of *in vivo* nerves. In addition, the relatively inaccessible ester groups on PCL lead to slower biodegradation rates, as well as improving scaffold flexibility[196]. A previous study using aligned PCL microfibers demonstrated controlled regeneration of dorsal root ganglion neurons, with parallel-aligned neurites adhering to and extending along the fibre surfaces for over 2mm per ganglion body. Co-localised Schwann cells were also observed to form intimate intercellular contact along the length of the neurite processes[14], thus making aligned PCL microfibers an attractive material in the development of experimental *in vitro* MND models.

1.4.2. Scaffold Production - Electrospinning

Electrospinning is a relatively cheap and versatile method for the production of micro and nanofibre scaffolds. By careful preparation of materials and optimisation of processing parameters, fibrous scaffolds of selected fibre diameter and morphology could be obtained. This section provides a summary of theoretical principles that are needed to be taken into consideration when embarking on the selective production of aligned fibre scaffolds towards a submicron level using electrospinning.

In electrospinning there are three principal types of apparatus classified according to the type of jets produced: 1) upward jets; 2) downward jets and 3) horizontal jets. At present, a significant proportion of studies report on the use of the downward jet systems, whereby fluid flow is accompanied by the force of gravity. However, with this set-up, if the electrostatic instabilities are not well balanced with the viscoelastic ones, the resulting scaffolds are prone to droplet contamination. Upward jet systems, on the

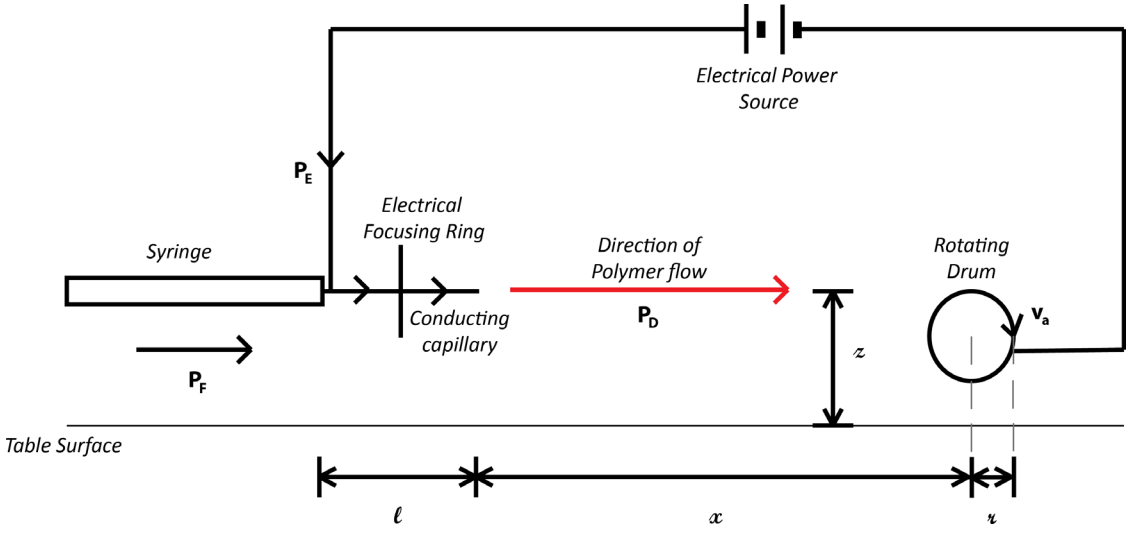

Fig 1.2: Diagramatic representation of a horizontal electrospinnig rig used to produce aligned microfibers. P_E = Electrical Power input; P_F = Power input from fluid motion; P_D = Power used to overcome air resistance or drag; z = height of polymer dispensing from table surface; v_a = angular velocity; ℓ = length of needle; x = distance from needle tip to rotating drum; and r = radius of rotating drum

other hand, are less prone to such issues, but they require more energy to generate as well as to drive the jets towards the collector against gravity. With horizontal jet systems (diagrammatically represented in fig 1.2) gravity only has a partial influence which limits droplet contamination on the product fabrics whilst at the same time reduces the energy required to drive the electrostatic jets.

Neurite alignment is one of the target features in the development of MND models. In electrospinning the alignment of the fibres is primarily controlled by having the electrostatic instabilities overpowering the viscoelastic ones[197]. One method is to employ the use of a rapidly rotating collector with angular velocity (v_a) at or exceeding jet velocity, in place of static plates. This improves fibre alignments by limiting the available orientations of the deposited fibres. Another is the addition of a charged focusing (metal) ring located midway along the dispensing needle to enhance the induced perpendicular magnetic field. This would further align electrospun ultrafine fibres, as demonstrated in fig 1.3 and further explored below.

1.4.3. Principles of Electrospinning

At the start of electrospinning a polymer solution is supplied into a conducting capillary (i.e. syringe needle) where it is subjected to an electric field, determined by a

combination of applied voltage (V)[198], flow rate (Q)[199], capillary surface area to volume ratio[200]. Depending on the overall electrical permittivity (the dielectric property) and conductivity of the different components of the polymer solution, charge is accumulated unevenly, causing electrostatic instabilities. This unstable accumulation of charge reaches equilibrium by distributing themselves across the only exposed surface located at the needle tip where remodelling of the polymer solution (or fluid) is possible. At regions of high surface charge densities the surface stretches and shifts into conical structures known as Taylor cones, where the surface charges are more evenly distributed. When this build-up of charge exceeds the surface tension keeping the solution as a single unit, droplets or beads are generated[201]. However, if the viscosity of the polymer solution (fluid) is sufficiently high the correspondingly higher surface tension would preferentially stretch the beads to form electrostatic jets which would eventually solidify into the electrospun polymer fibres. However, if the polymer solution is subjected to a sufficiently high electric field, those that surpass its Rayleigh limit (the total amount of charge that a material can hold), the solution surface bursts thus forming an electrospray.

The Rayleigh limit of a polymer solution is governed by its dielectric constant that can be controlled via the use of carefully selected solvents that takes into account both their overall polarity and volatility. Polar and/or ionic solvents (or polymers) are generally better at capturing charge[202], which helps to increase the Rayleigh limit allowing for more stable formation of electrostatic jets. However, their comparatively slower solvent evaporation rate means that thicker fibres are generated, as it tends to

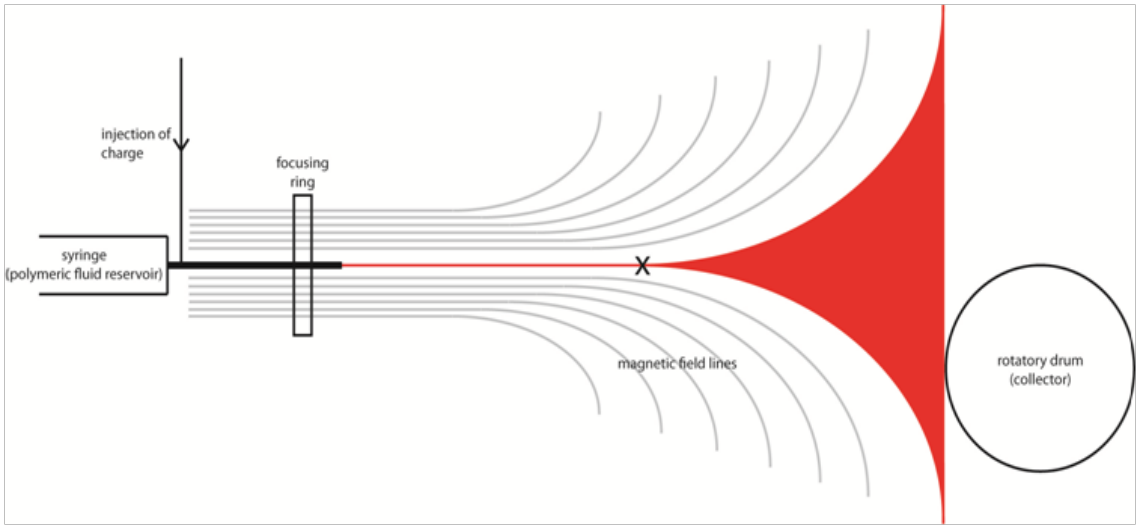

Fig 1.3: The effects of electric field, as represented by the magnetic field, on the path of the electrostatic polymer jets. With the addition of the focusing ring, it further extends the critical straight jet length, marked by X, At this point the viscoelastic instabilities overcome the electrostatic instabilities leading to a 'whipping' effect where the jet can travel in any direction within the highlighted red region.

decrease the polymer relaxation time (considered below). On the other hand, lower to non-polar solvents are less conductive, but the decrease in the Rayleigh limit as a result allows for the formation of smaller Taylor cones leading to the production of much finer electrostatic jets. This also means they are more likely to result in an electrospray. In effect, depending on the diameter of fibres that is desired, the best solvent system is the one that balances the formation of the Taylor cone with the stability of the electrostatic jet.

The propulsion of the electrostatic jet towards the collector is via the action of the electric field induced along the x-axes as well as the perpendicular electromagnetic field along the yz-plane. The gradient of the electric field drives the acceleration and stretching of the electrostatic jet towards the collector. In contrast, the electromagnetic field governs the critical straight jet length[203], which affects the relative alignments of the electrospun polymer fibres. These two parameters are collectively influenced by the potential difference (equivalent to V) between the charged capillary and the grounded collector as well as the distance of the gap between them (x)[204]. Although the electric field along the distance x decreases, it is the steepness of the gradient that affects the point, denoted X in fig 1.3, where viscoelastic instabilities dominate, leading to the whipping effect[205]. By controlling the position of point X along the x-axis, either by manipulating the electric or electromagnetic field, alignment of the electrospun fibres can be achieved.

1.4.4. Effects of Viscoelastic Instabilities

The electrospinning of a material is in effect the stretching of the fluidic state so that on collection they can be deposited as ultrafine fibres. The stretching and re-modelling of the electrostatic jet are governed by the viscoelastic instabilities. These are principally derived from the dynamic inter- and intramolecular interactions between the component molecules of the fluid; denoted as the molecular relaxation time (λ), elasticity (G) and viscosity (μ).

The molecular relaxation time describes the time it can take for a single molecule to collapse into its most stable form. With polymers, it is a good indicator of the degree of entanglement of the polymer strands which can influence on their elasticity and

viscosity. Typically, the more tangled the polymer chains are the longer their relaxation times. With greater molecular relaxation time, decreases in the elasticity and viscosity of the polymer are commonly observed. However, such correlations are only general in principal as a poor equilibrium of these properties can lead to a phenomenon known as "beads-on-a-string"[206], which affects fibre consistencies.

The viscosity, also described as the fluid thickness, is a property that only exists when a material is in a liquid-fluid state as it describes material flow. It also describes how easily a material could be remodelled to minimise external stresses. In electrospinning, the fluidic state of the electrospun polymer could either be obtained as melts[207] or as a solution. As melts the polymers are in a relatively pure form which exhibits strong Van der Waals forces by the accumulation of many areas of weak intermolecular bonding of similar or identical molecules. Such interactions could be further enhanced by increasing the length of the polymer chains as it encourages the formation of additional molecular bonds by chain entanglement. Collectively, these properties contribute towards an increase in viscosity which make them much harder to electrospin; resulting in thicker fibres[200].

The viscosity of a polymer solution is determined by the concentration of the polymer and the composition of the solvent systems[208-210]. High concentrations of polymers increase both the molecular relaxation time and the viscosity. This increase can be alleviated by carefully designing solvent systems to limit the molecular interactions by increased solvation to decrease viscosity. However, the influence of the solvent system on the overall electrostatic instabilities (mentioned previously) must also be taken into account.

The elasticity of a material describes how readily it can return to their original shape when the external stresses are removed. It often correlates with the surface tension and is the principle cause of the whipping effect observed when the electrostatic instabilities are no longer dominant, i.e. at point X in fig 1.3. This can often be manipulated by adjustment of the molecular weight, M_r or chain length, of a polymer, which affects the degree of chain entanglement. However, if the polymer chains are not sufficiently relaxed such that they have a high molecular relaxation time, this could determine the difference between the generation of electrostatic jets or an electrospray.

1.4.5. Environmental Influence on Electrospinning

Electrospinning is the combination of a dynamic equilibrium between electrostatic and viscoelastic instabilities. It is described that the electrostatic instability governs jet formation, acceleration, as well as relative alignments, while the viscoelastic instability controls jet morphology. However, the deposition of the scaffold fibres is governed by environmental parameters that affect the rate of solidification and subsequent time-dependent changes.

The rate of solidification is affected primarily by standard environmental parameters such as the atmospheric air pressure, temperature (T) and relative humidity (ϕ)[211] although via different routes for polymer melts or solutions. However, under laboratory conditions atmospheric air pressure is relatively constant and is mostly ignored.

An increase in relative humidity typically decreases the rate of solidification. In melts, this occurs by the increased surface tension due to a lower air density, which limits molecular air-to-jet interactions. With polymer solutions, the increased relative humidity decreases the rate of the solvent evaporation because of the smaller difference between vapour density of the solvents on the surface of the jets and the density of the humid air.

An increase in temperature on the other hand affects polymer melts and solutions differently. At higher temperatures, the rate of solidification decreases for polymer melts. However, it increases the rate of solvent evaporation for polymer solutions which both increases the rate of solidification as well as decreasing the rate of decrease in molecular relaxation time. The significance of the latter lies in the fact that it can result in increased occurrences of the “beads-on-a-string” effect due to increased polymer chain contractions.

Another less well-considered environmental factor is the electrical conductivity (or dielectric properties) of the surrounding air as it affect the conduction of the electrostatic jets, which in effect completes a circuit, as demonstrated in the schematic shown in fig 1.2. A higher electrical air conductivity, which commonly correlates with a higher relative humidity[212], appears to improve the critical straight jet length which can better align the deposited fibres.

1.5. Aims and Objectives

MND is a group of neurodegenerative disorders with complex epidemiology, pathophysiology and aetiology. As a majority of existing experimental MND models are of non-human in origin, positive laboratory results have yet to be translated into success stories in the clinic. Current developments in the use of human stem cells are beginning to generate data useful in unravelling the pathogenesis of MND[17,168,213]. However, such models are limited in their ability to provide complex neural tissue data for MND due to the lack of three-dimensional structures similar to those found *in vivo*. Therefore, the major aim of this project is to:

1. Identify the ability of micro- vs nanofibres in the control of neurite growth.

   Aligned electrospun microfibre[14] and nanofibre[15] scaffolds have been successfully developed in tissue engineering to support the controlled regeneration of *ex vivo* peripheral nerves[214]. However, increasing evidence is pointing towards the use of nanofibres as they had been found to enhance neuron maturation[215,216] as well as enhancing motor neuron development[217]. Preliminary experiments via the use of a motor neuron cell line NSC-34 (neuroblastoma x spinal cord hybrid)[139] will be conducted on both aligned micro- and nanofibres to select for the most suitable fibre diameter for use in the development of an *in vitro* human MND model.

2. Develop primary neuron-glial co-culture models on aligned fibre scaffolds.

   Once the selection of micro- or nanofibres have been made, similar experiments would be conducted on these scaffolds with primary murine motor neuron cultures to determine their effects on cell survival and differentiation. As glial cells[35] have also been implicated as contributors towards the pathophysiology of MND[218], their effects on establishing defined *in vitro* MND tissue models will also be evaluated via the use of primary murine dissociated spinal cord cultures.

3. Develop alternative methods for the control of electrospinning of submicron fibre scaffolds.

   One of the major factors limiting the more general adoption of aligned nanofibres in nerve regeneration is the technical difficulty in obtaining high quality electrospun submicron fibre scaffolds. This is due primarily to the intricate interdependence of processing parameters where minor changes could affect the morphology of the final scaffolds. Using theoretical models of electrospinning as a basis, an attempt is made to simplify/improve the control of processing parameters to obtain submicron fibre scaffolds.

2. Materials and Methods

2.1. Materials

All solutions were made under sterile conditions where possible and stored at 4°C unless otherwise stated.

2.1.1. Polymer Solutions

PCL: Polycaprolactone (M_r = 80,000, Sigma 440744). **DCM**: Dichloromethane stabilised with methanol for HPLC (Fisher D/1859/17). **Chloroform**: 1.489g/mL stabilised for HPLC (Fisher C/4966/17). **Polymer Solutions**: 5% w.t, 8% w.t., 10% w.t. and 20% w.t. PCL was dissolved in 1:0, 1:1, 3:1 ratios of DCM-chloroform to make up 5 ml of polymer solutions. The polymer was allowed to dissolve between 3 hrs to overnight in sealed containers at room temperature. When not in use they were stored under 5°C in total darkness for up to 2 months.

2.1.2. Buffers

PBS: Phosphate Buffered Saline 1x tablet (Fisher BPE9739-1) dissolved in dH_2O as in manufacturer's specification. **HBSS**: Hank's Balanced Salt Solution without Phenol Red (Lonza 10-527F); sterile filtered at 0.22μm. **HBSS+**: 50ml HBSS; 5 μl 55mM β-mercaptoethanol (Invitrogen 21985023); sterile filtered at 0.22μm

2.1.3. Surface Coatings

pORN: 50mg/ml Poly-DL-ornithine hydrobromide (Sigma P-8638) in 0.15M borate buffered saline pH 8.2. **Laminin**: laminin (Invitrogen 23017-015) 125 ng/ml in HBSS. **PLL**: 0.1% w/v poly-L-lysine in water.

2.1.4. Immunopanning

p75: 1:5000 mouse monoclonal anti-p75 NGF receptor antibody (Abcam ab8877/ ab10495) in 10mM Tris, pH 9.5; freshly prepared.

2.1.5. Media Compositions

NSC Medium: 40ml of 4.5 g/l High glucose DMEM + L-glutamine (Invitrogen 41966052); 400µl of 10,000 units penicillin and 10mg/ml streptomycin solution in H_2O (Sigma P4333); and 4ml of foetal calf serum (Invitrogen 16140071). **Serum Reduced NSC Medium**: 20ml of 4.5g/l High glucose DMEM + L-glutamine (Invitrogen 41966052); 1ml of 20x stock solution Ham's F12 (Invitrogen 21700075); 19ml dH_2O; 400µl of penicillin/streptomycin; 400µl of foetal calf serum (Invitrogen 16140071). **Primary Motor Neuron (PMN) Base Medium**: 50ml of Neurobasal Medium (Invitrogen 21103-049) supplemented with 1% Glutamax-1 (GIBCO 35050); 5 µl β-mercaptoethanol 55mM (Invitrogen 21985023); sterile filtered at 0.22µm. **PMN Supplemented Medium**: 50ml of Neurobasal Medium (Invitrogen 21103-049) supplemented with 1% Glutamax-1 (GIBCO 35050); 1 ml Horse Serum (Linaris SHD3250YK); 1 ml B-27 Supplement 50x (Invitrogen 17504); 5 µl β-mercaptoethanol 55mM (Invitrogen 21985023); sterile filtered at 0.22µm.

2.1.6. Dissociation Solutions

TrypA: 10mg/ml Trypsin with Phenol red (Worthington TRL 3, 3707) in HBSS, colour adjusted to salmon by addition of NaOH. **TrypI**: 500mg Trypsin inhibitor with Phenol red (Sigma T6522) in 49ml HBSS and 1ml of 1M HEPES (pH 7.4, 20mM end conc.) **Depolarisation solution**: 30mM KCl and 0.8% NaCl in dH_2O.

2.1.7. Sample Prepartions, Immunolabels and Fluorescent Stains

Formalin: 27 ml 37% formaldehyde (Sigma F1635); 73 ml dH2O. **Triton**: 0.5% Triton X-100 (Sigma T8787) in PBS. **BSA**: Bovine Serum Albumin (Sigma A4503). **DAPI**: 5 mg/

ID	Antibody	Identifies	Source	Distributor	Dist. ID	Conc. Used
P_1	Anti-β III Tubulin	Neuron	Mouse	Promega	G7121	0.5 μg/ml
P_2	Anti-Islet 1	Motor Neuron	Rabbit	Abcam	ab20670	0.5 μg/ml
P_3	Anti-S100β	Glia	Rabbit	Dako	Z0311	4.0 μg/ml
P_4	Anti-ALDH1L1	Astrocyte	Mouse	Abcam	ab56777	0.5 μg/ml
P_5	Anti-MBP	Oligodendrocyte	Rat	Abcam	ab7349	1:1000
P_6	Anti-GFAP	Astrocyte	Rabbit	Abcam	ab7260	0.5 μg/ml

Table 2.1: Primary Antibodies for the identification of the cell types listed. Dist. = distributor; conc. = concentrations

ID	Fluorophor	λ_{abs}	λ_{em}	Conjugate	Source	Distributor	Dist. ID	Conc. Used
S_1	Fluorescein	494 nm	521 nm	Rabbit IgG	Goat	Vector Lab	FI-1000	1.5 μg/ml
S_2	Fluorescein	494 nm	521 nm	Rat IgG	Rat	Vector Lab	FI-4000	1.5 μg/ml
S_3	Texas Red	595 nm	615 nm	Mouse IgG	Horse	Vector Lab	TI-9000	1.5 μg/ml
S_4	Texas Red	595 nm	615 nm	Rat IgG	Goat	Vector Lab	TI-9400	1.5 μg/ml

Table 2.2: Fluorescent Secondary antibodies. λ_{abs} = peak absorption wavelength; λ_{em} = peak emission wavelength; conc. = concentration

ml 4',6-diamidino-2-phenylindole (DNA-conjugated, λ_{abs} = 364nm, λ_{em} = 454nm, Sigma D9542) in PBS. $\mathbf{P_n}$: primary antibodies in 1% BSA in PBS, dilution as in table 2.1,. $\mathbf{S_n}$: secondary antibodies in 1% BSA in PBS diluted as in table 2.2.

2.2. Electrospinning

Electrospinning of micro-/nanofibres was conducted using the rig set as illustrated in fig 2.1. To start, 1 ml syringes (4.776 mm internal diameter) were fully loaded with 5 – 20 wt% polycaprolactone (M_r = 80,000) in chloroform-dichloromethane (0:1, 1:1 and 1:3) solutions then capped with a blunt 24G syringe needle (0.55 x 40mm, outer diameter x length). Excess air was then expunged before the syringes were set onto the dispenser and connected to the circuit from its base. A focusing ring (60 mm inner diameter x 10 mm length) was also connected to the circuit in parallel to and positioned mid-way along the needle. The polymer solutions were dispensed at constant flow rates (0.3, 1 or 2 ml/hr) via a WPI Aladdin-220 syringe pump. The electric field was induced via the Genvolt 73030 power pack at 8-20 kV, 50Hz. Positioned 5, 10, 15 or 20 cm away from the tip of the needle, a conducting drum (d = 65 mm, ℓ = 150 mm, and motorized to 2000 r.p.m. by an IKA Labortechnik RW20.n stirring motor) was covered with aluminium foil and connected to the neutral end of the circuit for the collection of the deposited fibres. A

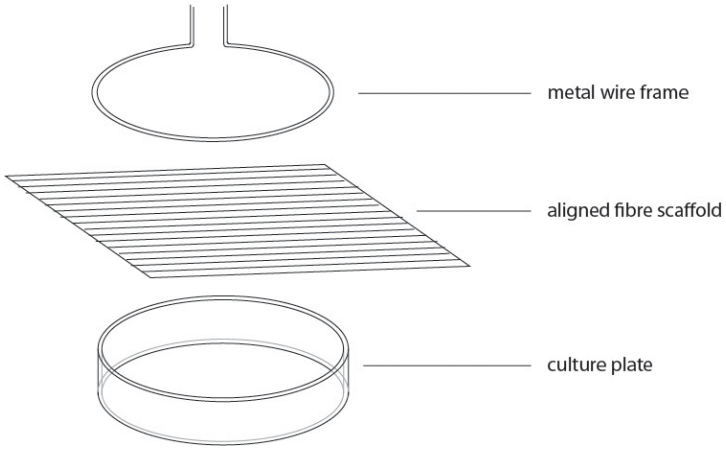

Fig 2.1: Schematic of scaffold set-up

CRD-130-630Y temperature and humidity probe was used to monitor the environmental conditions of the electrospinning region between charged capillary and collector every 15 mins. The effective temperature and relative humidity quoted for each sample were averages of all measurements taken from immediately before and after the start and finish of electrospinning. Collection of the fibres continued until a visible sheet of fabric was observed (~5 min for microfibres and 15 to 60 minutes for nanofibres). The final scaffolds, still on foil, were then stored in a sealed bag at around 4°C until use.

2.3. Scaffold Preparations

Small sections of aligned fibre scaffolds, 35 x 35 mm, were cut then fixed onto the flat underside of 35 mm outer and 25 mm inner diameter 316L stainless steel rings coated with 100 µl of 10% w.t. PCL in DCM. After the sections had dried they were moistened with 70% IMS. With gentle encouragement the scaffolds were peeled off from their metallic supports. They were independently re-stretched and relaxed in 2.5ml 70% IMS in 6-well plates then submerged with 316L stainless steel wire frames, fig 2.1, for a minimum of 30 minutes. To remove residual IMS the scaffolds were kept in sterile PBS overnight under UV light.

2.4. NSC-34 Murine Motor Neuron Cell Line

NSC-34 cells between passages 12-18 were used for all experiments. Stock NSC-34 was passaged at 70-80% confluence, with the conditioned NSC medium (cNM) retained. Whilst the cNM was centrifuged at 400 rpm for 4 mins to remove debris NSC-34 were blasted off the culture dish with 3ml fresh NSC medium with repeated pipette motion. Once all cells were lifted the suspension was diluted with more NSC medium to 28,000 cells/ml then split into aliquots of 1ml onto each scaffold (or well) of a 6-wells plate. Each well was supplemented with 1 ml of the supernatant from the centrifuged cNM before incubation at 37°C and 5% CO_2. The remainder of the undiluted NSC-34 suspension was then re-plated as stock with fresh NSC medium to generate fresh conditioned media. After 24 hours the medium of stock NSC-34 culture was switched to serum-reduced NSC34 media (SRNM) to generate fresh conditioned SRNM (cSRNM) for subsequent media changes. At 48 hrs the media of the 6-wells were switched to 2ml of 1:1 v:v ratio of the SRNM and cSRNM to encourage neurite growth. From henceforth the medium was continually changed three times a week for 14 days before the samples were immunolabelled for confocal imaging.

2.5. Primary *In Vitro* MND Models

2.5.1. Scaffold Preparations for Primary Cultures

After an overnight incubation in PBS, the scaffolds and control wells (all classed as scaffolds from henceforth) were submerged 1.5 ml pORN at 4oC overnight. The solution was then switched to 1 ml laminin and the scaffolds were incubated at 37°C, 5% CO_2 for 2-3 hours. Just before plating the laminin solution was replaced with 1 ml of PMN supplemented media (PSM).

2.5.2. E13 Murine Spinal Cord Dissociates

Pregnant CD-1 mice at E13.5 gestation were sacraficed by cervical dislocation in

accordance with the Animals (Scientific Procedures) Act 1986 relating to Schedule 1 procedures. The embryos were extracted then submerged in HBSS+. The embryos were then decapitated and the tails removed. Incisions were made along the two edges of the spinal column to isolate the spinal cord. After the removal of the meninges, up to two spinal cords were temporarily stored in ice cold 180 µl aliquots of HBSS+. After all spinal cords were isolated, 20 µl of TrypA were incubated with each aliquot for 15 mins at 37°C, 5% CO^2. Trypsination was stopped by the addition of 20 µl of trypI. After gentle mashing the spinal cord tissues were homogenised by repeated pipette motion to a maximum of 15 times. The suspension was then diluted into PSM to 900,000 cells/ml, 1 ml of which were then added to each of the pre-prepared scaffolds and controls. The samples were incubated at 37°C, 5% CO_2 for 6 days, before immunolabelling for confocal microscopy. Half of the medium was replaced by fresh PSM every 2-3 days.

2.5.3. E13 Murine Motor Neurons

In separate 12-well plates each well was coated with 1 ml of the anti-p75 (promotor of neuron differentiation) for 1-2 hours at room temperature. Following the dissociation of E13.5 spinal cords the coating solution in the 12-wells was switched to 1 ml per well PMN base media (PBM) which the homogenised aliquots were then seeded into. For 30-40 minutes at room temperature the motor neurons in the aliquots selectively adhered to the coating. After a single wash with PBM, the remaining motor neurons were detached using 10µl depolarisation solution then resuspended in an additional 990 µl/well PSM. The suspension was then diluted to result in 100,000 cells per 6-well. The samples were incubated at 37°C, 5% CO_2 for 6 days, before immunolabelling for confocal microscopy. Half of the media was replaced with fresh PSM every 2-3 days.

2.6. Immunolabelling

On immunolabelling, culture medium was removed and samples were fixed with formalin for 15 minutes. They were permeabilised with 0.5% Triton X-100 for 5 minutes at 4°C before being blocked with 2.5 wt% BSA in PBS for one hour. They were then incubated

with primary antibodies, table 2.1, for 90 minutes at room temperature. Afterwards, the samples were incubated, also at room temperature, with secondary fluorescent antibodies, table 2.2, for 2 hours. Five minutes before final washes 10 µl of DAPI was added *in situ*. After final washes the samples were left under PBS and were imaged as soon as possible.

Neuron-Glia co-localisations: P_1 and P_3, along with their complementary S_3 and S_1 respectively, were incubated in parallel as above to study the ratio of neurons versus glia.

Motor Neuron Identification: P_1 and P_3, along with their complementary S_3 and S_1 respectively, were incubated in parallel as above to study the ratio of neurons versus glia.

Glial identification: For the identification of either astrocytes or oligodendrocytes, P_4 (with S_3) and P_5 (with S_2) respectively were co-incubated with the samples as above.

2.7. Imaging

2.7.1. Scanning Electron Microscopy

Scanning Electron Microscopy work was conducted at the Sorby Centre, part of the Material Science and Engineering Department of the University of Sheffield. Electrospun fibre scaffolds were evaluated by using either Jeol JSM6400 SEM or CamScan Mk2 SEM. Scaffold samples were mounted onto 15mm aluminium stubs using a graphite-based adhesive whilst still on their aluminium support. They were subsequently gold sputtered at 15 mA under Argon for 1 min. On imaging, electron micrographs were obtained at an accelerating voltage of 12kV and currents of under 30mA. The working distance was set at either 18mm (JEOL) or 35mm (CamScan).

2.7.2. Confocal Microscopy

Confocal imaging was performed at the Kroto Research Institute Confocal Imaging Facility

using the Zeiss LSM510 Meta upright confocal microscope. Images (1332 x 1332 pixels) were obtained using objectives of either W N-Achroplan 10x/0.3, 40x/0.75 or 63x/0.9, with a pixel dwell time of 2.46 μs/pixel. Anti-mouse IgG and anti-rat IgG conjugated with Texas red (λ_{ex} = 595nm, λ_{em} = 615nm) were excited with HeNe 543 nm laser at 0.96 mW with its emission spectrum between 565-615 nm used for imaging. Anti-rabbit IgG and anti-rat IgG conjugated with green fluorescein (λ_{ex} = 494nm, λ_{em} = 521nm) were excited with Ar 488 nm laser at 3% transmission. Its emission spectrum between 500-550 nm was used. The spectral emissions of DAPI between 435-485 nm were imaged after excitation via the multiphoton Ti-Sapphire 760 nm laser at 58.04 mW.

2.8. Image Analyses

All images were analysed in the jpeg format using the analytical tools in Adobe Photoshop CS5. Angular degrees were measured against image normal and corrected for equivalence. They were then normalised using the mean as the point of reference to obtain residual values which were used for statistical analyses. Measurements of lengths for both sets of data were recorded in pixels then scaled up against the image scale bars to obtain metric values.

2.8.1. Measurements of Scaffold Fibres

Fibre scaffolds were magnified up to 5000x to obtain images containing approximately 20 fibres each. For each scaffold five or more frames were taken to obtain a minimum of 100 fibres for comparison as well as to estimate fibre densities. For each fibre the diameter was measured by drawing a line perpendicular to its axis at the middle of the most consistent stretch along their captured length. Alignment values were taken from the angle of this measured line.

2.8.2. Evaluation of NSC34

NSC34 were imaged at 10x magnification for neuron-neurite analyses. Neuronal cell counts were measured as a means of predicting the impact of scaffolds on cell survival and were done by counting the total distinct nuclei per frame. Individual neurites were defined as observable processes with distinct hillocks and visibly connected growth cones (or axonal termini). The distances along the neurite axes between these sets of two points were measured as the neurite length and the total count of such lengths was recorded to calculate a ratio to define the degree of neuronal differentiation on scaffolds. Alignment values were recorded, as before, as the overall degrees away from normal of image of all the lines drawn on top of the defined neurites.

2.8.3. Evaluation of Primary *in vitro* Murine Models

Primary models were evaluated at 40x magnification. However, due to difficulties in obtaining measurable samples analyses were limited to image comparisons of the presence or absence of immunolabelled biomarkers.

2.9. Statistical Analyses

Statistical analyses were conducted using the statistical programming language R. Significance for all data sets were defined as having $p < 0.05$.

Alignment data were first corrected for equivalence before residual values (unit distance away from the mean) were calculated to generate histograms with bars defined by 2-degree intervals. A normal distribution graph was fitted and overlaid onto the histograms to confirm normality. Given the identical means of these data, a Bartlett's test was used to test for the homogeneity of the variances between samples. The greatest degree of alignment is defined by the lowest p values as determined against the control distributions.

Analysis of variance (ANOVA) was conducted for all other data sets with transformation as appropriate for the type of data and distributions observed. For count and ratio data, Poisson transformations were employed to calculate the adjusted p

significance via TukeyHSD() function. Continuous data of neurite lengths and scaffold fibre diameters were assessed visually by plotting the density of the data via the ggplot() function and compared with fitted distributions to identify suitable transformations for ANOVA.

3. Results

Previous studies in nerve regeneration reported the use of 1 μm diameter fibres to be the best at guiding *in vitro* neurite growth following injury of rat dorsal root ganglia[14]. However, 1 μm fibre scaffolds were also at the lower limit within the range of fibre diameters used in that study. In the development of *in vitro* human motor neuron disease (MND) models, a motor neuron-like neuroblastoma hybrid cell line (NSC-34) was used initially to assess the full range of micro- to nanofibre scaffolds. This was to identify the most suitable scaffold/s that would provide the best environment for cell-cell interactions as well as neuronal survival. Once selected, primary murine spinal cord dissociates and pure motor neuron cultures were cultured on such scaffolds for morphological analyses. To minimise the effects of seeding density, only scaffolds with a minimum of 30% fibre occupancy were used.

3.1. Evaluation of aligned PCL fibre scaffolds using NSC-34 cells

Five aligned fibre scaffolds spanning the range of nano- to microfibers were assessed *in vitro* in the control of NSC34 neurite development. The scaffolds used were classified as follows: 300 nm (mean= 307 ±13 (SEM) nm); 700 nm (640 ±39nm); 800 nm (669 ±57nm); 2 μm (2.63 ±145nm) and 4 μm (4150 ±332nm), shown in fig 3.1. On visual inspection, although all scaffolds appeared to support NSC34 survival and neurite growth, cells cultured on 300 nm and 2 μm appeared to be unhealthy as they displayed a condensed morphology.

Assessment of scaffolds' ability to support neurite growth was measured by neurite length after 14 days, fig 3.2A. The distribution of measured neurite lengths exhibited log-normal characteristics; as such, quoted values are the median and the 95% confidence intervals (C.I., or the range of neurite lengths that 95% of neurites measured would fall into) as well as the total neurites assessed. In descending values the recorded values of neurite lengths are as follows: 2μm (118.81μm, 95% C.I. = 16.66-626.67μm, n = 27); 700 nm scaffolds (80.66μm, 95% C.I. = 49.71-129.14μm, n = 324); TCP (78.97μm, 95% C.I. = 41.86-133.75μm, n = 214); 300 nm (71.50μm, 95% C.I. = 24.69-211.61μm, n =

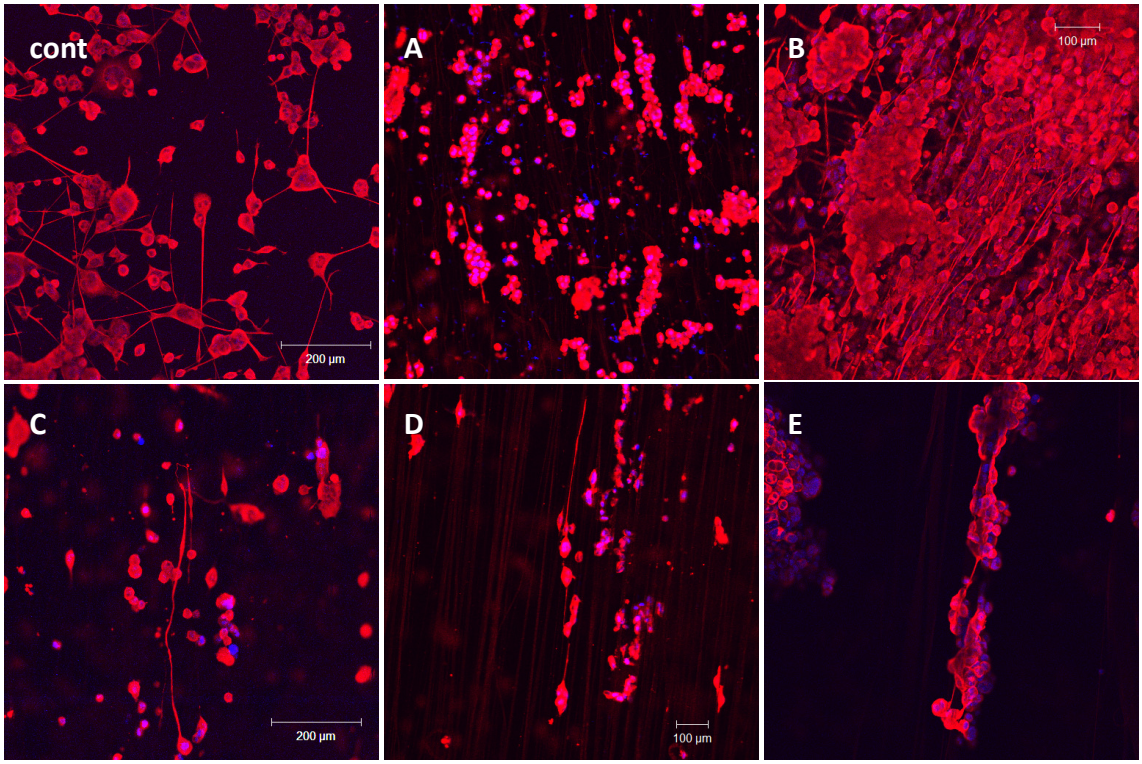

Fig 3.1: 14 days 10x Confocal images of NSC34 on a range of polycaprolactone fibre scaffolds. All samples were stained for β-tubulin III (red) and with DAPI (blue) then imaged. These images highlights the improvements in neurite alignments with the use of the aligned fibre scaffolds as opposed to the use of traditional flat culture surfaces. Scaffold fibre diameters: **cont**: Tissue culture plastics; **A**: 307nm, 95% C.I. = 295-319nm; **B**: 640nm, 95% C.I. = 606-676nm; **C**: 669nm, 95% C.I. = 678-735nm; **D**: 2.63µm, 95% C.I. = 2.40-2.88µm; and **E**: 4.15 µm, 95% C.I. = 3.83-4.50µm; n = 3

61); 800 nm (59.72µm, 95% C.I. = 26.98-151.88µm, n = 89); and 4 µm (45.35µm, 95% C.I. = 20.89-100.59µm, n = 91). Although significance was observed in ANOVA ($p < 0.001$), no specific scaffold stood out as best.

The ability of scaffolds to control neurite growth was evaluated by the quantity known as the relative alignments, fig 3.2B (or fig 3.3 for distribution overlays). The measured values for each scaffold were corrected for equivalence for each image and evaluated in terms of the residual degrees against the mean. In general, the use of the aligned fibre scaffolds significantly improved the alignment of neurite growth (Bartlett test for homogeneity: $p < 0.0001$) with 300 nm appearing to be the best (shown in red in fig 3.2B).

Scaffold presence on NSC34 survival and maturation was assessed by the average cell and neurite count per 1 mm^2 frame, respectively (fig 3.2C and D). In terms of cell counts, NSC34 cells cultured on 700 nm (521 ±334 cells/mm^2) appeared to be thriving. When analysed via ANOVA, significance was observed against 800 nm (104 ±96 cells/mm^2, $p_{adj} < 0.05$), 2 µm (192 ±111 cells/mm^2, $p_{adj} < 0.05$) and 4 µm (187 ±153

cells/mm^2, p_{adj} <0.05). No significance was observed in the mean cell counts between the control (234 ±183 cells/mm^2), 300 nm (413 ±223 cells/mm^2) and 700 nm scaffolds, although significance was observed between 800 nm and 4 µm scaffolds (p_{adj} <0.01). In terms of neurite counts, significance was observed between TCP (43 ±16 neurites/ mm^2) against all cultured on scaffolds: 300 nm (10 ±6 neurites/mm^2, p_{adj}<0.001); 700 nm (23 ±16 neurites/mm^2, p_{adj}<0.05); 800 nm (13 ±7 neurites/mm^2, p_{adj}<0.001); 2 µm (3 ±2 neurites/mm^2, p_{adj} <0.001) and 4 µm (6 ±5 neurites/mm^2, p_{adj} <0.001). Significance was also observed for 2 µm (p_{adj} <0.001) and 4 µm (p_{adj} <0.01) against 700 nm. However, the

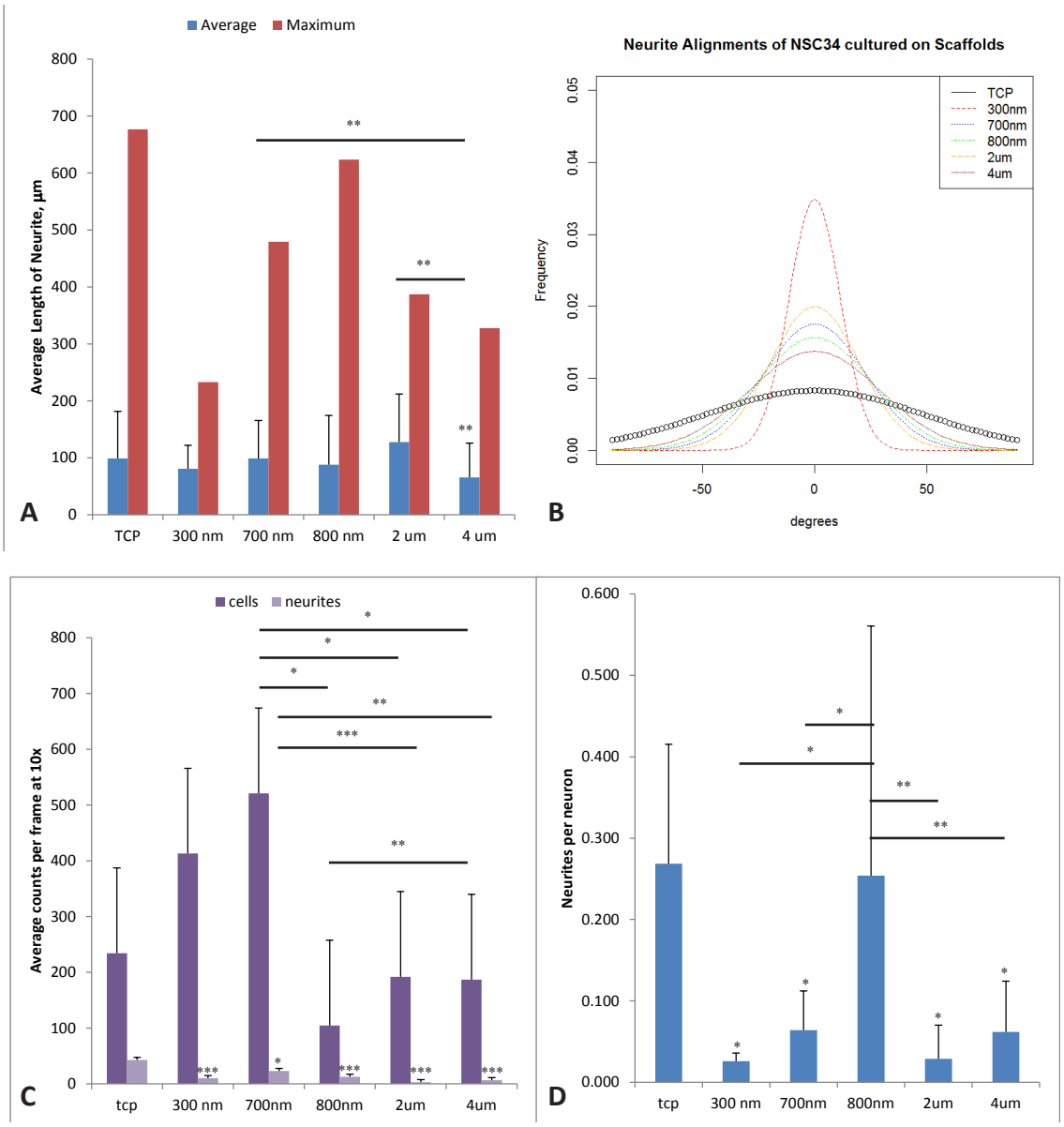

Fig 3.2: Data on the average cell and neurite counts per 1 x 1 mm frames, neuron-neurite ratio and neurite length and alignments were collected for each of the scaffolds. **A**: mean and maximum neurite lengths in µm (ANOVA: p <0.001). **B**: fitted normal distributions of the residues of relative alignment of neurites growth calculated from mean degree deviation from normal of image (Bartlett's: p <0.001). **C**: average cell (ANOVA: p <0.001) and neurite (ANOVA: p <0.001) counts per frame. **D**: neuron-neurite ratios (ANOVA: p <0.001). Significance denoted by * p < 0.05, ** p < 0.01, *** p < 0.001, n = 3

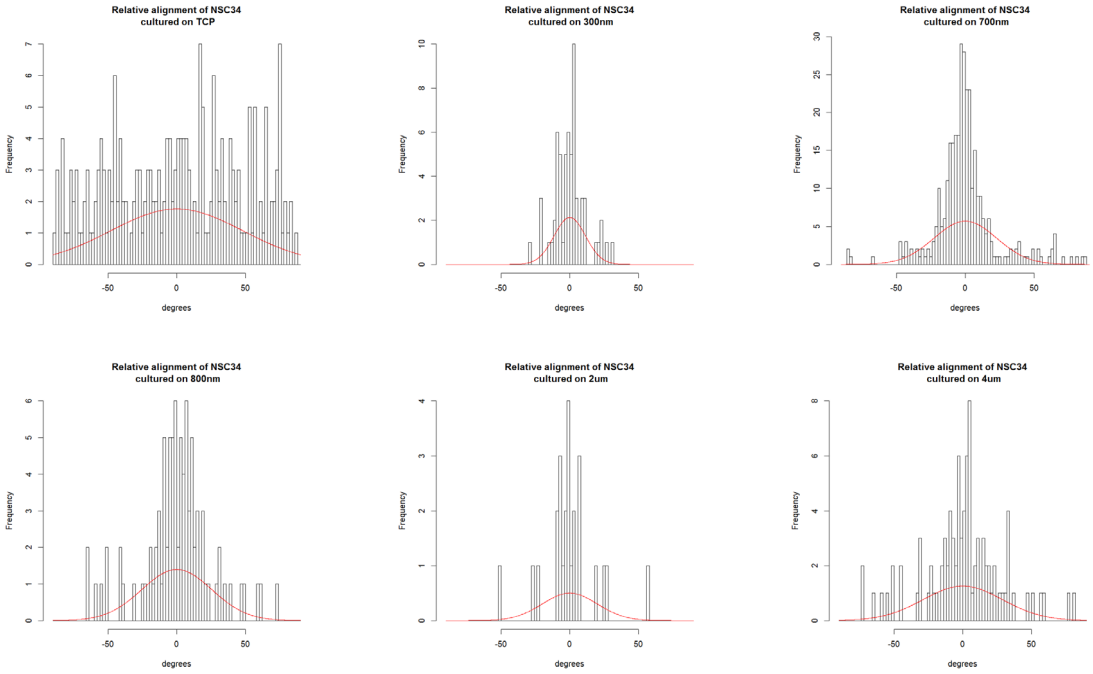

Fig 3.3: Relative Alignments of Preliminary NSC34 Neurites on Selected Scaffolds.
Histograms of residual values of transformed neurite alignment data classified by 2° intervals. Red curve is the fitted normal distribution plot.

N-number (N=3) is low, so caution must be used when drawing conclusions from the statistical analysis.

As neurite count is highly dependent on neuronal cell count neuron-neurite ratios were also evaluated, fig 3.2D. In terms of average values NSC-34 grown on 800 nm (0.254 ±0.307) fibre scaffolds were the closest to those grown on TCP (0.269 ±0.147, p_{adj} = 1.00), which would have suggested it to be optimal. However, on closer evaluation when scaffolds were further classified according to the age of the plated NSC34 the neuron-neurite ratio were statistically identical: P14, 700 nm (0.064 ±0.048) v 4 µm (0.062 ±0.064), p_{adj} = 1.00; P16, TCP v 800 nm, as mentioned earlier; and P22, 300 nm (0.026 ±0.010) v 2 µm (0.029 ±0.064), p_{adj} = 1.00. These results gave rise to uncertainty as to whether the observed differences in cell/neurite counts were due to the scaffold fibre diameters themselves or due to the age of the NSC34 cells.

From this set of experiments, evidence emerged pointing towards the use of submicron fibres, including the most dramatic improvement in neurite alignment and the higher cell density observed. However, the mild significance between micro- and nanofibres as well as the uncertainty generated from the separation of NSC34 cultures by age suggested the need for further evaluation.

3.2. Extended NSC34 Models

Following the uncertainty observed in the preliminary experiments the range of scaffolds used was reduced to submicron fibre diameters and assessed in parallel for each set of comparative experiments. The scaffolds used were fine (mean = 201 ±9 (SEM) nm), medium (405 ±19nm) and thick (mean = 598 ±38nm) as well as tissue culture plastics as control. In addition, passages 13, 14, 16 and 17 of NSC34 cells were evaluated.

In general the effects of submicron fibre scaffolds on the survival and differentiation of NSC34 cells appeared to be limited to restricting the total cell count to approximately one third of those cultured on control (fig 3.4A; TCP: 614 ±158/mm^2; fine: 152 ±81/mm^2; medium: 141 ±98/mm^2; thick: 119 ±84/mm^2). No significance was observed between scaffolds. When passage number was taken into account a general decline in cell and neurite counts against passage number for all scaffolds (fig. 3.5) was

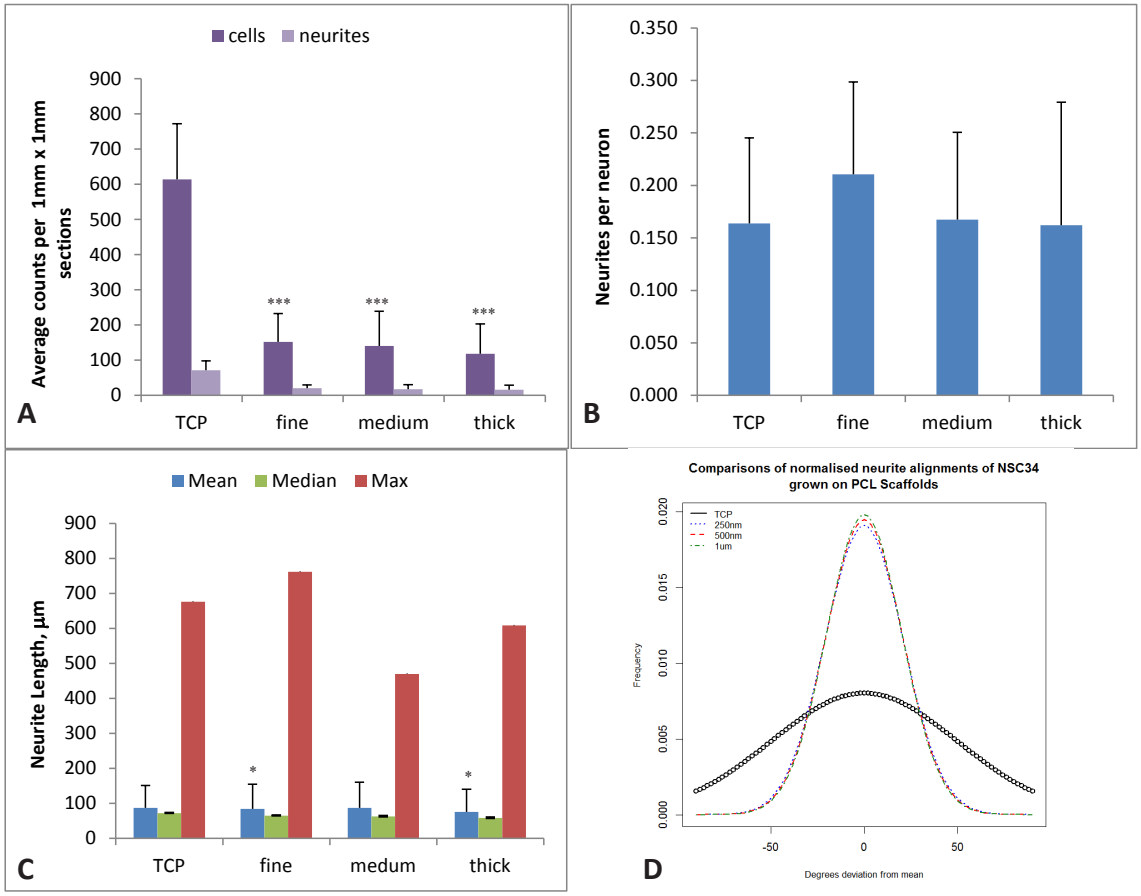

Fig 3.4: Data on the average cell and neurite counts per 1 x 1 mm frames, neuron-neurite ratio and neurite length and alignments were collected for each of the scaffolds. **A**: average cell (ANOVA: p <0.001) and neurite (ANOVA: p <0.001) counts per frame. **B**: neuron-neurite ratios (ANOVA: p <0.001). Significance denoted by * p < 0.05, ** p < 0.01, *** p < 0.001, n = 3 **C**: mean and maximum neurite lengths in µm (ANOVA: p <0.001). **D**: fitted normal distributions of the residues of relative alignment of neurites growth calculated from mean degree deviation from normal of image (Bartlett's: p <0.001).

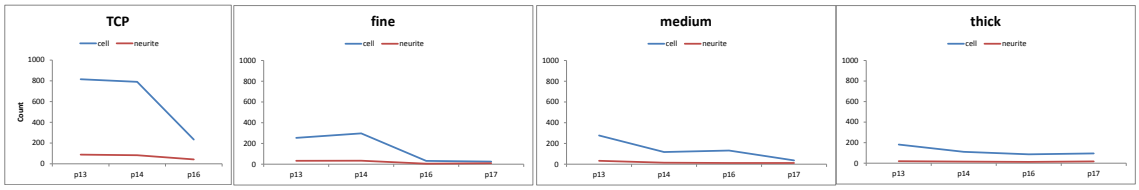

Fig 3.5: Effect of Passage on Cell Survival. Simple line chart demonstrating the effect of passage number on the total cell/ neurite count on chosen scaffolds.

observed, although the differences were not significant.

Neuron-neurite ratios were evaluated as before. A slight increase was observed at higher passages (fig 3.6A and 3.6B) for both the control and fine fibre scaffolds, although a minor decrease was observed for medium scaffolds and almost no change in thick fibre scaffolds (fig 3.6C and 3.6D). However, statistical analyses proved inconclusive.

Visually, mean neurite lengths were found to be almost identical between all scaffolds (TCP: median = 72.36 μm, 95% C.I. = 56.08-88.62 μm, n = 1329; fine: 65.07 μm, 95% C.I. = 49.39-83.78 μm, n = 954; medium: 62.75 μm, 95% C.I. = 49.84-90.54 μm, n = 617; and thick: 58.30 mm, 95% C.I. = 40.95-83.18 μm, n = 506; fig 3.4C, raw distributions shown in fig 3.7). However, one-way and two-way log-normal ANOVA against both scaffolds and passage showed significance ($p<0.001$ for all). When adjusted p values for all samples were compared significance was mostly observed against p14 samples, appendix A.

In the evaluation of relative alignment data, apart from the improvement observed via the use of scaffolds, no significance was observed between the use of any of the submicron fibre scaffolds (fig 3.4D, histograms and fitted distributions shown in fig 3.8).

Overall, the data suggest the use of p14 NSC34 cultures to be ideal, although no statistically significant effects across all types of data were observed to facilitate the selection of any particular submicron fibre scaffolds.

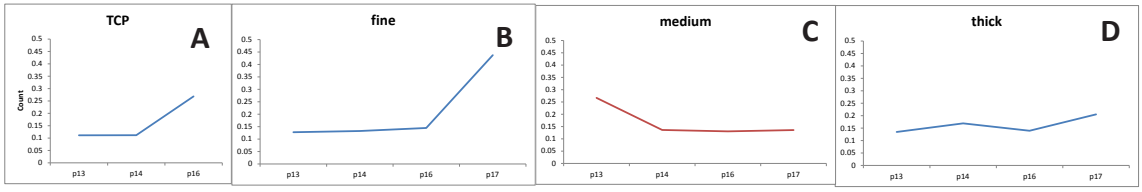

Fig 3.6: Effect of Passage on NSC34 Neuron-Neurite Ratio. Neuron-neurite ratio of extended NSC34 experiments as separated by scaffolds. Labels are as follows: TCP (control); fine (mean = 201 nm, 95% C.I. = 153-265 nm); medium (405 nm, 95% C.I. = 348-472 nm); and thick (598 nm, 95% C.I. = 552-648 nm)

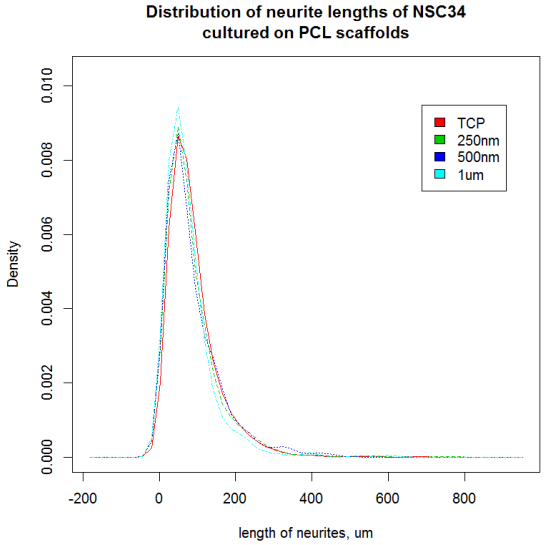

Fig 3.7: Fitted Distribution of Neurite Lengths. Raw distribution of neurite lengths as plotted via the ggplot() in R. Transformation analyses pointed towards a log-normal distribution, $p > 0.5$.

3.3. Primary Murine E13 Spinal Cord Dissociates

Following from the results of the NSC34 studies, the extended models were translated for use with primary dissociated murine spinal cord cultures. Early studies suggested clustering of dissociated spinal cord cells on microfibre scaffolds with improved cell-cell scattering/migration on submicron fibre scaffolds (fig 3.9D v fig 3.9B and 3.9C respectively). However, differentiation and survival of dissociated spinal cord cultures appeared to be hindered when compared with those cultured on tissue culture plastics as control (fig 3.9A).

To improve differentiation and survival of motor neurons in *in vitro* models, poly-L-lysine[219] and laminin[192], both commonly used in neuronal models, were coated on tissue culture plastics and compared against control. Overall, both coatings improved cell adhesion. However, poly-L-lysine appeared to induce necrosis (demonstrated by the fluorescent rings in fig 3.10C) as well as clustering of glia and neuronal somata (fig

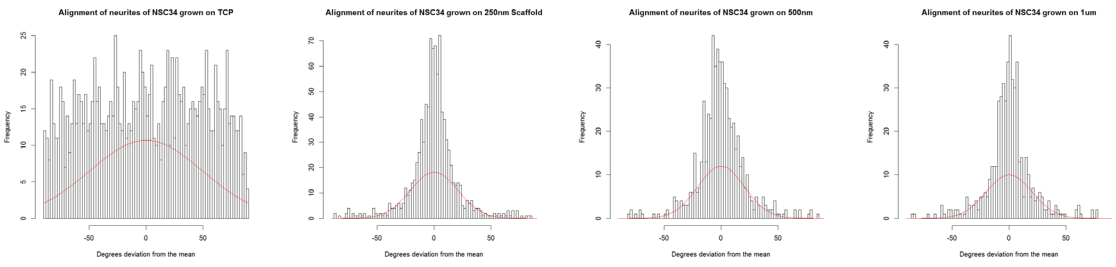

Fig. 3.8: Alignment Distribution of Extended NSC34 Models. Histogram of relative residual values following transformations of relative alignment data of NSC34 neurites culture on submicron fibre scaffolds. All data are classified by 2° separations with fitted histogram shown in red.

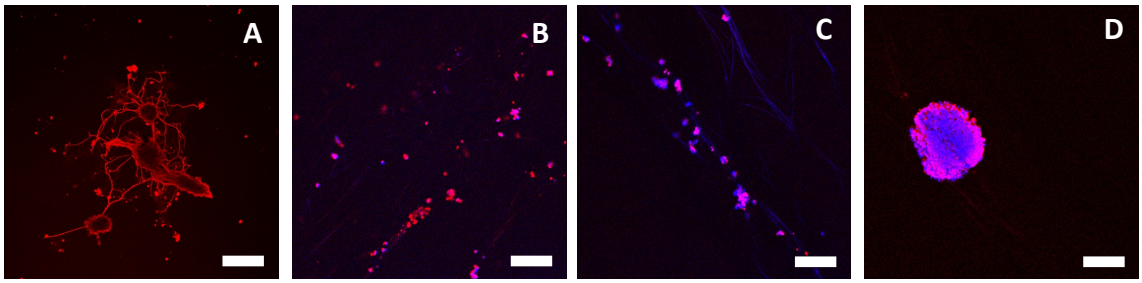

Fig. 3.9: Primary E10 Murine Spinal Cord Dissociates. Preliminary cultures of primary spinal cord dissociates cultured under minimum conditions for 7 days. No coatings or growth factors were used. Scaffolds used were tissue culture plastics (**A**), 346 ± 206 nm (**B**), 735 ± 392nm (**C**) and 4.75 ± 4.51μm (**D**) fibre diameter scaffolds. Scale bars represent 100 μm. From the images it could be observed that the use of fibres allowed controlled migration of neuroblasts although the degree of differentiations were much restricted on the fibres. When the different scaffolds were compared, cells cultured on microfibres tended to form strong clusters as opposed to the more dispersed growth of cells cultured on submicron fibres.

3.10D) for dissociated spinal cord cultures. Laminin, on the other hand, significantly improved pure motor neuron survival and differentiation (fig 3.10B) as well as supporting the dispersion of spinal cord cultures (fig 3.10E) thus allowing greater clarity to study individual cells.

The above experiment was repeated on both uncoated and laminin-coated nanofibre (405 ±19nm) scaffolds. The resulting spinal cord dissociates exhibited strong preference for laminin-coated scaffolds as defined by the much stronger fluorescence intensities observed for both S100β and β-Tubulin III immunolabels, used as glial and neuronal markers respectively (fig 3.11). However, the survival/differentiation of pure motor neuron cultures was not observed. As such all further experiments focused on spinal cord dissociates.

Following from the selection of laminin coating, subsequent experiments concentrated on the selection of ideal submicron fibres, as used previously for NSC34 models. Again, no preference was observed for any of the scaffolds. However, the amount of cell clustering, as observed previously, was markedly reduced when microfibres were used.

An attempt was made at identifying the degree of differentiation for astrocytes, oligodendrocytes and motor neurons which are the target cell types in the development of an *in vitro* human MND model, fig 3.12. Although S100β labelling suggested presence of glial cell types, fluorescence intensities immunolabelled for biomarkers of both astrocytes (ALDH1L1 and GFAP) and oligodendrocytes (MBP) were very weak. So much so, that such signals were completely eliminated when compared against fluorescence intensities of scaffolds cultured with conditioned medium derived from spinal cord dissociate cultures. Having considered the time-lag between the differentiation of motor

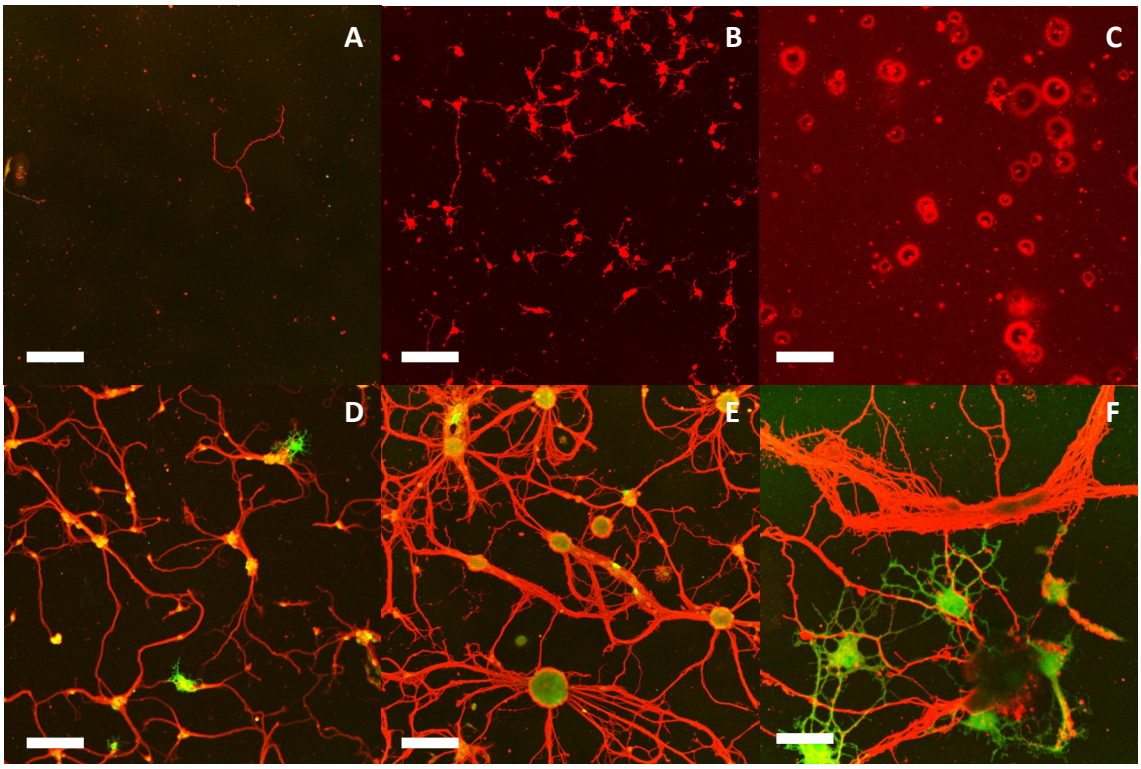

Fig 3.10: Confocal images of primary murine E13 motor neuron cultures (seeding density 50,000 cell/ml) and spinal cord dissociates (450,000 cells/ml) on coated tissue culture plastics (TCP). Red fluorescence is labeled for β-Tubulin III as a generic marker for neurons. Green fluorescence is labeled for S100β as a generic glial markers. Unless otherwise stated all images were at 10x magnification and the scale bars represent 100 μm. Although the use of coatings improved cell adhesion when compared to control (**A**, no coating) it could be observed that the use of laminin was better at supporting motor neuron survival and differentiation (**B**) as the use of poly-L-lysine appeared to stimulate necrosis; demonstrated by the fluorescent 'rings' (**C**). In addition, the use of laminin enabled a more dispersed primary mixed glia-neuron culture (spinal cord dissociate, shown in **D**) as compared to strong glial and neural somata clustering seen in **E** when cultured on poly-L-lysine. Image **F** shows primary E13 spinal cord dissociates cultured on laminin-coated TCP at 40x magnification, scalebar represents 20 μm, for clarity.

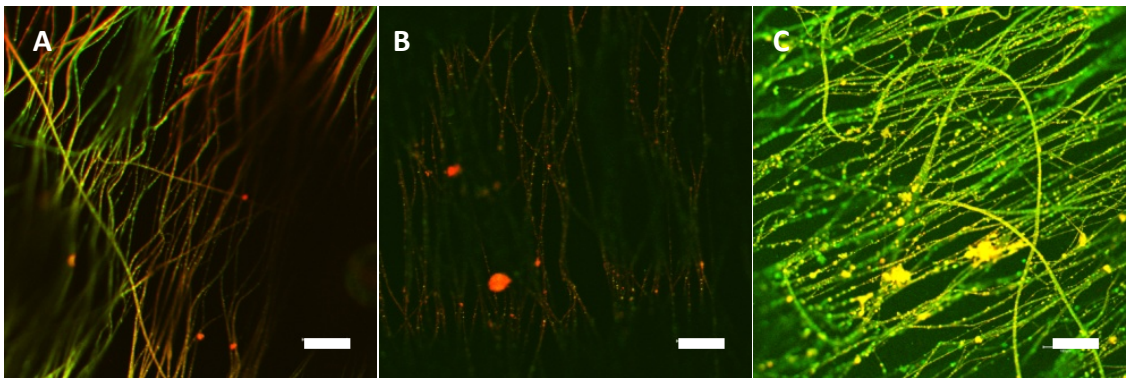

Fig. 3.11: Primary E13 Murine Spinal Cord Dissociates Cultured on Polycaprolactone Nanofibre Scaffolds. Primary E13 Murine spinal cord dissociates were cultured on bare (**A**), poly-L-lysine- (**B**) and laminin-coated (**C**) polycaprolactone nanofibres. Although fluorescence was observed for both labels identifying both β-Tubulin III (red) and S100β (green), used as neural and glial markers respectively, the fluorescence intensities of markers for cells cultured on laminin-coated polycaprolactone fibres were the strongest. Scalebar represents 20 μm.

neurons vs astrocytes and oligodendrocytes, the cultures were extended from 6 days to thirteen days. However, no difference was observed. Identical results were obtained whilst trying to identify motor neurons via the use of Islet-1 immunolabelling.

From this study, it could be concluded that the use of submicron polycaprolactone fibres supported the growth, control and survival of motor neurons as well as glia, although the use of laminin improved the results when compared against poly-L-lysine or bare fibres. The differentiation of glia into astrocytes or oligodendrocytes as well as their ratio in cultures on the scaffolds have yet to be determined as identification markers for both cell types appeared to be identical to control (or blank) samples. However, primary motor neurons have yet to be successfully cultured on submicron fibre scaffolds.

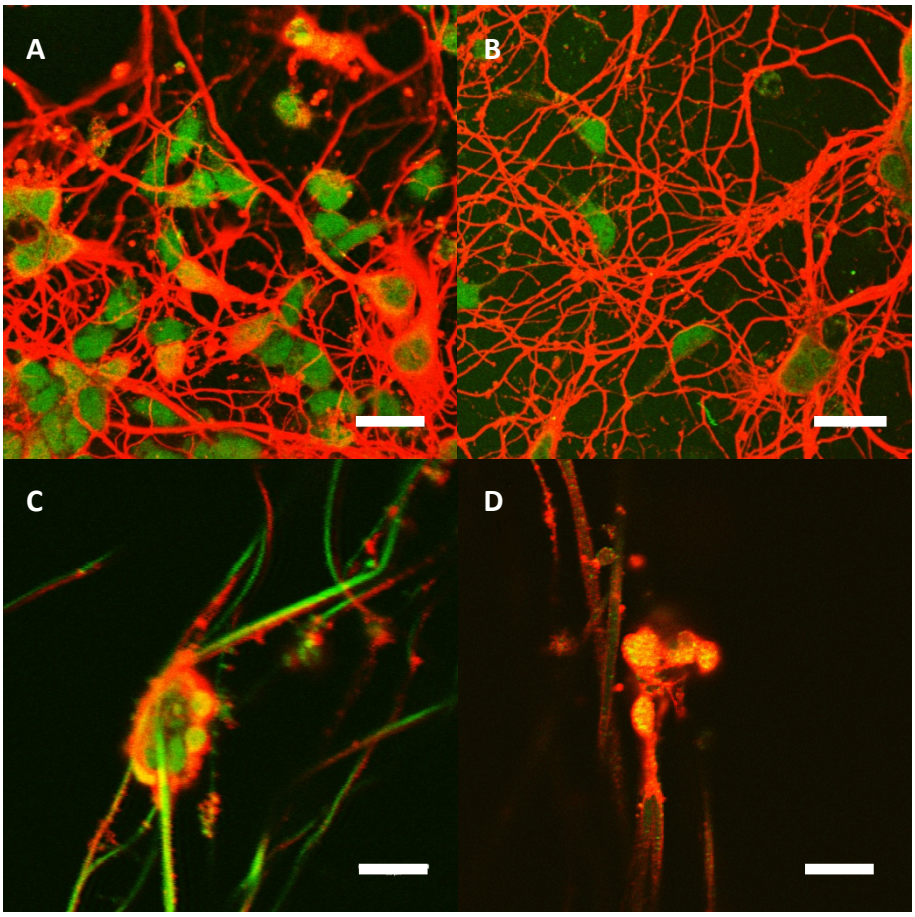

Fig 3.12: Confocal images of primary murine E13 spinal cord dissociates (1,500,000 cells/ml) cultured on laminin-coated tissue culture plastics (**A-B**) and laminin-coated polycaprolactone medium fibre scaffolds (**C-D**, 405 nm, 95% C.I. = 348-472 nm fibre diameters). Spinal cord dissociates were double immunolabelled for β-tubulin III (red) and S100β (green) to identify glia/neuron presence (**A**,**C**) and also for β-tubulin III (red) and Islet-1 (green) for motor-neurons (**B**,**D**).

4. Fabrication of Aligned Submicron Fibre Scaffolds

Given the emerging evidence pointing towards the preference of neurons for submicron fibres, there is an increasing need for the efficient generation of nanofibres with a highly controlled morphology. Electrospinning is a simple yet versatile process in the fabrication of ultrafine fibres of micro- to nanometre dimensions. However, the major limitation to its use for the generation of submicron fibre is the multiple contributions of each processing parameter towards the generation of consistent electrostatic jets, which on collection deposits the ultrafine fibres. Environmental parameters such as temperature, relative humidity and atmospheric conductivity are some of the most difficult and expensive parameters to control in a practical manner as they require a climate-controlled facility. However, by an understanding of the inter-relationships of common processing parameters towards the equilibrium between the electrostatic and viscoelastic instabilities, which result in electrostatic jets, a control of fibre scaffold consistencies would become possible without significant increases in production costs.

Polycaprolactone (PCL, M_w = 80,000) is a long chain polyester that is naturally degraded by hydrolysis or via the tricarboxylic acid cycle. Using between 5-20% in ratios of chloroform and dichloromethane PCL solutions were electrospun by variations of several processing parameters against the effects of environmental humidity and temperature (parameters that were not controlled for). To minimise as much day-to-day variation as possible, a fume hood at a constant flow rate of 1 m s^{-1} air was used. Parameter combinations that resulted in an electrospray were discarded.

4.1. Practical Approach

Given the complexity of the electrospinning process, a practical approach was used initially to simplify and logically quantify the relationships between processing parameters and final fibre diameters. Following the production of aligned fibre scaffolds, samples were taken from the densest regions for scanning electron microscopy. Five to eight frames of the scaffold samples were taken on imaging for a decent estimate of the

density of fibres to select for use in cultures. An approximate total of 100 ±50 fibres per sample was taken from the images combined. Distribution analyses of fibre diameters demonstrated a predominant log-normal character for all sample scaffolds. As such, all fibre diameters are quoted as the median and 95% confidence levels (or the range of fibre diameters that 95% of measured fibres would fall into) derived and de-transformed from their respective log-distributions.

4.1.1. Effects of Relative Humidity

In electrospinning, the phenomenon of winter vs. summer fibre scaffolds is well known, which could be attributed to the difference in relative humidity (ϕ). To assess the precise effects of relative humidity on fibre morphology two identical sets of electrospinning experiments were conducted both in winter and in summer, which corresponded to 15.42% ϕ and 45.05% ϕ respectively. In general, an increase in humidity favoured the production of thicker fibres, with the most dramatic increase in diameter observed for those electrospun at 1 ml/hr flow rate (Q); from 307 nm (95% C.I. = 247-381nm, n=113) to 383nm (95% C.I. = 304-481 nm, n=68) at 0.3 ml/hr and 285 nm (95% C.I. = 223-364nm, n=102) to 962 nm (95% C.I. = 956-969nm, n=115) at 1 ml/hr, fig 4.1A. It was also observed that at 15.42% ϕ, fig 4.1B, the variances between the relative alignments of ultrafine fibres produced at both flow rates were fairly consistent (F-test: p > 0.05).

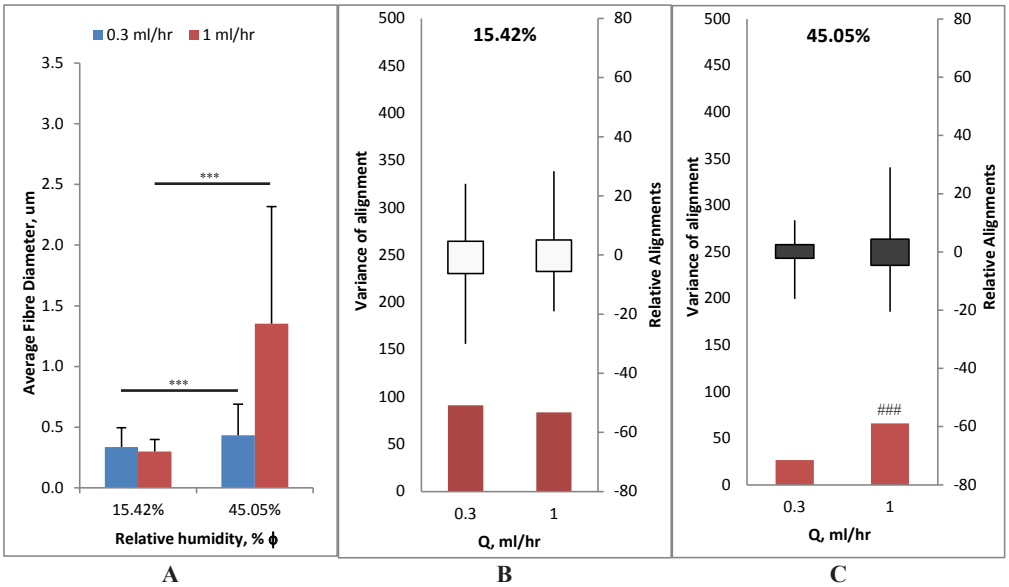

Fig 4.1: Effect of relative humidity on fibre diameter (**A**) and relative alignments (**B** and **C**). Constant parameters are as follows: T (temperature) = 21 °C, 25% chloroform in DCM, V (voltage) = 13 kV, v (velocity of rotating drum) = 660 m/s, [PCL] = 8%, Needle (dimensions) = 0.55 x 40 mm, y (distance from capillary to collector) = 15 cm, ** p (t-test) < 0.005, *** p < 0.0005, ### f (F-test: p) < 0.0005, n = 1

However, at 45.05% ϕ, fig 4.1C, the same could not be said (F-test: $p < 0.0005$). Although the increase of relative humidity at 0.3 ml/hr improved relative alignments (F-test: $p < 0.0005$) there was an insignificant decrease at 1 ml/hr (F-test: $p > 0.05$). This suggests that the variation of flow rate alone could not be used to minimise the effects of the fluctuation of relative humidity.

4.1.2. Effects of Concentration

The concentration of a polymer in solution affects the overall viscosity which can limit the influence of changes in relative humidity. PCL at concentrations of 8 % w.t. and 10 % w.t. ([PCL]) were electrospun at 56% ϕ to produce fibres of 323 nm (95% C.I. = 266-323 nm, n=130) and 367 nm (95% C.I. = 304-442 nm, n=111) respectively (t.test: $p < 0.05$), fig 4.2A. Although the relative alignments of nanofibres generated using PCL at 8% w.t. solution was found to be less consistent (F-test: $p < 0.05$) the overall distribution of alignment deviations, fig 4.2B, were of an acceptable level. This suggested 8% w.t. [PCL] might be a better concentration to produce nanofibres. However, it must be noted that the relatively high relative humidity within which these scaffolds were electrospun might actually favour the electrospinning of high consistency aligned nanofibre scaffolds from low PCL solution concentrations due to the slower rates of solvent evaporation.

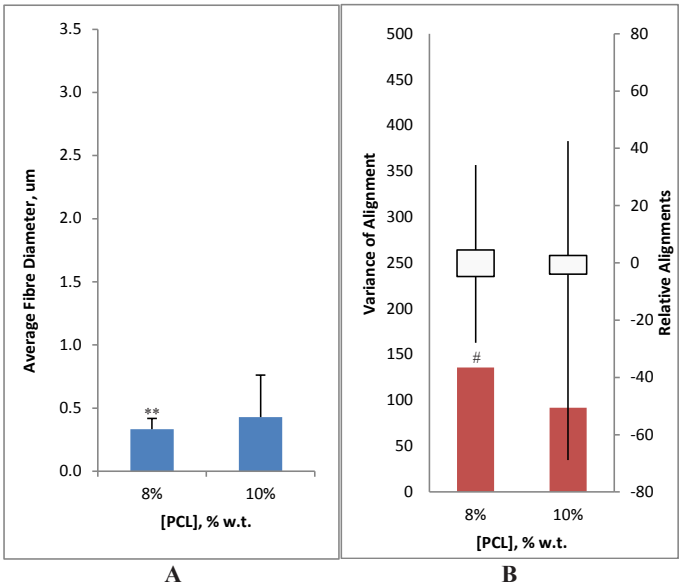

Fig 4.2: Effect of PCL concentration on fibre diameter in μm (**A**) and alignment (**B**). Constant parameters are as follows: T = 19 °C, ϕ (relative humidity) = 56%, 25% chloroform in DCM, V = 20 kV, v = 660 m/s, Q (flow Rate) = 0.3 ml/hr, y = 12 cm, Needle = 0.5 x 16 mm, ** $p < 0.005$, # $f < 0.05$, n = 1

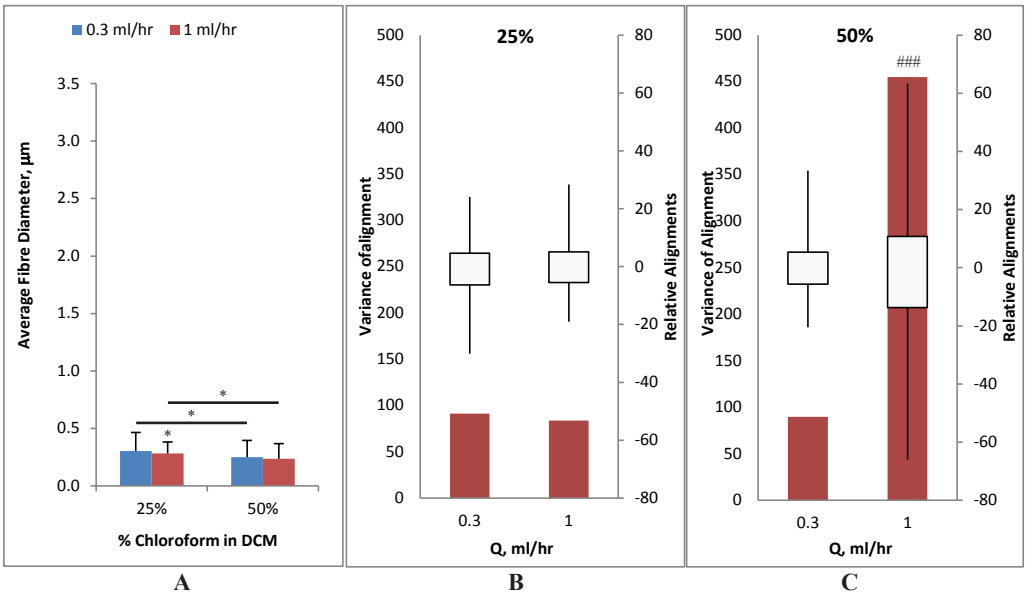

Fig 4.3: Effect of solvent system on fibre diameters in µm (**A**) and alignment (**B** and **C**). Constant parameters are as follows: T = 19.5 °C, ϕ = 15%, V = 13 kV, v = 660 m/s, [PCL] (concentration of PCL) = 8% w.t., needle = 0.55 x 40 mm, y = 15 cm, * $p < 0.05$, ### $f < 0.0005$, n = 1

4.1.3. Effects of Solvent System

A good use of solvent systems in electrospinning can determine the quality and consistency of deposited fibres as the Rayleigh limits and polymer relaxation times are affected. At 15% ϕ Dichloromethane (DCM), a polar solvent with a relatively good permittivity to charge, was supplemented with less polar but more electron-dense solvent, chloroform, at 0%, 25% and 50% to dissolve 8 % w.t. PCL. The electrospinning of 0% chloroform-DCM polymer solution generated an electrospray rather than a jet and was subsequently removed from further analyses. For the other two solutions they were both electrospun at 0.3 ml/hr Q and 1 ml/hr Q, fig 4.3. With the increase in chloroform percentage a consistent decrease of approximately 15% was observed in mean electrospun fibre diameters. At 0.3 ml/hr flow rate the mean diameters decreased from 307 nm (95% C.I. = 247-381nm, n=113) to 285 nm (95% C.I. = 223-364nm, n=102) and at 1 ml/hr Q it decreased from 259 (95% C.I. = 189-354 nm, n=71) to 231 nm (95% C.I. = 173-311 nm, n=96). However, when the alignment data for both solvent ratios were compared, the use of 25% chloroform in DCM produced more consistent fibres between the two flow rates (F-test: $p = 0.32$, fig 4.3B) as opposed to the dramatic changes seen for 50% chloroform in DCM (F-test: $p < 0.0005$, fig 4.3C). This suggests 25% chloroform in DCM is a better solvent system for increasing fibre consistency at 15% ϕ.

4.1.4. Effects of Voltage and Flow Rate

The voltage and flow rates are two complementary factors in electrospinning that both affect the volumetric charge density and therefore the generation of electrostatic jets. At 44% ϕ the increase in voltage, from 13kV to 20kV, generated a general decrease in diameter: 383nm (95% C.I. = 304-481nm, n=68) to 363nm (95% C.I. = 308-429 nm, n=147), p = 0.87, at 0.3 ml/hr; 1.013 μm (95% C.I. = 1.010-1.016 μm, n=100) to 756 nm (95% C.I. = 715-799 nm, n=98), p < 0.05, at 1 ml/hr; and 962 nm (95% C.I. = 955-969 nm, n=115) to 604 nm (95% C.I. = 527-693nm, n=55), p < 0.05, at 2 ml/hr.

On comparison of flow rates, significance was observed between 1 ml/hr Q and 2 ml/hr Q samples against 0.3 ml/hr samples for both voltages (ANOVA: p < 0.0005). Although 1 ml/hr and 2 ml/hr samples showed a slight decrease in fibre diameter at 20kV, no overall significance was observed.

Increasing flow rate at 13kV decreased relative alignments (fig. 4.4B) but a significant improvement was observed at 20kV (fig. 4.4C). However, given the distinct pattern observed against flow rate, statistical analyses between relative alignments against changes in voltage would be uninformative.

Overall, the effects of flow rate increased fibre diameters although it decreased relative fibre alignments when electrospun at 13kV, whilst increasing relative alignments

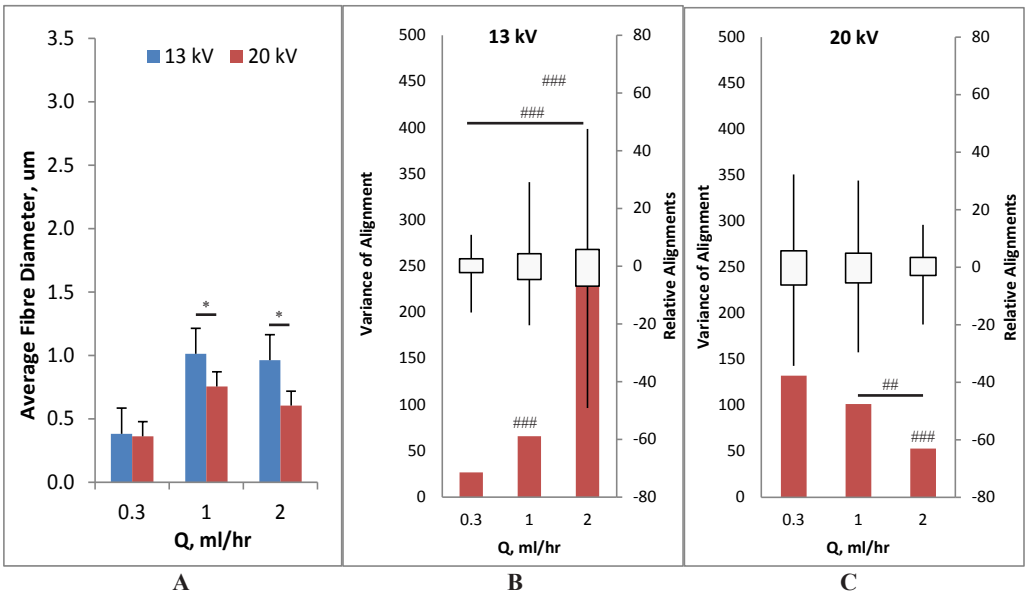

Fig 4.4: Effect of voltage and flow rate on fibre diameter in μm (**A**) and alignment (**B** and **C**). Constant parameters are as follows: T = 23 °C, ϕ = 44%, 25% chloroform in DCM, v = 660 m/s, [PCL] = 8% w.t., Needle = 0.55 x 40 mm, y = 15 cm. * p < 0.05, *** p <0.0005, ## p <0.005, ### f < 0.0005

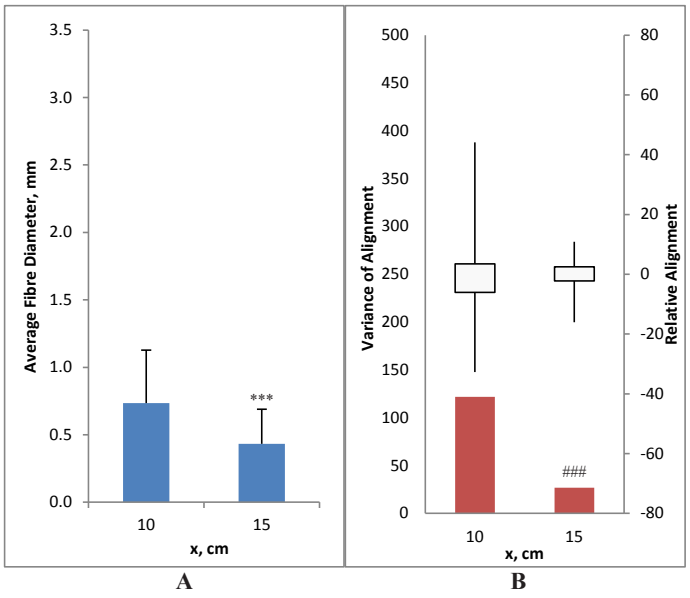

Fig 4.5: Effect of distance between capillary and collector on fibre diameter (**A**) and alignment (**B**). Constant parameters are as follows: T = 22 °C, ϕ = 48%, 25% chloroform in DCM, V = 13 kV, v = 660 m/s, Q = 0.3 ml/hr, [PCL] = 8% w.t., Needle = 0.55 x 40 mm, *** $p < 0.0001$, ### $f < 0.0005$, n = 1

at 20kV. In comparison an increase in voltage generally decreased fibre diameters except for samples electrospun at 0.3 ml/hr. However, this indicated that there was no distinct correlation to specify the precise relationship between flow rate and voltage.

4.1.5. Effects of the Distance between Capillary and Collector

The distance between the charged capillary and grounded collector (x) influences the gradient of the electric field along which the electrostatic jet stretches to form the fibres. At 48% ϕ the increase of x from 10 to 15 cm, of otherwise identical experiments, decreased the mean fibre diameter from 640 nm (95% C.I. = 587-698 nm, n=101) to 383 nm (95% C.I. = 304-481 nm, n=68), $p < 0.0001$, fig 4.5A. The increase in x was also found to improve the relative alignments (F-test: $p < 0.0001$, fig 4.5B). This suggests that a greater distance, or a gentler gradient down the electric field, would be more beneficial in increasing scaffold consistency.

4.2. Secondary Parameter Approach

Practical experimental studies identified the unfeasibility of employing simple/primary controls of processing parameters towards the electrospinning of select submicron fibres.

This was due to the complexity and indirect relationships between physical parameters and the final fibre morphology and orientations. Theoretical studies of electrospinning established the standard model[200,204] put forth by the groups of both Reneker and Yarin, which formed the basis for further developments and engineering in this field. However, the application of such models towards the production of aligned fibre scaffolds for biological studies in standard laboratories is limited due to their incapability of predicting fibre and fabric morphology, as that can influence cell differentiation and survival. In addition, the range of composite secondary parameters used for the standard model is almost as numerous and intricate as those used in practical approaches thus further limiting their broader adoption.

Another major limitation to the adoption of current theoretical models as secondary controls to the electrospinning process is the consideration of the underlying physics behind the generation[201,220] and properties[221,222] of induced Taylor cones, charge break-ups under Rayleigh limits[223] and the rate of solvent evaporation. Reviews of latent theoretical literature[220,222,224,225] as well as studies into solution composite interactions[209,226] provided insight into potential reductions towards a simplified, yet practically applicable, model of electrospinning. Using data from practical electrospinning experiments and knowledge obtained from literature review, a simplification of the electrospinning model is attempted via the use of multivariate ANOVA of primary and secondary parameters against measured scaffold morphology.

Previous assessments suggested a log-normal distribution of scaffold fibre diameters and were subsequently evaluated as such in multivariate ANOVA (ANOVA

	Polycaprolactone	**Chloroform**	**Dichloromethane**
molecular weight, M_r, mg/mmol	80,000	119.38	84.93
relative permittivity, ε_r	3.235	4.8069	9.08
viscosity, μ, mg/(mm.s)	139.5699 (VBN)	1.5262-0.0018T	1.5247-0.0037T
density, ρ, mg/mm^3	1.1450	2.0315-0.0018T	1.325
surface tension, γ, mg/s^2	51000.0	64139.176-128.4T	65461.63-129.5T
Vapour pressure, P_v, 10^9 mg/(mm.s^2) $\ln P_v = A \ln T + B/T + C + DT^2$			
Antoine's constant A	-	-10.07089	-10.08632
Antoine's constant B	-	-6351.140	-6030.610
Antoine's constant C	-	81.14393	80.87786
Antoine's constant D	-	9.127608	9.812512

Table 4.1: Values Used in Electrospinning Model Transformations. Constants: Permittivity of free space, ε_0: 8.85418782 x 10-15 C/(V.mm); Coulombs Constant, k_e: 8.9875517873681764 x 10^{12} (mm.V)/C; Relative permittivity of water: 80.1; Relative permittivity of dry air: 1.00058986

Eq 4.1: Refutas' equation of viscosity blends. **a**: transformation of dynamic (absolute) viscosity (μ) into kinematic viscosity (ν) necessary for the calculation of viscosity blend number (VBN); ρ = density. **b**: calculation of VBN for pure components (i). **c**: summation of all VBN accounting for their mole fractions (x), VBN_b. **d**: to obtain overall ν. To obtain overall μ, the composite ν was multiplied by the overall density. This equation is for viscosities measured in cSt.

$$\nu = \frac{\mu}{\rho} \quad \textbf{a}$$

$$VBN = 14.534\ln[\ln(\nu + 0.8)] + 10.975 \quad \textbf{b}$$

$$VBN_b = \sum x_i VBN_i \quad \textbf{c}$$

$$\nu = \exp\left(\exp\left(\frac{(VBN_b - 10.975)}{14.534}\right)\right) - 0.8 \quad \textbf{d}$$

for simplicity from hence forth; N=75). Given that collector spin rate and dimensions of focusing ring were kept constant throughout, they were temporarily eliminated from analyses. Preliminary ANOVA of primary parameters identified 352 possible combinations, with 115 of them showing significance ($p<0.05$, Appendix B). Reduction of parameters will initiate with logical transformation of simple combination in a stepwise fashion until the minimum independent parameters are reached. System constants are summarised in table 4.1.

4.2.1. Solution Parameters

Chemical compositions contribute towards the electrospinning process in unison. In terms of electrospinning there are three main solution parameters that may affect fibre morphology: solution viscosity (μ), surface tension (γ) and electrical permittivity (ε).

Solution viscosity, μ, describes a fluid's resistance to deformation against external stresses. For the current study, it is estimated via the Refutas' equation of viscosity blends (eq. 4.1) using values calculated from recorded correlations with absolute temperature.

The surface tensions of pure components were found to be similar and as such the overall surface tension was approximated by the mole fractions of each component once the effects of temperature had been factored in.

Eq 4.2: **a**: Oster's rule on overall polarisation, pm, of composite medium. v_i = molar volume of pure component i, p_i = polarisation of pure component i. **b**: Kirkwood's theory on polarsation against permittivity, ε. The overall permittivity was calculated using the reverse of **b**.

$$p_m = \frac{\left(\sum^n{}_i x_i v_i p_i\right)}{\left(\sum^n{}_i x_i v_i\right)} \quad \textbf{a}$$

$$p = \frac{((\varepsilon - 1)(2\varepsilon + 1))}{(9\varepsilon)} \quad \textbf{b}$$

The electrical permittivity, ε, describes the susceptibility of a dielectric medium to permit the transmission of charge under an electric field. It is also a good indicator of how well a polymer solution can form Taylor cones. The overall permittivity is estimated by the application of Oster's rule on Kirkwood's theory on the relationship between polarisation and permittivity[227] (eq. 4.2).

Following such transformations, ANOVA was conducted for the interactions between relative humidity (ϕ), surface tension (γ), viscosity (μ), electrical permittivity of solution (ε), needle diameter, needle length, flow rate (Q), voltage (V), and distance between needle tip and collector (y). The number of interactions decreased to 182, with 74 significant combinations of parameters on scaffold fibre diameter observed.

4.2.2. Environmental parameters

Environmental parameters in electrospinning are predominantly the temperature and relative humidity. Given that temperature had mostly been factored into solution parameters, focus at this stage is on the effects of relative humidity. The relative humidity affects fibre morphology in two major ways. The first way is via its effects on the permittivity of the humid air during the propulsion of electrostatic jets (calculated as before, using values quoted for dry air and water). The other is on the rate of solvent evaporation.

The rate of evaporation is commonly predicted using the Langmuir's equation, which is dependent on the air pressure and the vapour pressure of the evaporating liquid. Extended Antoine's equations for the pure solvents were first applied to obtain their respective vapour pressures at the measured absolute temperature for each sample. These pressures were then proportionally calculated into Raoult's law to form the vapour pressure of the electrospun solution. As the loss of mass is difficult to predict in electrospinning, the difference between humid air pressure and polymer vapour pressure is taken as an indicator instead.

Following these transformation ANOVA of the needle diameter, needle length, flow rate, y, viscosity, difference between vapour pressure (P_{diff}), voltage, surface tension, permittivity of humid air and solution permittivity yielded 265 different parameter interactions, with 86 of them showing significance. Following this, it was of note that

$$D = \varepsilon(E_1 + E_2) \quad \textbf{a}$$

$$E_1 = \frac{(k_e q_1)}{(a(l+a))} \quad \textbf{b}$$

$$E_2 = \frac{(k_e x q_2)}{\left((R_1)^2 + x^2\right)^{1.5}} \quad \textbf{c}$$

$$q_1 = 2\pi\varepsilon l \frac{V}{\Lambda}\left\{1 + \frac{1}{\Lambda}(1 - \ln 2) + \frac{1}{\Lambda^2}\left[1 + (1 - \ln 2)^2 - \frac{\pi^2}{12}\right] + \frac{1}{\Lambda^3}\right\}, \Lambda = \ln\frac{l}{A} \quad \textbf{d}$$

$$q_2 = 2\pi\varepsilon w \frac{V}{(\ln(R_2) - \ln(R_1))} \quad \textbf{e}$$

Eq. 4.3: Calculation of electric displacement field, D. **a**: the electric displacement field of the system. ε = permittivity of the humid air. **b**: electric field due to the charged polymer solution held in needle. k_e = Coulomb's constant. $\boldsymbol{a}$ = distance of point to tip of rod, taken to be equivalent to the radius of needle bore where the Taylor cone approximately forms . $\boldsymbol{\ell}$ = length of needle. **c**: electric field due to the charged focusing ring. $\boldsymbol{x}$ = perpendicular distance of point to central plane of focusing ring, measured to be halfway along needle plus $\boldsymbol{a}$. R_1 = radius of needle. **d**: total charge induced into the polymer solution within needle. ε = permittivity of polymer solution. V = applied voltage. **e**: total charged induced due to the charged ring. ε = permittivity of humid air. $\boldsymbol{\omega}$ = width of focusing ring. R_2 = radius of focusing ring.

the predominant decrease was on the level of complex parameter interactions which showed significance.

4.2.3. Electric Displacement field, D

The electric displacement field is defined as the polarization of a medium under a potential difference. It is an important factor in electromagnetism and accounts for the ease/difficulty for charge to pass through the induced electric field. In simple dielectrics, i.e. air, it is estimated from the electric field multiplied by the permittivity of the local medium (eq. 4.3). It is calculated from the potential difference in the system, the permittivity of the medium, the dimensions of the charge inducers and the distance between the charge inducers and point of interest in space – taken to be the transition zone at the Taylor cone apex assumed to be equivalent to the radius of the needle bore. In the current electrospinning set-up, the overall electric field is generated by both the focusing ring (eq. 4.3.a) and the charged solution segment contained within the syringe needle (eq. 4.3.b).

The revised ANOVA model now contained the electric displacement field, the flow rate, y, viscosity, surface tension and P_{diff}. This conveniently decreased the interacting parameters to 63, with 47 significant interactions.

$$\rho_q = \rho_v \frac{d_0}{4} \quad \text{a}$$

$$\rho_v = \frac{q_1}{(Al)} \quad \text{b}$$

$$d_0 = \sqrt[3]{\left(\rho_v \frac{Q^2}{\gamma}\right)} \quad \text{c}$$

Eq 4.4: **a**: surface charge density[197]. **b**: volumetric charge density. q_1 = total induced charge of polymer solution, calculated from eq 4.3.d. A = cross-sectional area of needle. ℓ = length of needle. **c**: predicted initial electrostatic jet diameter[191]. Q = volumetric flow rate. γ = solution surface tension.

4.2.4. Surface Charge Density, ρ_q

In a dielectric material, induced charge is predominantly distributed about the surface area. In the current system, the only exposed surface of the polymer solution is located at the needle tip, where the Taylor cones form as a result of charge build-up under the induced electric field. The level of charge build-up could be predicted using the parameter surface charge density, ρ_q. This was calculated from the equation proposed by Theron *et al*[228], eq 4.4, with the volumetric charge density (ρ_v, eq 4.4.a) and initial jet diameters[222] (d_0, eq 4.4.b) approximated as shown.

The new set of parameters analysed via ANOVA now became the electric displacement field, the surface charge density, flow rate, P_{diff}, y and viscosity. Of the 63 interacting parameters, a slight decrease to 41 significant interactions on fibre diameter was observed.

4.2.5. Reynolds number, Re

Apart from surface charge density, solution flow rate was found to have significant interactions with viscosity on the diameter of deposited polymer fibres. Due to the dynamic, and potentially turbulent, flow of the polymer solution caused by the effects of an electric field, the Reynolds number was used for model simplification (eq 4.5). The Reynolds number is a dimensionless parameter that factors in the flow rate and the kinematic viscosity (ν) to account for the fluid's internal ratio between inertial and viscous forces; the solution's resistance to changes in velocity and friction between

$$\mathrm{Re} = Q \frac{d}{(\nu A)}$$

Eq 4.5: Calculation of the Reynold number, Re. Q = volumetric flow rate. d = diameter of the needle. n = kinematic viscosity. A = cross-sectional area of needle

constituent particles, respectively.

Multivariate ANOVA of the new reduced list of parameters (electric displacement field, surface charge density, Re, P_{diff} and y) identified 31 different combinations, with 25 of them showing significance.

4.2.6. Parameter Effects on fibre alignment

Following their identification secondary parameters were compared against fibre alignments. Three dimensional plots of the individual residual degrees against two of the parameters at a time identified the distance between needle tip and collector (y), electric displacement field (D), and surface charge density to have the greatest effects, fig 4.6A and fig 4.6B. The Reynolds number (Re) also showed slight effects (fig 4.6C) although the difference in vapour pressures, P_{diff}, did not appear to have an effect (fig 4.6D).

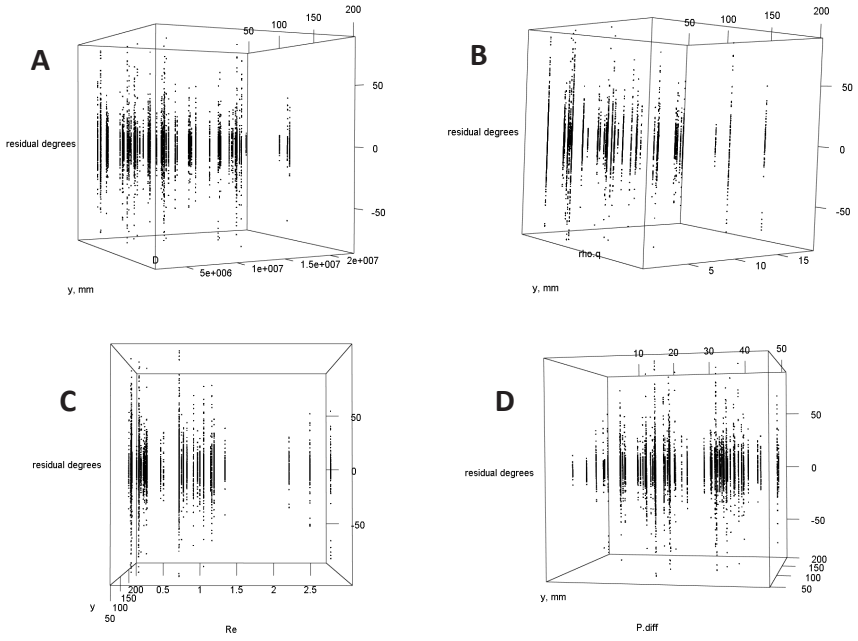

Fig 4.6: 3D plots of residual degrees (degrees away from mean) versus distance between needle tip and collector (y) and electric displacement field (D, **A**), surface charge density (rho.q, **B**), Reynolds number (Re, **C**) or difference between air and solvent vapour pressures (P.diff, **D**). Significant reductions in the distribution of residual degrees was observed for increases in y, D and rho.q. Although an effect was observed for the change in Reynolds number it is unreliable due to the low sample count of high Reynold numbers. However, evaluation of the effects of P.diff on the distribution of residual degrees proved to be inconclusive.

5. Discussion

Scaffold studies in the development of an *in vitro* human motor neuron disease (MND) model identified the preference of both the motor neuron cell line NSC34 and E13 primary spinal cord dissociates for submicron fibre scaffolds. As a result, subsequent studies were divided into two parts: i) the continued development of the *in vitro* model and ii) the reduction of processing parameters for the controlled production of aligned submicron fibre scaffolds.

5.1. Development of MND Model

In vitro MND models were developed in the present study using electrospun aligned fibre scaffolds that were originally designed for peripheral nerve regeneration. This was primarily to serve two general purposes. Firstly, the use of ultrafine fibres can artificially generate gap distances between fibres to >2μm which had been proven to control neurite growth[142,229]. Secondly, work conducted using *ex vivo* dorsal root ganglia[14] and dissociates[215] have suggested the use of submicron fibres can stimulate greater elongation of axons with ~300nm diameter fibres proven to be the best[215]. Results from the present study using NSC34, a neuroblastoma cell line that resembled early motor neurons[139], and primary E13 murine spinal cord dissociates agreed with previous studies.

In order to understand the effects of fibre diameter on the development of *in vitro* MND models the process of neuroblast differentiation into mature neurons would need to be investigated. Early research identified 5 stages of this process in hippocampal neurons that could be loosely translated for all other neuronal cell types[230]. In brief, spherical neuroblast first generates filopodia at the periphery to facilitate attachment onto substrates (stage 1). In stage 2, migration of filopodia drives the formation of growth cones that subsequently form processes/neurites. As neurites elongate one would selectively form the axon (stage 3) whilst all others retract and develop into dendrites (stage 4). The final stage in this process would be the formation of synapses ready for use in signal transmission.

Topographical features are principal effectors of submicron fibres on neurite

development[229]. The very small diameters of submicron fibres dramatically reduce the available surface area for environmental sensing[109] of filopodia. This pre-determines the migratory path of the developing growth cones which restricted the degree of dynamic assembly and disassembly of filamentous actin (F-actin)[22,231,232]. Consequently, the engorgement of microtubule molecules[233] elongates the developing neurite and drives the early entry into stage 2 of neuronal development[142,234]. In addition, stage 3 of neuron maturation (axon formation) is governed by the competition of the variable combinations of topographical and extraneous influences experienced by individual neurites[235]. However, physical limitations imposed by submicron fibres significantly favour neurites that grew parallel to the orientation of the fibres into forming axons, thus reducing the time required before the appearance of dendrites. Although not explicitly discussed by Christopherson *et al*[215] the earlier formation of axons could explain the elevated presence of dendrites and oligodendrocytes observed in their study on the differentiation of neural stem cell culture on submicron fibre meshes.

One of the questions raised from the present study was the decrease in cell count observed in NSC34 cultures on fibre scaffolds when compared to flat surface controls. With a lack of stimulating factors that can induce neuron maturation except for universal serum reduction, it is possible to attribute this decline to the use of the fibre scaffolds. Neuroblasts are mitotic cells that would enter a state of quiescent when sufficient non-mitotic neurons have been generated to establish a neural network[236]. In embryogenesis, the entry into the dormant state typically follows an explosion in neural stem cell numbers superseded by apoptosis of excess neuron progenitors. Although NSC34 is a transformed cell line, similar patterns of behaviour have been unofficially observed with increasing age of samples used in experiments; which led to the decision to only use cells between passages 13 to 20. However, given the fact that submicron fibres drive early maturation of neurons, and the fact that limited amounts of morphologically apoptotic cells were observed in NSC34 cultures, it raises several questions that will be of interest for further investigation. Principally, would the decrease in cell count of NSC34 cultured on aligned fibre scaffolds be caused by a) an increase of apoptosis typical of neural network formation; or b) early entry into quiescence of non-differentiated neuroblasts?

The effects of aligned submicron fibre scaffolds were also studied on both primary murine motor neurons and spinal cord dissociates (PSD). Primary motor neurons

are highly sensitive to their culture conditions which had often restricted their survival *in vitro* to less than 6 days, which was the experimental period used in the present study. Following literature review, the lack of motor neuron survival in the current project is most likely caused by the use of serum rather than the presence of the scaffolds as demonstrated by Gertz *et al* who have successfully cultured primary motor neurons on submicron fibre scaffolds using serum-free media[217,237].

Primary spinal cord dissociates (PSD) consists of a mixture of neurons, astrocytes and oligodendrocytes that act synergistically to support each other's survival. As expected, aligned submicron fibre scaffolds were most able to increase the immunoreactivity to β-Tubulin III, indicative of differentiated neurons. In the development of MND models, tentative adhesion and clustering of early PSD models stimulated an investigation into the potential use of laminin or poly-L-lysine (PLL) coating on PCL fibres. When the coatings were compared against nude PCL fibres, the laminin coatings provided the best response as shown by immunolabelling for neurons and glia, which was followed by the use of PLL coating. PLL is a common coating used in *in vitro* culture of neurons by providing an adhesive surface for cells to adhere. Biologically, they are inert and there is evidence that simple adhesion is insufficient to support the maturation of primary neurons[232,235]. Comparatively, laminin is a ligand to the transmembrane integrin receptor that is involved in cytoskeletal reorganisation and neurite growth[41]. Although, it is capable of supporting axon elongation during stage 3 in neuron maturation[142,235,238], once the developing neurons had entered into stage 4 they appeared to lose their sensitivity to laminin[239]. However, in regenerating mature neurons it appeared that this response can be restored via alternative pathways following modification to laminin[240].

The interaction between motor neurons, astrocytes and oligodendrocytes is an emerging factor when considering the pathophysiology of MND. Early models in the present study using 1.5×10^6 cells per 6-well identified good associations between neuron and glia. Encapsulation of fibres and neurites by glia were observed as expected, as well as the occasional morphological features typical of differentiating oligodendrocytes. However, the very high cell density of these models affected quantitative analyses that led to a reduction in cell counts to 900,000/6-well in subsequent experiments. Although model visibility did improve, neuron/neurite densities were still sufficiently high to hinder quantitative analyses. Furthermore, the loss of the glial signals could potentially be attributed to the glia-inhibitory nature of the neurobasal media. Alternatively, it may

be indicative of the incomplete maturation of astrocytes or due to an insufficient density of oligodendrocytes[241]. In order to better develop *in vitro* co-culture human MND models, it will be necessary to have a baseline study of pure astrocytes, oligodendrocytes and motor neurons to better decipher the mystery of the neuron-glial interactions.

5.2. Electrospinning

Increasing evidence is pointing towards the benefits of nanofibres in the differentiation of motor neurons[216,217]. However, the generation of nanofibres are limited by the high sensitivity of electrospinning to environmental factors which is difficult to control. Building upon the theoretical models established by Thompson *et al*[200], Theron *et al*[228], Tan *et al*[242] and many others an alternative approach was devised to identify potential simplifications to the control of submicron electrospinning.

When considering limiting factors in the controlled electrospinning of aligned submicron fibres two principal processes are of primary concern: i) formation of Taylor cones[201]; and ii) stretching of electrostatic jets[197]. These processes are both derived from different combinations of primary parameters all contributing towards the dynamic equilibrium between electrostatic and viscoelastic instabilities.

The formation of Taylor cones is caused by peaks in dynamic surface charge densities which are sufficiently rich in potential energy to modify surface topography. This energy is chiefly generated by the applied voltage (V) on the dielectric polymer solution which leads to an accumulation of charge in the enclosed volume of the needle, described by the term volumetric charge density (ρ_v)[200]. However, ρ_v is dependent on the overall electrical permittivity (ε) of the polymer solution used[226,243,244]. In order to generate the electrostatic jet, the accumulated potential energy would have to be sufficient to break surface tension (γ)[220,245] yet low enough to not exceed the Rayleigh limit which would result in an electrospray[223,246]. To limit the potential for the formation of an electrospray, the viscosity (μ)[200,207,228,247] is typically manipulated by the use of high molecular weight polymer chains. Yet, the viscosity has to be tightly controlled so as to limit the size of the generated Taylor cone and the initial jet diameter (d_0)[220] for the electrospinning of submicron fibres. Finally, application of liquid flow rate (Q) and the

electric displacement field (D) impose directionality on jet migration, thereby initiating the stretching of the electrostatic jet.

After the formation of the electrostatic jet the electric displacement field, determined by the electric field and the electrical permittivity of humid air, drives their migration towards the grounded collector. As charge and solvent components are lost as the jet migrates (the rate of which is determined by the vapour pressure calculated from relative humidity) subsequent changes to the interdependent viscosity and surface tension[248,249] of polymer solutions stimulate the stretching or bending instability of the electrostatic jet[204,205]. It is this process which further decreases the diameter of the electrospun fibres.

Unexpectedly, multivariate ANOVA on the data obtained in the present study drew attention to the interaction between needle length and diameter, and the electrical permittivity of both the polymer solution and of the electrospinning space. On review, these parameters were identified to be those required for the calculation of capacitance, which when combined with the interacting voltage provided the overall charge of the system. In the set-up employed for the current study there were two separate sources of charge: i) from the focusing ring acting on the system; and ii) from the syringe needle acting on the flowing polymer solution. These two parameters, once matched with their equivalent electric field calculations, could be used in the calculation of electric field at specific points in the system; taken as the point where Taylor cones are most likely to form, located one radius away from the tip of the needle. Once calculated, the two electric fields could then be combined and multiplied by the electrical permittivity of the system to form the electric displacement field which described the electrostatic drive of the induced polymer jet.

From the remaining combinations of parameter interactions, significance was observed between flow rate and viscosity. These two factors can each be used to describe the inertial and viscous forces respectively. The ratio between the two forces can be defined by a parameter known as the dimensionless Reynolds number. This is a useful parameter as it predicts the nature of the solution fluid flow. If high Reynolds numbers were obtained, it is very likely that the flow of the electrostatic jet is highly turbulent and an increase in the variance of measured fibre diameters are likely, or beads may easily be formed.

Following numerous transformations, the total number of parameters was reduced to a total of 5 (electric displacement field, surface charge density, Reynolds number, difference between vapour pressures and the distance between needle tip and the collector). However, significance was still observed in the interactions between parameters following multivariate ANOVA. This suggests that further reductions to the number of processing parameters is possible, although that would require further research into fluid dynamics and electrostatics.

5.3. Concluding Remarks

In the present study the use of aligned submicron fibre scaffolds have been confirmed to support the differentiation of NSC34 cells. E13 murine spinal cord dissociates cultured on fibre scaffolds had exhibited good neuron-glia associations. However, the lack of mature glial markers or individual neuron resolution of a lower culture density suggests the need for pure culture studies as well as modifications to co-culture models. On another positive note, successes in the generation of fibroblast-iPSC-derived motor neurons from ALS patients within the research group further enhanced the possibility of alternative human *in vitro* 3D model for MND.

The generation of aligned submicron fibre scaffolds is one of the more difficult processes in electrospinning due to the high sensitivity of fibre morphology to changes to any one of many parameters. Simplification studies via log-normal multivariate ANOVA following secondary transformations of physical parameters successfully reduced the number of controlling parameters to 5. However, significant interactions were still observed between them. This suggests that further reductions are possible, although more research into fluid dynamics and electrostatics would be necessary.

Bibliography

1. Aminoff, M. J. & Kerchner, G. A. in *Current Medical Diagnosis & Treatment* (eds Stephen J. McPhee & Maxine A. Papadakis) Ch. 24, 927-994 (McGraw Hill Lange, 2011).
2. Talbot, K. & Marsden, R. *Motor Neuron Disease: The Facts*. (Oxford University Press, 2008).
3. Mitchell, J. D. & Borasio, G. D. Amyotrophic lateral sclerosis. *Lancet* **369**, 2031-2041 (2007).
4. Hand, C. K. & Rouleau, G. A. Familial Amyotrophic Lateral Sclerosis. *Muscle and Nerve* **25**, 135-139 (2002).
5. Hervias, I., Beal, M. F. & Manfredi, G. Mitochondrial dysfunction and amyotrophic lateral sclerosis. *Muscle and Nerve* **33**, 596-608 (2006).
6. Shaw, P. J. & Ince, P. G. Glutamate, excitotoxicity and amyotrophic lateral sclerosis. *J Neurol* **244 [Suppl 2]**, S3-S14 (1997).
7. Heath, P. R. & Shaw, P. J. An update on the glutamatergic neurotransmitter system and the role of excitotoxicity in amyotrophic lateral sclerosis. *Muscle and Nerve* **26**, 438-458 (2002).
8. Irons, H. R. *et al*. Three-dimensional neural constructs: a novel platform for neurophysiological investigation. *J Neural Eng* **5**, 333-341 (2008).
9. Xu, T. *et al*. Electrophysiological characterization of embryonic hippocampal neurons cultured in a 3D collagen hydrogel. *Biomaterials* **30**, 4377-4383 (2009).
10. Kehoe, S., Zhang, X. F. & Boyd, D. FDA approved guidance conduits and wraps for peripheral nerve injury: A review of materials and efficacy. *Injury* **43**, 553-572, doi:10.1016/j.injury.2010.12.030 (2012).
11. Cunha, C., Panseri, S. & Antonini, S. Emerging nanotechnology approaches in tissue engineering for peripheral nerve regeneration. *Nanomedicine* **7**, 50-59 (2011).
12. Bell, J. H. A. & Haycock, J. W. Next Generation Nerve Guides: Materials, Fabrication, Growth Factors, and Cell Delivery. *Tissue Eng B* **18**, 116-128, doi:10.1089/ten.teb.2011.0498 (2012).
13. Mahoney, M. J., Chen, R. R., Tan, J. & Saltzman, W. M. The influence of microchannels on neurite growth and architecture. *Biomaterials* **26**, 771-778, doi:10.1016/j.biomaterials.2004.03.015 (2005).
14. Daud, M. F. B., Pawar, K. C., Claeyssens, F., Ryan, A. J. & Haycock, J. W. An aligned 3D neuronal glial co-culture model for peripheral nerve studies. *Biomaterials* **33**, doi:10.1016/j.biomaterials.2012.05.008 (2012).
15. Yang, F., Murugan, R., Wang, S. & Ramakrishna, S. Electrospinning of nano/micro scale poly(L-lactic acid) aligned fibers and their potential in neural tissue engineering. *Biomaterials* **26**, 2609-2610 (2005).
16. Yucel, D., Kose, G. T. & Hasirci, V. Polyester based nerve guidance conduit design. *Biomaterials* **31**, 1596-1603 (2010).
17. Dimos, J. T. *et al*. Induced Pluripotent Stem Cells Generated from Patients with ALS Can Be Differentiated into Motor Neurons. *Science* **321**, 1218-1221, doi:10.1126/science.1158799 (2008).
18. Felten, D. L. & Shetty, A. N. *Netter's Atlas of Neuroscience*. 2 edn, (Saunders Elsevier, 2010).
19. Debanne, D., Campanac, E., Bialowas, A., Carlier, E. & Alcaraz, G. Axon physiology. *Physiol Rev* **91**, 555-602, doi:10.1152/physrev.00048.2009 (2011).
20. Arimura, N. & Kaibuchi, K. Neuronal polarity: from extracellular signals to intracellular mechanisms. *Nat Rev Neurosci* **8**, 194-205 (2007).
21. Chevalier-Larsen, E. & Holzbaur, E. L. F. Axonal transport and neurodegenerative disease. *Biochim Biophys Acta* **1762**, 1094-1108, doi:10.1016/j.bbadis.2006.04.00 (2006).
22. Luo, L. Actin Cytoskeleton Regulation in Neuronal Morphogenesis and Structural Plasticity. *Annu Rev Cell Dev Biol* **18**, 601-635 (2002).
23. Kabsch, W. & Vandekerckhove, J. Structure and Function of Actin. *Annu Rev Biophys Biomol Struct* **21**, 46-76 (1992).
24. Van Den Bosch, L., Vandenberghe, W., Klaassen, H., Van Houtte, E. & Robberecht, W. Ca^{2+}-permeable AMPA receptors and selective vulnerability of motor neurons. *J Neurol Sci* **180**, 29-34 (2000).
25. Sanelli, T., Ge, W., Leystra-Lantz, C. & Strong, M. J. Calcium mediated excitotoxicity in neurofilament aggregate-bearing neurons in vitro is NMDA receptor dependent. *J Neurol Sci* **256**, 39-51, doi:10.1016/j.jns.2007.02.018 (2007).
26. Young, D. M., Jan, Y. N. & Jan, L. Y. in *From Molecules to Networks: An Introduction to Cellular and Molecular Neuroscience* (eds John H. Byrne & James L. Roberts) Ch. 6, 159-180 (Academic Press, 2009).
27. McCormick, D. A. in *From Molecules to Networks: An Introduction to Cellular and Molecular Neuroscience* (eds John H. Byrne & James L. Roberts) Ch. 5, 133-158 (Academic Press, 2009).
28. Baxter, D. A. & Byrne, J. H. in *From Molecules to Networks: An Introduction to Cellular and Molecular Neuroscience* (eds John H. Byrne & James L. Roberts) Ch. 7, 181-218 (Academic Press, 2009).
29. Mihailoff, G. A. & Haines, D. E. in *Fundamental Neuroscience for Basic and Clinical Applications* (ed Duane E. Haines) Ch. 25, 394-412 (Churchill Livingstone, 2006).
30. Levitan, I. B. & Kaczmarek, L. K. *The Neuron: Cell and Molecular Biology*. 3 edn, (Oxford University Press, 2002).
31. Cakir, T., Alsan, S., Saybasili, H., Akin, A. & Ulgen, K. O. Reconstruction and flux analysis of coupling between metabolic pathways of astrocytes and neurons: application to cerebral hypoxia. *Theoret Biol Med Model* **4**, 48 (2007).
32. Blackburn, D., Sargsyan, S. A., Monk, P. N. & Shaw, P. J. Astrocyte Function and Role in Motor Neuron

Disease: A Future Therapeutic Target? *Glia* **57**, 1251-1264 (2009).

33. Nishida, H. & Okabe, S. Direct Astrocytic Contacts Regulate Local Maturation of Dendritic Spines. *J Neurosci* **27**, 331-343 (2007).

34. Hartley, R. S., Margulis, M., Fishman, P. S., Lee, V. M.-Y. & Tang, C.-M. Functional Synapses Are Formed Between Human Ntera2 (NT2N, hNT) Neurons Grown on Astrocytes. *J Comp Neurol* **407**, 1-10 (1999).

35. Ndubaku, U. & de Bellard, M. E. Glial cells: Old cells with new twists. *Acta Histochem* **110**, 182-195 (2008).

36. Martini, R. The effect of myelinating Schwann cells on axons. *Muscle and Nerve* **24**, 456-466 (2001).

37. Wilkins, A., Majed, H., Layfield, R., Compston, A. & Chandran, S. Oligodendrocytes Promote Neuronal Survival and Axonal Length by Distinct Intracellular Mechanisms: A Novel Role for Oligodendrocyte-Derived Glial Cell Line-Derived Neurotrophic Factor. *J Neurosci* **23**, 4967-4974 (2003).

38. Byrne, J. H. & Shepherd, G. M. in *From Molecules to Networks: An Introduction to Cellular and Molecular Neuroscience* (eds John H. Byrne & James L. Roberts) Ch. 4, 111-132 (Academic Press, 2009).

39. Zochodne, D. W. *Neurobiology of Peripheral Nerve Regeneration*. (Cambridge University Press, 2008).

40. Paz Soldan, M. M. & Pirko, I. Biogenesis and Significance of Central Nervous System Myelin. *Semin Neurol* **32**, 9-14, doi:10.1055/s-0032-1306381. (2012).

41. Ivins, J., Yurchenco, P. D. & Lander, A. D. Regulation of neurite outgrowth by integrin activation. *J Neurosci* **20**, 6551-6560 (2000).

42. Davies, S. J. A., Goucher, D. R., Doller, C. & Silver, J. Robust regeneration of adult sensory axons in degenerating white matter of the adult rat spinal cord. *J Neurosci* **19**, 5810-5822 (1999).

43. Horner, P. J. & Gage, F. H. Regenerating the damaged central nervous system. *Nature* **407**, 963-970 (2000).

44. Banner, S. J. *et al*. The expression of the glutamate re-uptake transporter EAAT1 in the normal human CNS and in amyotrophic lateral sclerosis (ALS): an immunohistochemical study. *Neuroscience* **109**, 27-44 (2002).

45. Jeans, A. F. & Ansorge, O. Recent Developments in the Pathology of Motor Neurone Disease. *ACNR* **9**, 25-26 (2009).

46. Ferraiuolo, L., Kirby, J., Grierson, A. J., Sendtner, M. & Shaw, P. J. Molecular pathways of motor neuron injury in amyotrophic lateral sclerosis. *Nat Rev Neurol* **7**, 616-630, doi:10.1038/nrneurol.2011.152 (2011).

47. Anneser, J. M. H., Chahli, C., Ince, P. G., Borasio, G. D. & Shaw, P. J. Glial proliferation and metabotropic glutamate receptor expression in amyotrophic lateral sclerosis. *J Neuropathol Exp Neurol* **63**, 831-840 (2004).

48. Kersaitis, C. *et al*. Ubiquitin-positive inclusions and progression of pathology in frontotemporal dementia and motor neurone disease indentifies a group with mainly early pathology. *Neuropathol Appl Neurobiol* **32**, 83-91, doi:10.1111/j.1365-2990.2005.00704.x (2006).

49. Neumann, M. *et al*. Ubiquitinated TDP-43 in Frontotemporal Lobar Degeneration and Amyotrophic Lateral Sclerosis. *Science* **314**, 130-133, doi:10.1126/science.1134108 (2006).

50. Dal Canto, M. C. & Gurney, M. E. A low expressor line of transgenic mice carrying a mutant human Cu,Zn superoxide dismutase (*SOD1*) gene develops pathological changes that most closely resemble those in human amyotrophic lateral sclerosis. *Acta Neuropathol* **93**, 537-550 (1997).

51. Wallis, N., Zagami, C. J., Beart, P. M. & O'Shea, R. D. Combined excitotoxic-oxidative stress and the concept of non-cell autonomous pathology of ALS: Insights into motoneuron axonopathy and astrogliosis. *Neurochem Int* **51**, 523-30 doi:10.1016/j.neuint.2012.02.026 (2012).

52. Ferraiuolo, L., Kirby, J., Grierson, A. J., Sendtner, M. & Shaw, P. J. Molecular pathways of motor neuron injury in amyotrophic lateral sclerosis. *Nat Rev Neurol* **7**, 616-630, doi:10.1038/nrneurol.2011.152 (2011).

53. Andersen, P. M. & Al-Chalabi, A. Clinical genetics of amyotrophic lateral sclerosis: what do we really know? *Nat Rev Neurol* **7**, 603-615, doi:10.1038/nrneurol.2011.150 (2011).

54. Sasabe, J. *et al*. D-Amino acid oxidase controls motoneuron degeneration through D-serine. *PNAS* **109**, 627-632, doi:10.1073/pnas.1114639109 (2012).

55. Suzuki, H. *et al*. ALS-linked P56S-VAPB, an aggregated loss-of-function mutant of VAPB, predisposes motor neurons to ER stress-related death by inducing aggregation of co-expressed wild-type VAPB. *J Neurochem* **108**, 973-985 (2009).

56. Chen, H.-J. *et al*. Characterization of the properties of a novel mutation in VAPB in familial amyotrophic lateral sclerosis. *J Biol Chem* **285**, 40266-40281, doi:10.1074/jbc.M110.161398 (2010).

57. Maruyama, H. *et al*. Mutations of optineurin in amyotrophic lateral sclerosis. *Nat Lett* **465**, 223-227, doi:10.1038/nature08971 (2010).

58. Belzil, V. V. *et al*. Analysis of *OPTN* as a causative gene for amyotrophic lateral sclerosis. *Neurobiol Aging* **32**, 555.e513-555.e514, doi:10.1016/j.neurobiolaging.2010.10.001 (2011).

59. Jacquier, A., Bellouze, S., Blanchard, S., Bohl, D. & Haase, G. Astrocytic protection of spinal motor neurons but not cortical neurons against loss of Als2/alsin function. *Hum Mol Genet* **18**, 2127-2139, doi:10.1093/hmg/ddp136 (2009).

60. Vance, C. *et al*. Mutations in *FUS*, an RNA processing protein, cause familial amyotrophic lateral sclerosis type 6. *Science* **323**, 1208-1211, doi:10.1126/science.1165942 (2009).

61. DeJesus-Hernandez, M. *et al*. De novo truncating *FUS* gene mutation as a cause of sporadic amyotrophic lateral sclerosis. *Hum Mutat* **31**, 1377-1389, doi:10.1002/humu.21241 (2010).

62. Lee, E. B., Lee, V. M.-Y. & Trojanowski, J. Q. Gains or

losses: molecular mechanisms for TDP43-mediated neurodegeneration. *Nat Rev Neurosci* **13**, 38-50 (2012).

63. Tollervey, J. R. *et al*. Characterizing the RNA targets and position-dependent splicing regulation by TDP-43. *Nat Neurosci* **14**, 452-459, doi:10.1038/nn.2778 (2011).

64. Deng, H.-X. *et al*. Mutations in *UBQLN2* cause dominant X-linked juvenile and adult-onset ALS and ALS/dementia. *Nature* **477**, 211-215, doi:10.1038/nature10353 (2011).

65. Renton, A. E. *et al*. A Hexanucleotide Repeat Expansion in *C9ORF72* Is the Cause of Chromosome 9p21-Linked ALS-FTD. *Neuron* **72**, 257-268, doi:10.1016/j.neuron.2011.09.010 (2011).

66. DeJesus-Hernandez, M. *et al*. Expanded GGGGCC hexanucleotide repeat in noncoding region of *C9ORF72* causes chromosome 9p-linked FTD and ALS. *Neuron* **7**, 245-256, doi:10.1016/j.neuron.2011.09.011 (2011).

67. Shatunov, A. et al. Chromosome 9p21 in sporadic amyotrophic lateral sclerosis in the UK and seven other countries: a genome-wide association study. *Lancet Neurol* **9**, 986-994, doi:10.1016/S1474-4422(10)70197-6 (2010).

68. Ince, P. G. & Codd, G. A. Return of the cycad hypothesis - does the amyotrophic lateral sclerosis/parkinsonism dementia complex (ALS/PDC) of Guam have new implications for global health? *Neuropathol Appl Neurobiol* **31**, 345-353 (2005).

69. Shaw, P. J. & Eggett, C. J. Molecular factors underlying the selective vulnerability of motor neurons to neurodegeneration in amyotrophic lateral sclerosis. *J Neurol* **247**, I17-I27 (2000).

70. Reyes, N., Ginter, C. & Boudker, O. Transport mechanism of a bacterial homologue of glutamate transporters. *Nature* **462**, 880-885, doi:10.1038/nature08616 (2009).

71. Maragakis, N. J. & Rothstein, J. D. Glutamate transporters: animal models to neurologic disease. *Neurobiol Dis* **15**, 461-473, doi:10.1016/j.nbd.2003.12.007 (2004).

72. Tzingounis, A. V. & Wadiche, J. I. Glutamate transporters: confining runaway excitation by shaping synaptic transmission. *Nat Rev Neurosci* **8**, 935-947, doi:10.1038/nrn2274 (2007).

73. Huang, Y. H., Sinha, S. R., Tanaka, K., Rothstein, J. D. & Bergles, D. E. Astrocyte Glutamate Transporters Regulate Metabotropic Glutamate Receptor-Mediated Excitation of Hippocampal Interneurons. *J Neurosci* **24**, 4551-4559, doi:10.1523/JNEUROSCI.5217-03.2004 (2004).

74. Cohen-Kashi-Malina, K., Cooper, I. & Teichberg, V. I. Mechanisms of glutamate efflux at the blood-brain barrier: involvement of glial cells. *J Cereb Blood Flow Metab* **32**, 177-189, doi:10.1038/jcbfm.2011.121 (2012).

75. von Lewinski, F. & Keller, B. U. Ca^{2+}, mitochondria and selective motoneuron vulnerability: implications for ALS. *Trends Neurosci* **28**, 494-500, doi:10.1016/j.tins.2005.07.001 (2005).

76. Sheng, Z.-H. & Cai, Q. Mitochondrial transport in neurons: impact on synaptic homeostasis and neurodegeneration. *Nat Rev Neurosci* **13**, 77-93, doi:10.1038/nrn3156 (2012).

77. Rugarli, E. I. & Langer, T. Mitochondrial quality control: a matter of life and death for neurons. *EMBO* **31**, 1336-1349, doi:10.1038/emboj.2012.38; (2012).

78. Sathasivam, S., Ince, P. G. & Shaw, P. J. Apoptosis in amyotrophic lateral sclerosis: a review of the evidence. *Neuropathol Appl Neurobiol* **27**, 257-274 (2001).

79. Menzies, F. M., Ince, P. G. & Shaw, P. J. Mitochondrial involvement in amyotrophic lateral sclerosis. *Neurochem Int* **40**, 543-551 (2002).

80. Apel, K. & Hirt, H. Reactive Oxygen Species: Metabolism, Oxidative Stress, and Signal Transduction. *Annu Rev Plant Biol* **55**, 373-399, doi:10.1146/annurev.arplant.55.031903.141701 (2004).

81. Droege, W. Free Radicals in the Physiological Control of Cell Function. *Physiol Rev* **82**, 47-95, doi:10.1152/physrev.00018.2001. (2002).

82. Parge, H. E., Hallewell, R. A. & Tainer, J. A. Atomic structures of wild-type and thermostable mutant recombinant human Cu,Zn superoxide dismutase. *PNAS* **89**, 6109-6113 (1992).

83. Xu, R. *et al*. Linking hypoxic and oxidative insults to cell death mechanisms in models of ALS. *Brain Res* **1372**, 133-144 (2011).

84. Chio, A., Benzi, G., Dossena, M., Mutani, R. & Mora, G. Severely increased risk of amyotrophic lateral sclerosis among Italian professional football players. *Brain* **128**, 472-476 (2005).

85. Wolf, J. A., Stys, P. K., Lusardi, T., Meaney, D. & Smith, D. H. Traumatic Axonal Injury Induces Calcium Influx Modulated by Tetrodotoxin-Sensitive Sodium Channels. *J Neurosci* **21**, 1923-1930 (2001).

86. Shaw, P. J. Toxicity of CSF in motor neurone disease: a potential route to neuroprotection. *Brain* **125**, 693-694 (2002).

87. Mitchell, J. D., Jackson, M. J. & Pentland, B. Indices of free radical activity in the cerebrospinal fluid in motor neurone disease. *J Neurol Neurosurg Psychiatry 50*, 919-922 (1987).

88. Sturtz, L. A., Diekert, K., Jensen, L. T., Lill, R. & Culotta, V. C. A Fraction of Yeast Cu,Zn-Superoxide Dismutase and its Metallochaperone, CCS, Localize to the Intermembrane Space of Mitochondria: A Physiological Role for SOD1 in Guarding Against Mitochondrial Oxidative Damage. *J Bio Chem* **276**, 38084-38089 (2001).

89. Tomkins, J., Banner, S. J., McDermott, C. J. & Shaw, P. J. Mutation screening of manganese superoxide dismutase in amyotrophic lateral sclerosis. *NeuroReport* **12**, 2319-2322 (2001).

90. Van Landeghem, G. F., Tabatabaie, P., Beckman, G., Beckman, L. & Andersen, P. M. Manganese-containing superoxide dismutase signal sequence polymorphism associated with sporadic motor neuron disease. *Eur J Neurol* 6, 639-644, doi:10.1046/j.1468-1331.1999.660639.x (1999).

91. Kirby (nee Tomkins), J., Menzies, F. M., Cookson,

M. R., Bushby, K. & Shaw, P. J. Differential gene expression in a cell culture model of SOD1 related familial motor neurone disease. *Hum Mol Genet* **11**, 2061-2075, doi:10.1093/hmg/11.17.2061 (2002).

92. Deng, H.-X. *et al*. Amyotrophic Lateral Sclerosis and Structural Defects in Cu,Zn Superoxide Dismutase. *Science* **261**, 1047-1051 (1993).

93. Cleveland, D. W. & Rothstein, J. D. From Charcot to Lou Gehring: Deciphering Selective Motor Neuron Death in ALS. *Nat Rev Neurosci* **2**, 806-819 (2001).

94. Arai, K. et al. Glycation and Inactivation of Human Cu-Zn-Superoxide Dismutase: Identification of the *in vitro* glycated sites. *J Bio Chem* **262**, 16969-16972 (1987).

95. Luiking, Y. C., Engelen, M. P. K. J. & Deutz, N. E. P. Regulation of nitric oxide production in health and disease. *Curr Opin Clin Nutr Metab Care* **13**, 97-104, doi:10.1097/MCO.0b013e328332f99d (2010).

96. Cookson, M. R., Manning, P. M., McNeil, C. J., Figlewicz, D. A. & Shaw, P. J. Superoxide-induced nitric oxide release from cultured glial cells. *Brain Res* **911**, 203-210 (2001).

97. Anneser, J. M. H., Cookson, M. R., Ince, P. G., Shaw, P. J. & Borasio, G. D. Glial cells of the spinal cord and subcortical white matter up-regulate neuronal nitric oxide synthase in sporadic amyotrophic lateral sclerosis. *Exp Neurol* **171**, 418-421, doi:10.1006/exnr.2001.775 (2001).

98. Beckman, J. S. & Koppenol, W. H. Nitric oxide, superoxide, and peroxynitrite the good, the bad and the ugly. *Am J Physiol* **271**, c1424-c1437 (1996).

99. Halliwell, B., Zhao, K. & Whiteman, M. Nitric oxide and peroxynitrite. The ugly, the uglier and the not so good: A personal view of recent controversies. *Free Radic Res* **31**, 651-669 (1999).

100. Burney, S., Caulfield, J. L., Niles, J. C., Wishnok, J. S. & Tannenbaum, S. R. The chemistry of DNA damage from nitric oxide and peroxynitrite. *Mutat Res* **424**, 37-49 (1999).

101. Radi, R., Beckman, J. S., Bush, K. M. & Freeman, B. A. Peroxynitrite-induced membrane lipid peroxidation: The cytotoxic potential of superoxide and nitric oxide. *Arch Biochem Biophys* **288**, 481-487 (1991).

102. Allen, S. *et al*. Analysis of the cytosolic proteome in a cell culture model of familial amyotrophic lateral sclerosis reveals alterations to the proteasome, anti-oxidant defences and nitric oxide synthetic pathways. *J Bio Chem* **278**, 6371-6383, doi:10.1074/jbc.M209915200 (2003).

103. Sies, H. & Arteel, G. E. Interaction of peroxynitrite with selenoproteins and glutathione peroxidase mimics. *Free Radic Bio Med* **28**, 1451-1455 (2000).

104. Padmaja, S., Squadrito, G. L. & Pryor, W. A. Inactivation of Glutathione Peroxidase by Peroxynitrite. *Arch Biochem Biophy* **349**, 1-6 (1998).

105. Kirby, J. *et al*. Mutant *SOD1* alters the motor neuronal transcriptome: implications for familial ALS. *Brain* **128**, 1686-1706 (2005).

106. Shaw, P. J. Molecular and cellular pathways of neurodegeneration in motor neurone disease (MND). *J Neurol Neurosurg Psychiatry* **76**, 1046-1057 (2005).

107. Hsu, S.-H. *et al*. Ubiquitin carboxyl-terminal hydrolase L1 (UCHL1) regulates the level of SMN expression through ubiquitination in primary spinal muscular atrophy fibroblasts. *Clin Chim Acta* **411**, 1920-1928 (2010).

108. Menzies, F. M. *et al*. Mitochondrial dysfunction in a cell culture model of familial amyotrophic lateral sclerosis. *Brain* **125**, 1522-1533 (2002).

109. Geiger, B., Spatz, J. P. & Bershadsky, A. D. Environmental sensing through focal adhesions. *Nat Rev: Mol Cell Bio* **10**, 21-33 (2009).

110. Cooper, J. A. The Role of Actin Polymerization in Cell Motility. *Annu Rev Physiol* **53**, 585-605 (1991).

111. Dillon, C. & Goda, Y. The Actin Cytoskeleton: Integrating Form and Function at the Synapse. *Annu Rev Neurosci* **28**, 25-55 (2005).

112. Kreft, M., Potokar, M., Stenovec, M., Pangrsic, T. & Zorec, R. Regulated Exocytosis and Vesicle Trafficking in Astrocytes. *Mechan Exocyt: Ann NY Acad Sci* 1152, 30-42, doi:10.1111/j.1749-6632.2008.04005.x (2009).

113. Janmey, P. A. Phosphoinositides and Calcium as Regulators of Cellular Actin Assembly and Disassembly. *Annu Rev Physiol* **56**, 169-191 (1994).

114. Chow, C. Y. *et al*. Deleterious variants of *FIG4*, a phosphoinositide phosphatase, in patients with ALS. *Am J Hum Genet* **84**, 85-88, doi:10.1016/j.ajhg.2008.12.010 (2009).

115. Arendt, K. L. *et al*. PIP_3 controls synaptic function by maintaining AMPA receptor clustering at the postsynaptic membrane. *Nat Neurosci* **13**, 36-44, doi:10.1038/nn.2462 (2010).

116. Al-Chalabi, A. Deletions of the heavy neurofilament subunit tail in amyotrophic lateral sclerosis. *Hum Mol Genet* **8**, 157-164, doi:10.1093/hmg/8.2.157 (1999).

117. Tsang, Y. M., Chiong, F., Kuznetsov, D., Kasarskis, E. & Geula, C. Motor neurons are rich in non-phosphorylated neurofilaments: cross-species comparison and alternations in ALS. *Brain Res* **861**, 45-58 (2000).

118. Menzies, F. M. et al. Selective loss of neurofilament expression in Cu/Zn superoxide dismutase (SOD1) linked amyotrophic lateral sclerosis. *J Neurochem* **82**, 1118-1128 (2002).

119. Wolozin, B., Gabel, C., Ferree, A., Guillily, M. & Ebata, A. Watching Worms Whither: Modeling Neurodegeneration in C. elegans. *Prog Mol Biol Transl Sci* **100**, 499-514, doi:10.1016/B978-0-12-384878-9.00015-7 (2011).

120. De Vos, K. J. *et al*. Familial amyotrophic lateral sclerosis-linked SOD1 mutants perturb fast axonal transport to reduce axonal mitochondria content. *Hum Mol Genet* **16**, 2720-2728, doi:10.1093/hmg/ddm226 (2007).

121. Kieran, D. *et al*. A mutation in dynein rescues axonal transport defects and extends the life span of ALS mice. *J Cell Biol* **169**, 561-567, doi:10.1083/jcb.200501085 (2005).

122. Burghes, A. H. M. & Beattie, C. E. Spinal muscular atrophy: why do low levels of survival motor neuron protein make motor neurons sick? *Nat Rev Neurosci*

10, 597-609, doi:10.1038/nrn2670 (2009).

123. Corcia, P. *et al*. Abnormal SMN1 gene copy number is a susceptibility factor for amyotrophic lateral sclerosis. *Ann Neurol* **51**, 243-246, doi:10.1002/ana.10104 (2002).

124. Blair, I. P. *FUS* mutations in amyotrophic lateral sclerosis: clinical, pathological, neurophysiological and genetic analysis. *J Neurol Neurosurg Psychiatry* **81**, 639-645, doi:10.1136/jnnp.2009.194399 (2010).

125. Taylor, A. R. *et al*. Astrocyte and Muscle-Derived Secreted Factors Differentially Regulate Motoneuron Survival. *J Neurosci* **27**, 634-644, doi:10.1523/JNEUROSCI.4947-06.2007 (2007).

126. Sofroniew, M. V. & Vinters, H. V. Astrocytes: biology and pathology. *Acta Neuropathol* **119**, 7-35, doi:10.1007/s00401-009-0619-8 (2010).

127. Maragakis, N. J. & Rothstein, J. D. Mechanisms of Disease: astrocytes in neurodegenerative disease. *Nat Clin Pract Neurol* **2**, 679-689, doi:10.1038/ncpneuro0355 (2006).

128. Haidet-Phillips, A. M. *et al*. Astrocytes from familial and sporadic ALS patients are toxic to motor neurons. *Nat Biotech* **29**, 824-830, doi:10.1038/nbt1957 (2011).

129. Lepore, A. C. *et al*. Focal transplantation-based astrocyte replacement is neuroprotective in a model of motor neuron disease. *Nat Neurosci* **11**, 1294-1301, doi:10.1038/nn.2210 (2008).

130. Williams, R. E. *et al*. Cultured glial cells are resistant to the effects of ALS/MND associated SOD1 mutations. *Neurosci Lett* **302**, 146-150 (2001).

131. Faijerson, J. *et al*. Reactive Astrogliosis Induces Astrocytic Differentiation of Adult Neural Stem/Progentor Cells *In Vitro*. *J Neurosci Res* **84**, 1415-1424 (2006).

132. Diaz-Amarilla, P. *et al*. Phenotypically aberrant astrocytes that promote motoneuron damage in a model of inherited amyotrophic lateral sclerosis. *PNAS* **108**, 18126-18131, doi:10.1073/pnas.1110689108 (2011).

133. Collinson, J. M., Marshall, D., Gillespie, C. S. & Brophy, P. J. Transient Expression of Neurofascin by Oligodendrocytes at the Onset of Myelinogenesis: Implications for Mechanisms of Axon-Glial Interaction. *Glia* **23**, 11-23 (1998).

134. Taveggia, C. *et al*. Type III Neuregulin-1 Promotes Oligodendrocyte Myelination. *Glia* **56**, 284-293, doi:10.1002/glia.20612 (2008).

135. Arai, K. & Lo, E. H. Astrocytes Protect Oligodendrocyte Precursor Cells via MEK/ERK and PI3K/Akt Signaling. *J Neurosci Res* **88**, 758-763, doi:10.1002/jnr.22256 (2010).

136. McGeer, P. L. & McGeer, E. G. Inflammatory processes in amyotrophic lateral sclerosis. *Muscle and Nerve* **26**, 459-470 (2002).

137. Sargsyan, S. A., Monk, P. N. & Shaw, P. J. Microglia as potential contributors to motor neuron injury in amyotrophic lateral sclerosis. *Glia* **51**, 241-253 (2005).

138. Doe, C. Q. Neural stem cells: balancing self-renewal with differentiation. *Development* **135**, 1575-1587 (2008).

139. Cashman, N. R. *et al*. Neuroblastoma x Spinal Cord (NSC) Hybrid Cell Lines Resemble Developing Motor Neurons. *Dev Dynam* **194**, 209-221 (1992).

140. Eggett, C. J. *et al*. Development and characterisation of a glutamate sensitive motor neurone cell line. *J Neurochem* **74**, 1895-1902 (2000).

141. Durham, H. D. Evaluation of the spinal cord neuron X neuroblastoma hybrid cell line NSC-34 as a model for neurotoxicity testing. *Neurotoxicol* **14**, 387-395 (1993).

142. Gomez, N., Chen, S. & Schmidt, C. E. Polarization of hippocampal neurons with competitive surface stimuli: contact guidance cues are preferred over chemical ligands. *J R Soc Interface* **4**, 223-233, doi:10.1098/rsif.2006.0171 (2007).

143. Grumbles, R. M., Sesodia, S., Wood, P. M. & Thomas, C. K. Neurotrophic Factors Improve Motoneuron Survival and Function of Muscle Reinnervated by Embryonic Neurons. *J Neuropathol Exp Neurol* **68**, 736-746, doi:10.1097/NEN.0b013e3181a9360f (2009).

144. Nona, S. N., Thomlinson, A. M., Bartlett, C. A. & Scholes, J. Schwann cells in the regenerating fish optic nerve: Evidence that CNS axons, not the glia, determine when myelin formation begins. *J Neurocytol* **29**, 285-300 (2000).

145. Gingras, M., Beaulieu, M.-M., Gagnon, V., Durham, H. D. & Berthod, F. *In Vitro* Study of Axonal Migration and Myelination of Motor Neurons in a Three-Dimensional Tissue Engineered Model. *Glia* **56**, 354-364, doi:10.1002/glia.20617 (2008).

146. Barbeito, L. H. *et al*. A role for astrocytes in motor neuron loss in amyotrophic lateral sclerosis. *Brain Res Rev* **47**, 263- 274, doi:10.1016/j.brainresrev.2004.05.003 (2004).

147. Nagai, M. *et al*. Astrocytes expressing ALS-linked mutated SOD1 release factors selectively toxic to motor neurons. *Nat Neurosci* **10**, 615-622, doi:10.1038/nn1876 (2007).

148. Das, M. *et al*. Embryonic motoneuron-skeletal muscle co-culture in a define system. Neuroscience 146, 481-488 (2007).

149. 149 Das, M., Rumsey, J. W., Bhargava, N., Stancescu, M. & Hickman, J. J. A defined long-term in vitro tissue engineered model of neuromuscular junctions. Biomaterials 31, 4880-4888 (2010).

150. 150 Elliott, J. L. Experimental Models of Amyotrophic Lateral Sclerosis. Neurobiol Disease 6, 310-320 (1999).

151. Ding, J. B., Takasaki, K. T. & Sabatini, B. L. Supraresolution Imaging in Brain Slices using Stimulated-Emission Depletion Two-Photon Laser Scanning Microscopy. *Neuron* **63**, 429-437 (2009)

152. Kasischke, K. A., Vishwasrao, H. D., Fisher, P. J., Zipfel, W. R. & Webb, W. W. Neural Activity Triggers Neuronal Oxidative Metabolism Followed by Astrocytic Glycolysis. *Science* **305**, 99-103, doi:10.1126/science.1096485 (2004).

153. Rothstein, J. D., Jin, L., Dykes-Hoberg, M. & Kuncl, R. W. Chronic inhibition of glutamate uptake produces

a model of slow neurotoxicity. *PNAS* **90**, 6591-6595 (1993).

154. Rodriguez-Ithurralde, D., Olivera, S., Migues, V., Vincent, O. & Salazar, R. Glutamate-receptor elicited acetylcholinesterase release in mouse spinal cord slice: a model of early excitotoxic injury. *J Neurol Sci* **129**, 104-106 (1995).

155. Yin, H. Z. & Weiss, J. H. Marked synergism between mutant SOD1 and glutamate transport inhibition in the induction of motor neuronal degeneration in spinal cord slice cultures. *Brain Res* **1448**, 153-162, doi:10.1016/j.brainres.2012.02.005 (2012).

156. Lu, Y., Inokuchi, H., Tanaka, E., Li, J.-S. & Higashi, H. A spinal cord slice preparation for analyzing synaptic responses to stimulation of pelvic and pudendal nerves in mature rats. *J Neurosci Methods* **100**, 71-78 (2000).

157. Jeong, D.-K., Taghavi, C. E., Song, K.-J., Lee, K.-B. & Kang, H.-W. Organotypic Human Spinal Cord Slice Culture as an Alternative to Direct Transplantation of Human Bone Marrow Precursor Cells for Treating Spinal Cord Injury. *World Neurosurg* **75**, 533-539, doi:10.1016/j.wneu.2010.10.042 (2011).

158. Jucker, M. The benefits and limitations of animal models for translational research in neurodegenerative diseases. *Nat Med* **16**, 1210-1214, doi:10.1038/nm.2224 (2010).

159. Dimitriadi, M. & Hart, A. C. Neurodegenerative disorders: Insights from the nematode Caenorhabditis elegans. *Neurobiol Dis* **40**, 4-11, doi:10.1016/j.nbd.2010.05.012 (2010).

160. Lessing, D. & Bonini, N. M. Maintaing the brain: insight into human neurodegeneration from Drosophila melanogaster mutants. *Nat Rev Genet* **10**, 359-370, doi:10.1038/nrg2563 (2009).

161. Vaccaro, A. *et al*. TDP-1/TDP-43 Regulates Stress Signalling and Age-Dependent Proteotoxicity in Caenorhabditis elegans. *PLoS Genet* **8**, e1002806, doi:10.1371/journal.pgen.1002806 (2012).

162. Ramesh, T. *et al*. A genetic model of amyotrophic lateral sclerosis in zebrafish displays phenotypic hallmarks of motoneuron disease. *Dis Model Mech* **3**, 652-662, doi:10.1242/dmm.005538 (2010).

163. Uchida, A. *et al*. Non-human primate model of amyotrophic lateral sclerosis with cytoplasmic mislocalization of TDP-43. *Brain* **135**, 833-846, doi:10.1093/brain/awr348 (2012).

164. Rothstein, J. D. Of Mice and Men: Reconciling Preclinical ALS Mouse Studies and Human Clinical Trials. *Ann Neurol* **53**, 423-426, doi:10.1002/ana.10561 (2003).

165. Raoul, C. *et al*. Motoneuron Death Triggered by a Specific Pathway Downstream of Fas: Potentiation by ALS-linked SOD1 Mutations. *Neuron* **35**, 1067-1083 (2002).

166. Thonhoff, J. R., Ojeda, L. D. & Wu, P. Stem Cell-Derived Motor Neurons: Applications and Challenges in Amyotrophic Lateral Sclerosis. *Curr Stem Cell Res Ther* **4**, 178-199 (2009).

167. Rubin, L. L. & Haston, K. M. Stem cell biology and drug discovery. *BMC Biol* **9**, 42 (2011).

168. Christou, Y. A. *Generation of motor neurons from embryonic stem cells: application in studies of the motor neuron disease mechanism* PhD thesis, University of Sheffield, (2009).

169. Jordan, P. M. *et al*. Generation of spinal motor neurons from fetal brain-derived neural stem cells: role of basic fibroblast growth factor. *J Neurosci Res* **87**, 318-332, doi:10.1002/jnr.21856 (2009).

170. Erceg, S. *et al*. Differentiation of Human Embryonic Stem Cells to Regional Specific Neural Precursors in Chemically Defined Medium Conditions. *PLoS ONE* **3**, e2122, doi:10.1371/journal.pone.0002122 (2008).

171. Soundararajan, P., MIles, G. B., Rubin, L. L., Brownstone, R. M. & Rafuse, V. F. Motoneurons Derived from Embryonic Stem Cells Express Transcription Factors and Develop Phenotypes Characteristic of Medial Motor Column Neurons. *J Neurosci* **26**, 3256-3268 (2006).

172. Kaewkhaw, R., Scutt, A. M. & Haycock, J. W. Anatomical Site Influences the Differentiation of Adipose-Derived Stem Cells for Schwann-Cell Phenotype and Function. *Glia* **59**, 734-749, doi:10.1002/glia.21145 (2011).

173. Greco, S. J., Zhou, C., Ye, J.-H. & Rameshwar, P. A method to generate human mesenchymal stem cell-derived neurons which express and are excited by multiple neurotransmitters *Biol Proc Online* **10**, 90-101, doi:10.1251/bpo147 (2008).

174. Dimos, J. T. *et al*. Induced pluripotent stem cells generated from patients with ALS can be differentiated into motor neurons. *Science* **321**, 1218-1221 (2008).

175. Mitne-Neto, M. *et al*. Downregulation of *VAPB* expression in motor neurons derived from induced pluripotent stem cells of ALS8 patients. *Hum Mol Genet*, doi:10.1093/hmg/ddr284 (2011).

176. Caiazzo, M. *et al*. Direct generation of functional dopaminergic neurons from mouse and human fibroblasts. *Nature* **476**, 224-227, doi:10.1038/nature10284 (2011).

177. Schmidt, C. E. & Leach, J. B. Neural Tissue Engineering: Strategies for Repair and Regeneration. *Annu Rev Biomed Eng* **5**, 293-347 (2003).

178. Evans, G. R. D. Peripheral Nerve Injury: A Review and Approach to Tissue Engineered Constructs. *Anat Rec* **263**, 396-404, doi:10.1002/ar.1120 (2001).

179. Jha, B. S. *et al*. Two pole air gap electrospinning: Fabrication of highly aligned, three-dimensional scaffolds for nerve recontruction. *Acta Biomat* **7**, 203-215, doi:10.1016/j.actbio.2010.08.004 (2011).

180. Evans, G. R. D. *et al*. Bioactive poly(L-lactic acid) conduits seeded with Schwann cells for peripheral nerve regeneration. *Biomaterials* **23**, 841-848 (2002).

181. Schnell, E. *et al*. Guidance of glial cell migration and axonal growth on electrospun nanofibers of poly-ε-caprolactone and a collagen/poly-ε-caprolactone blend. *Biomaterials* **28**, 3012-3025, doi:10.1016/j.biomaterials.2007.03.009 (2007).

182. Mori, K. & Sakano, H. How is the Olfactory Map Formed and Interpreted in the Mammalian Brain? *Annu Rev Neurosci* **34**, 467-499, doi:10.1146/annurev-neuro-112210-112917 (2011).

183. Chen, B. K. *et al*. Comparison of polymer scaffolds in rat spinal cord: A step toward quantitative assessment of combinatorial approaches to spinal cord repair. *Biomaterials* **32**, 8077-8086, doi:10.1016/j.biomaterials.2011.07.029 (2011).

184. Williams, D. F. On the mechanisms of biocompatibility. **Biomaterials 29**, 2941-2953 (2008).

185. Baier, R. E. Surface behaviour of biomaterials: The theta surface for biocompatibility. *J Mater Sci: Mater Med* **17**, 1057-1062 (2006).

186. Sell, S. A., McClure, M. J., Garg, K., Wolfe, P. S. & Bowlin, G. L. Electrospinning of collagen/biopolymers for regenerative medicine and cardiovascular tissue engineering. *Adv Drug Deliv Rev* **61**, 1007-1019 (2009).

187. Xu, S. *et al*. Electrospinning of native cellulose from nonvolatile solvent system. Polymer 49, 2911-2917 (2008).

188. Min, B.-M. *et al*. Electrospinning of silk fibroin nanofibres and its effect on the adhesion and spreading of normal human keratinocytes and fibroblasts in vitro. *Biomaterials* **25**, 1289-1297 (2004).

189. Chen, Z.-G., Wei, B., Mo, X.-M. & Cui, F.-Z. Diameter Control of Electrospun Chitosan-Collagen Fibers. *J Polym Sci B* **47**, 1949-1955, doi:10.1002/polb.21793 (2009).

190. Lee, K. Y., Jeong, L., Kang, Y. O., Lee, S. J. & Park, W. H. Electrospinning of polysaccharides for regenerative medicine. *Adv Drug Deliv Rev* **61**, 1020-1032 (2009).

191. Kwon, I. K., Kidoaki, S. & Matsuda, T. Electrospun nano- to microfiber fabrics made of biodegradable copolyesters: structural characteristics, mechanical properties and cell adhesion potential. *Biomaterials* **26**, 3929-3939 (2005).

192. Koh, H. S., Yong, T., Chan, C. K. & Ramakrishna, S. Enhancement of neurite outgrowth using nano-structured scaffold coupled with laminin. *Biomaterials* **29**, 3574-3582 (2008).

193. Deb, S. in *Cellular response to biomaterials* (ed Lucy Di Silvio) Ch. 2, 28-60 (Woodhead Publishing Ltd, 2009).

194. You, Z. & Wang, Y. in *Biomaterials for Tissue Engineering Applications: A Review of the Past and Future Trends* (eds Jason A. Burdick & Robert L. Mauck) Ch. 4, 75-118 (Springer, 2011).

195. Thomas, V. *et al*. Mechano-morphological studies of aligned nanofibrous scaffolds of polycaprolactone fabricated by electrospinning. *J Biomat Sci Polymer Ed* **17**, 969-984, doi:10.1163/156856206778366022 (2006).

196. Williamson, M. R., Adams, E. F. & Coombes, A. G. A. Cell Attachment and Proliferation on Novel Polycaprolactone Fibres having Applications in Soft Tissue Engineering. *Eur Cells Mater* **4**, 62-63 (2002).

197. Feng, J. J. Stretching of a straight electrically charged viscoelastic jet. *J Non-Newtonian Fluid Mech* **116**, 55-70 (2003).

198. Deitzel, J. M., Kleinmeyer, J., Harris, D. & Beck Tan, N. C. The effect of processing variables on the morphology of electrospun nanofibres and textiles. *Polymer* **42**, 261-272 (2001).

199. He, J.-H., Wan, Y.-Q. & Yu, J.-Y. Scaling law in electrospinning: relationship between electric current and solution flow rate. *Polymer* **46**, 2799-2801 (2005).

200. Thompson, C. J., Chase, G. G., Yarin, A. L. & Reneker, D. H. Effects of parameters on nanofiber diameter determined from electrospinning model. *Polymer* **48**, 6913-6922 (2007).

201. de la Mora, J. F. The Fluid Dynamics of Taylor Cones. *Annu Rev Fluid Mech* **39**, 217-243, doi:10.1146/annurev.fluid.39.050905.110159 (2007).

202. Uyar, T. & Besenbacher, F. Electrospinning of uniform polystyrene fibers: The effect of solvent conductivity. *Polymer* **49**, 5336-5343 (2008).

203. He, J.-H., Wu, Y. & Zuo, W.-W. Critical length of straight jet in electrospinning. *Polymer* **46**, 12637-12640 (2005).

204. Reneker, D. H., Yarin, A. L., Fong, H. & Koombhongse, S. Bending instability of electrically charged liquid jets of polymer solutions in electrospinning. *J Appl Phys* **87**, 4531-4547 (2000).

205. Yarin, A. L., Koombhongse, S. & Reneker, D. H. Bending instability in electrospinning of nanofibers. *J Appl Phys* **89**, 3018-3026 (2001).

206. Oliveira, M. S. N., Yeh, R. & McKinley, G. H. Iterated stretching, extensional rheology and formation of beads-on-a-string structures in polymer solutions. *J Non-Newtonian Fluid Mech* **137**, 137-148 (2006).

207. Tan, D. H. et al. Meltblown fibers: Influence of viscosity and elasticity on diameter distribution. *J Non-Newtonian Fluid Mech* **165**, 892-900 (2010).

208. David, R. L. A., Wei, M.-H. & Kornfield, J. A. Effects of pairwise, donor-acceptor functional groups on polymer solubility, solution viscosity and mist control. *Polymer* **50**, 6323-6330, doi:10.1016/j.polymer.2009.10.032 (2009).

209. Luo, C. J., Nangrejo, M. & Edirisinghe, M. A novel method of selecting solvents for polymer electrospinning. *Polymer* **51**, 1654-1662 (2010).

210. Lu, C., Chen, P., Li, J. & Zhang, Y. Computer simulation of electrospinning. Part I. Effect of solvent in electrospinning. *Polymer* **47**, 915-921 (2006).

211. Huang, L., Bui, N.-N., Manickam, S. S. & McCutcheon, J. R. Controlling Electrospun Nanofiber Morphology and Mechanical Properties Using Humidity. *J Polym Sci B* **49**, 1734-1744, doi:10.1002/polb.22371 (2011).

212. Pawar, S. D., Murugavel, P. & Lal, D. M. Effect of relative humidity and sea level pressure on electrical conductivity of air over Indian Ocean. *J Geophys Res* **114**, D02205_02201-02208, doi:10.1029/2007JD009716 (2009).

213. Greco, S. J., Zhou, C., Ye, J.-H. & Rameshwar, P. A method to generate human mesenchymal stem cell-derived neurons which express and are excited by multiple neurotransmitters. *Biol Proc Online* **10**, 90-101, doi:10.1251/bpo147 (2008).

214. Jiang, X., Lim, S. H., Mao, H.-Q. & Chew, S. Y.

Current applications and future perspectives of artificial nerve conduits. *Exp Neurol* **223**, 86-101, doi:10.1016/j.expneurol.2009.09.009 (2010).

215. Christopherson, G. T., Song, H. & Mao, H.-Q. The influence of fiber diameter of electrospun substrates on neural stem cell differentiation and proliferation. *Biomaterials* **30**, 556-564, doi:10.1016/j.biomaterials.2008.10.004 (2009).

216. Leach, M. K. *et al*. The Culture of Primary Motor and Sensory Neurons in Defined Media on Electrospun Poly-L-lactide Nanofiber Scaffolds. *J Vis Exp*, e2389, doi:10.3791/2389 (2011).

217. Gertz, C. C. *et al*. Accelerated neuritogenesis and maturation of primary spinal motor neurons in response to nanofibers. *Dev Neurobiol* **70**, 589-603, doi:10.1002/dneu.20792 (2010).

218. Neusch, C., Bahr, M. & Schneider-Gold, C. Glia cells in Amyotrophic lateral sclerosis: New clues to understanding an old disease? *Muscle and Nerve* **35**, 712-714 (2007).

219. Langlois, S. D., Morin, S., Yam, P. T. & Charron, F. Dissection and Culture of Commisural Neurons from Embryonic Spinal Cord. *J Vis Exp* **39**, e1773, doi:10.3791/1773 (2010).

220. Cherney, L. T. Structure of Taylor cone-jets: limit of low flow rates. *J Fluid Mech* **378**, 167-196 (1999).

221. Luedtke, W. D. et al. Nanojets, Electrospray, and Ion Field Evaporation: Molecular Dynamics Simulations and Laboratory Experiments. *J Phys Chem A* **112**, 9628-9649, doi:10.1021/jp804585y (2008).

222. Fernandez de la Mora, J. & Loscertales, I. G. The current emitted by highly conducting Taylor cones. *J Fluid Mech* **260**, 155-184 (1994).

223. Shrimpton, J. S. Dielectric Charged Drop Break-up at Sub-Rayleigh Limit Conditions. *IEEE Trans Dielect Elect Insul* **12**, 573-578, doi:10.1109/TDEI.2005.1453462 (2005).

224. Zeleny, J. The Electrical Discharge from Liquid Points, and A Hydrostatic Method of Measuring the Electric Intensity at Their Surfaces. *Phys Rev* **3**, 69-91 (1914).

225. Yarin, A. L. Strong Flows of Polymeric Liquids Part 1. Rheological Behaviour. *J Non-Newtonian Fluid Mech* **37**, 113-138 (1990).

226. Luo, C. J., Stride, E. & Edirisinghe, M. Mapping the Influence of Solubility and Dielectric Constant on Electrospinning Polycaprolactone Solutions. *Macromolecules* **45**, 4669-4680, doi:10.1021/ma300656u (2012).

227. Wang, P. & Anderko, A. Computation of dielectric constants of solvent mixtures and electrolyte solutions. *Fluid Phase Equilibria* **186**, 103-122 (2001).

228. Theron, S. A., Zussman, E. & Yarin, A. L. Experimental investigation of the governing parameters in the electrospinning of polymer solutions. *Polymer* **45**, 2017-2030 (2004).

229. Gomez, N., Lu, Y., Chen, S. & Schmidt, C. E. Immobilized nerve growth factor and microtopography have distinct effects on polarization versus axon elongation in hippocampal cells in culture. *Biomaterials* **28**, 271-284, doi:10.1016/j.biomaterials.2006.07.043 (2007).

230. Dotti, C. G., Sullivan, C. A. & Banker, G. A. The establishment of polarity by hippocampal neurons in culture. *J Neurosci* **8**, 1454-1468 (1988).

231. Sheetz, M. P., Wayne, D. B. & Pearlman, A. L. Extension of filopodia by motor-dependent actin assembly. *Cell Motil Cytoskel* **22**, 160-169 (1992).

232. Isbister, C. M. & O'Connor, T. P. Filopodial adhesion does not predict growth cone steering events *in vivo*. *J Neurosci* 19, 2589-2600 (1999).

233. Andersen, S. S. L. & Bi, G.-q. Axon formation: a molecular model for the generation of neuronal polarity. *BioEssays* **22**, 172-179 (2000).

234. Raincek, A. M., Britland, S. & McCaig, C. D. Contact guidance of CNS neurites on grooved quartz: influence of groove dimensions, neuronal age and cell type. *J Cell Sci* **110**, 2905-2913 (1997).

235. Esch, T., Lemmon, V. & Banker, G. Local presentation of substrate molecules direct axon specification by cultured hippocampal neurons. *J Neurosci* **19**, 6417-6426 (1999).

236. Sousa-Nunes, R., Yee, L. L. & Gould, A. P. Fat cells reactivate quiescent neuroblasts via TOR and glial Insulin relays in Drosophila. *Nature* **471**, 508-512, doi:10.1038/nature09867 (2011).

237. Corey, J. M. *et al*. The design of electrospun PLLA nanofiber scaffolds compatible with serum-free growth of primary motor and sensory neurons. *Acta Biomater* **4**, 863-875, doi:10.1016/j.actbio.2008.02.020 (2008).

238. Dertinger, S. K. W., Jiang, X., Li, Z., Murthy, V. N. & Whitesides, G. M. Gradients of substrate-bound laminin orient axonal specification of neurons. *PNAS* **99**, 12542-12547, doi:10.1073pnas.192457199 (2002).

239. Cohen, J., Burne, J. F., Winter, J. & Bartlett, P. Retinal ganglion cells lose response to laminin with maturation. *Nature* **322**, 465-467 (1986).

240. Neugebauer, K. M. & Reichardt, L. F. Cell-surface regulation of beta1-integrin activity on developing retinal neurons. *Nature* **350**, 68-71 (1991).

241. Lee, S. *et al*. A culture system to study oligodendrocyte myelination processes using engineered nanofibers. *Nat Methods* **9**, 917-922, doi:10.1038/nmeth.2105 (2012).

242. Tan, S. H., Inai, R., Kotaki, M. & Ramakrishna, S. Systematic parameter study for ultra-fine fiber fabrication via electrospinning process. *Polymer* **46**, 6128-6134, doi:10.1016/j.polymer.2005.05.068 (2005).

243. Hill, N. E., Vaughan, W. E., Price, A. H. & Davies, M. *Dielectric Properties and Molecular Behaviour.* (Van Nostrand Reinhold Company, 1969).

244. Tuszynski, J. A., Brown, J. A. & Hawrylak, P. Dielectric polarization, electrical conduction, information processing and quantum computation in microtubules. Are they plausible? *Phil Trans R Soc Lond A* **356**, 1897-1926, doi:10.1098/rsta.1998.0255 (1998).

245. Yarin, A. L., Koombhongse, S. & Reneker, D. H. Taylor cone and jetting from liquid droplets in electrospinning of nanofibres. *J Appl Phys* **90**, 4836-4846, doi:10.1063/1.1408260 (2001).

246. Grimm, R. L. & Beauchamp, J. L. Evaporation and Discharge Dynamics of Highly Charged Multicomponent Droplets Generated by Electrospray Ionization. *J Phys Chem A* **114**, 1411-1419, doi:10.1021/jp907162w (2010).

247. Jun, Z., Hou, H., Schaper, A., Wendorff, J. H. & Greiner, A. Poly-L-lactide nanofibers by electrospinning - Influence of solution viscosity and electrical conductivity on fiber diameter and fiber morphology. *e-Polymer* 9 (2003).

248. Queimada, A. J., Marrucho, I. M., Stenby, E. H. & Coutinho, J. A. P. Generalized relation between surface tension and viscosity: a study on pure and mixed n-alkanes. *Fluid Phase Equilibria* **222-223**, 161-168, doi:10.1016/j.fluid.2004.06.016 (2004).

249. Ibrehem, A. S. & Al-Salim, H. S. Generalized relation between surface tension and viscosity for some mixed organic compounds. *JPGE* **2**, 22-24 (2011).

Appendix

A. Inter-depedent Log-Normal ANOVA of Extended NSC-34 Neurite lengths

```
 Tukey multiple comparisons of means
    95% family-wise confidence level

Fit: aov(formula = log(length) ~ Scaffold * passage)

$Scaffold
                      diff          lwr           upr        p adj
fine-cont       -0.09167079 -0.16864737 -0.0146942062 0.0119217
mid-cont        -0.07933750 -0.16770828  0.0090332860 0.0964696
thick-cont      -0.18894276 -0.28370223 -0.0941832835 0.0000019
mid-fine         0.01233329 -0.08138269  0.1060492799 0.9866775
thick-fine      -0.09727197 -0.19703493  0.0024909956 0.0591339
thick-mid       -0.10960526 -0.21840163 -0.0008088934 0.0475208

$passage
                      diff          lwr          upr        p adj
p14-p13          0.17932308  0.11127558  0.247370586 0.0000000
p16-p13          0.07648619 -0.02915271  0.182125081 0.2452242
p17-p13         -0.09937084 -0.25140003  0.052658352 0.3343980
p16-p14         -0.10283689 -0.21124540  0.005571607 0.0702662
p17-p14         -0.27869392 -0.43266048 -0.124727358 0.0000202
p17-p16         -0.17585703 -0.34973864 -0.001975414 0.0462540

$`Scaffold:passage`
                            diff          lwr          upr        p adj
fine:p13-cont:p13     -0.1997748190  0.349116731 -0.050432907 0.0005203
mid:p13-cont:p13      -0.2281301479 -0.388334654 -0.067925641 0.0001257
thick:p13-cont:p13    -0.2124440459 -0.411624735 -0.013263357 0.0233207
cont:p14-cont:p13     -0.0169070142 -0.162513008  0.128698979 1.0000000
fine:p14-cont:p13      0.0552965652 -0.095296119  0.205889250 0.9971393
mid:p14-cont:p13       0.2610662004  0.046917951  0.475214450 0.0031251
thick:p14-cont:p13     0.0110065157 -0.206403961  0.228416993 1.0000000
cont:p16-cont:p13      0.0631960836 -0.129444153  0.255836320 0.9992041
fine:p16-cont:p13     -0.5821788483 -1.236194783  0.071837086 0.1482575
mid:p16-cont:p13       0.0923221550 -0.270277905  0.454922215 0.9999654
thick:p16-cont:p13    -0.3174237410 -0.595949974 -0.038897508 0.0093008
cont:p17-cont:p13     NA            NA           NA           NA
fine:p17-cont:p13     -0.2310000460 -0.630537303  0.168537211 0.8352503
mid:p17-cont:p13      -0.2290417185 -0.598883112  0.140799675 0.7500957
thick:p17-cont:p13    -0.3790995675 -0.682350896 -0.075848239 0.0019917
mid:p13-fine:p13      -0.0283553289 -0.198614226  0.141903568 0.9999999
thick:p13-fine:p13    -0.0126692269 -0.220022922  0.194684468 1.0000000
cont:p14-fine:p13      0.1828678048  0.026267315  0.339468295 0.0063924
fine:p14-fine:p13      0.2550713842  0.093823858  0.416318910 0.0000074
mid:p14-fine:p13       0.4608410194  0.239070686  0.682611353 0.0000000
thick:p14-fine:p13     0.2107813347 -0.014140704  0.435703374 0.0957275
cont:p16-fine:p13      0.2629709026  0.061891643  0.464050163 0.0008323
fine:p16-fine:p13     -0.3824040293 -1.038955208  0.274147150 0.8272388
mid:p16-fine:p13       0.2920969740 -0.075056144  0.659250092 0.3129494
thick:p16-fine:p13    -0.1176489220 -0.402077244  0.166779400 0.9899972
cont:p17-fine:p13     NA            NA           NA           NA
fine:p17-fine:p13     -0.0312252270 -0.434899140  0.372448686 1.0000000
mid:p17-fine:p13      -0.0292668995 -0.403573277  0.345039478 1.0000000
thick:p17-fine:p13    -0.1793247485 -0.488005776  0.129356279 0.8300831
thick:p13-mid:p13      0.0156861019 -0.199623053  0.230995256 1.0000000
cont:p14-mid:p13       0.2112231336  0.044231545  0.378214722 0.0016001
fine:p14-mid:p13       0.2834267131  0.112069654  0.454783772 0.0000018
mid:p14-mid:p13        0.4891963482  0.259970351  0.718422346 0.0000000
thick:p14-mid:p13      0.2391366636  0.006860103  0.471413224 0.0359787
cont:p16-mid:p13       0.2913262314  0.082052855  0.500599607 0.0002149
fine:p16-mid:p13      -0.3540487004 -1.013155617  0.305058216 0.9010956
mid:p16-mid:p13        0.3204523029 -0.051251731  0.692156337 0.1885943
thick:p16-mid:p13     -0.0892935931 -0.379572678  0.200985492 0.9996298
cont:p17-mid:p13      NA            NA           NA           NA
fine:p17-mid:p13      -0.0028698981 -0.410687388  0.404947592 1.0000000
mid:p17-mid:p13       -0.0009115706 -0.379682928  0.377859787 1.0000000
thick:p17-mid:p13     -0.1509694196 -0.465049750  0.163110910 0.9593364
cont:p14-thick:p13     0.1955370317 -0.009142360  0.400216424 0.0799024
fine:p14-thick:p13     0.2677406112  0.059484268  0.475996955 0.0011701
mid:p14-thick:p13      0.4735102463  0.215533463  0.731487030 0.0000000
thick:p14-thick:p13    0.2234505616 -0.037240565  0.484141689 0.1964876
cont:p16-thick:p13     0.2756401295  0.035217982  0.516062277 0.0084993
fine:p16-thick:p13    -0.3697348024 -1.039383509  0.299913905 0.8794122
mid:p16-thick:p13      0.3047662010 -0.085325265  0.694857667 0.3446801
thick:p16-thick:p13   -0.1049796950 -0.418459216  0.208499826 0.9989881
cont:p17-thick:p13    NA            NA           NA           NA
fine:p17-thick:p13    -0.0185560000 -0.443200049  0.406088049 1.0000000
mid:p17-thick:p13     -0.0165976725 -0.413429128  0.380233783 1.0000000
```

thick:p17-thick:p13	-0.1666555215	-0.502295085	0.168984042	0.9465371
fine:p14-cont:p14	0.0722035795	-0.085590157	0.229997316	0.9737001
mid:p14-cont:p14	0.2779732146	0.058701284	0.497245145	0.0015336
thick:p14-cont:p14	0.0279135299	-0.194545505	0.250372565	1.0000000
cont:p16-cont:p14	0.0801030978	-0.118217268	0.278423463	0.9921393
fine:p16-cont:p14	-0.5652718341	-1.220983317	0.090439649	0.1886613
mid:p16-cont:p14	0.1092291693	-0.256420267	0.474878606	0.9997408
thick:p16-cont:p14	-0.3005167267	-0.583001362	-0.018032092	0.0241036
cont:p17-cont:p14	NA	NA	NA	NA
fine:p17-cont:p14	-0.2140930317	-0.616399789	0.188213725	0.9077335
mid:p17-cont:p14	-0.2121347042	-0.584966252	0.160696843	0.8517521
thick:p17-cont:p14	-0.3621925532	-0.669083536	-0.055301571	0.0053920
mid:p14-fine:p14	0.2057696351	-0.016844898	0.428384169	0.1082966
thick:p14-fine:p14	-0.0442900495	-0.270044503	0.181464404	0.9999989
cont:p16-fine:p14	0.0078995183	-0.194110428	0.209909465	1.0000000
fine:p16-fine:p14	-0.6374754136	-1.294312228	0.019361401	0.0684005
mid:p16-fine:p14	0.0370255898	-0.330638063	0.404689243	1.0000000
thick:p16-fine:p14	-0.3727203062	-0.657807346	-0.087633267	0.0008375
cont:p17-fine:p14	NA	NA	NA	NA
fine:p17-fine:p14	-0.2862966112	-0.690434927	0.117841704	0.5255860
mid:p17-fine:p14	-0.2843382837	-0.659145453	0.090468885	0.3979610
thick:p17-fine:p14	-0.4343961327	-0.743684229	-0.125108037	0.0001747
thick:p14-mid:p14	-0.2500596847	-0.522358031	0.022238662	0.1146243
cont:p16-mid:p14	-0.1978701168	-0.450831250	0.055091016	0.3425306
fine:p16-mid:p14	-0.8432450487	-1.517497165	-0.168992932	0.0019765
mid:p16-mid:p14	-0.1687440453	-0.566686098	0.229198008	0.9872006
thick:p16-mid:p14	-0.5784899414	-0.901686377	-0.255293505	0.0000001
cont:p17-mid:p14	NA	NA	NA	NA
fine:p17-mid:p14	-0.4920662464	-0.923933233	-0.060199260	0.0093328
mid:p17-mid:p14	-0.4901079188	-0.894659189	-0.085556649	0.0034828
thick:p17-mid:p14	-0.6401657678	-0.984898189	-0.295433346	0.0000000
cont:p16-thick:p14	0.0521895679	-0.203539151	0.307918286	0.9999982
fine:p16-thick:p14	-0.5931853640	-1.268480677	0.082109949	0.1643010
mid:p16-thick:p14	0.0813156393	-0.318391404	0.481022683	0.9999983
thick:p16-thick:p14	-0.3284302567	-0.653797402	-0.003063112	0.0450936
cont:p17-thick:p14	NA	NA	NA	NA
fine:p17-thick:p14	-0.2420065617	-0.675500433	0.191487310	0.8697338
mid:p17-thick:p14	-0.2400482342	-0.646335784	0.166239315	0.8109178
thick:p17-thick:p14	-0.3901060832	-0.736874428	-0.043337738	0.0112618
fine:p16-cont:p16	-0.6453749319	-1.313107442	0.022357578	0.0712914
mid:p16-cont:p16	0.0291260715	-0.357666723	0.415918866	1.0000000
thick:p16-cont:p16	-0.3806198245	-0.689984858	-0.071254791	0.0026588
cont:p17-cont:p16	NA	NA	NA	NA
fine:p17-cont:p16	-0.2941961295	-0.715811929	0.127419670	0.5534458
mid:p17-cont:p16	-0.2922378020	-0.685827078	0.101351474	0.4378373
thick:p17-cont:p16	-0.4422956510	-0.774095637	-0.110495665	0.0005604
mid:p16-fine:p16	0.6745010034	-0.060505968	1.409507974	0.1153267
thick:p16-fine:p16	0.2647551073	-0.432620908	0.962131122	0.9958928
cont:p17-fine:p16	NA	NA	NA	NA
fine:p17-fine:p16	0.3511788023	-0.402735294	1.105092898	0.9691203
mid:p17-fine:p16	0.3531371299	-0.385469057	1.091743317	0.9611665
thick:p17-fine:p16	0.2030792809	-0.504534888	0.910693450	0.9998419
thick:p16-mid:p16	-0.4097458960	-0.845722119	0.026230327	0.0932275
cont:p17-mid:p16	NA	NA	NA	NA
fine:p17-mid:p16	-0.3233222010	-0.844981501	0.198337099	0.7489619
mid:p17-mid:p16	-0.3213638735	-0.820644417	0.177916670	0.6924152
thick:p17-mid:p16	-0.4714217225	-0.923594005	-0.019249440	0.0309685
cont:p17-thick:p16	NA	NA	NA	NA
fine:p17-thick:p16	0.0864236950	-0.380723480	0.553570870	0.9999995
mid:p17-thick:p16	0.0883820225	-0.353635081	0.530399126	0.9999986
thick:p17-thick:p16	-0.0616758265	-0.449693651	0.326341998	0.9999999
fine:p17-cont:p17	NA	NA	NA	NA
mid:p17-cont:p17	NA	NA	NA	NA
thick:p17-cont:p17	NA	NA	NA	NA
mid:p17-fine:p17	0.0019583275	-0.524760077	0.528676732	1.0000000
thick:p17-fine:p17	-0.1480995215	-0.630397137	0.334198094	0.9996376
thick:p17-mid:p17	-0.1500578490	-0.608057440	0.307941742	0.9992158

B. Preliminary multivariate ANOVA of primary electrospinning parameters against log-transformed fibre diameters

	Df	Sum Sq	Mean Sq	F value	Pr(>F)	
temp	1	158	157.9	484.226	< 2e-16	***
humidity	1	153	153.3	470.396	< 2e-16	***
DCM.x.mol	1	260	260.3	798.381	< 2e-16	***
chloro.x.mol	1	1084	1084.4	3326.397	< 2e-16	***
needle.bore	1	50	50.3	154.280	< 2e-16	***
needle.length	1	4	4.4	13.388	0.000255	***
flow.rate	1	445	444.9	1364.692	< 2e-16	***
voltage	1	36	36.2	111.070	< 2e-16	***
y	1	181	180.9	555.076	< 2e-16	***
temp:humidity	1	67	66.6	204.280	< 2e-16	***
temp:DCM.x.mol	1	5	5.0	15.450	8.53E-05	***
humidity:DCM.x.mol	1	47	46.7	143.268	< 2e-16	***
temp:chloro.x.mol	1	27	26.9	82.427	< 2e-16	***
humidity:chloro.x.mol	1	40	40.3	123.645	< 2e-16	***
DCM.x.mol:chloro.x.mol	1	106	105.8	324.641	< 2e-16	***
DCM.x.mol:PCL.x.mol	1	26	26.2	80.482	< 2e-16	***
chloro.x.mol:PCL.x.mol	1	45	44.9	137.627	< 2e-16	***
temp:needle.bore	1	36	36.2	110.962	< 2e-16	***
humidity:needle.bore	1	0	0.2	0.576	0.447822	
DCM.x.mol:needle.bore	1	31	31.0	95.181	< 2e-16	***
chloro.x.mol:needle.bore	1	34	33.9	103.974	< 2e-16	***
temp:needle.length	1	1	0.5	1.587	0.20773	
humidity:needle.length	1	5	5.0	15.348	9.00E-05	***
needle.bore:needle.length	1	1	0.7	2.190	0.138963	
temp:flow.rate	1	18	18.4	56.575	5.88E-14	***
humidity:flow.rate	1	6	5.8	17.939	2.30E-05	***
DCM.x.mol:flow.rate	1	0	0.0	0.000	0.991895	
chloro.x.mol:flow.rate	1	0	0.2	0.765	0.381927	
needle.bore:flow.rate	1	4	3.6	11.050	0.00089	***
temp:voltage	1	1	0.9	2.624	0.105268	
humidity:voltage	1	3	3.0	9.274	0.002331	**
DCM.x.mol:voltage	1	10	9.5	29.253	6.50E-08	***
chloro.x.mol:voltage	1	3	3.3	10.139	0.001456	**
needle.bore:voltage	1	1	1.0	2.935	0.086732	.
flow.rate:voltage	1	1	0.7	2.233	0.135089	
temp:y	1	6	5.6	17.236	3.33E-05	***
humidity:y	1	6	5.6	17.044	3.68E-05	***
DCM.x.mol:y	1	0	0.0	0.050	0.823704	
chloro.x.mol:y	1	27	26.7	81.878	< 2e-16	***
needle.bore:y	1	43	43.5	133.333	< 2e-16	***
flow.rate:y	1	3	3.3	10.013	0.001559	**
voltage:y	1	8	7.8	24.058	9.50E-07	***
temp:humidity:DCM.x.mol	1	7	6.6	20.333	6.58E-06	***
temp:humidity:chloro.x.mol	1	4	3.6	10.966	0.000931	***
temp:DCM.x.mol:chloro.x.mol	1	17	17.2	52.902	3.77E-13	***
humidity:DCM.x.mol:chloro.x.mol	1	4	3.6	11.122	0.000856	***
temp:DCM.x.mol:PCL.x.mol	1	0	0.1	0.402	0.525933	
humidity:DCM.x.mol:PCL.x.mol	1	23	22.5	69.103	< 2e-16	***
temp:chloro.x.mol:PCL.x.mol	1	0	0.2	0.536	0.463964	
humidity:chloro.x.mol:PCL.x.mol	1	3	3.4	10.439	0.001238	**
temp:DCM.x.mol:needle.bore	1	0	0.2	0.531	0.466076	
temp:chloro.x.mol:needle.bore	1	1	0.6	1.904	0.167673	
DCM.x.mol:chloro.x.mol:needle.bore	1	0	0.1	0.247	0.618981	
temp:PCL.x.mol:needle.bore	1	4	3.5	10.738	0.001053	**
chloro.x.mol:PCL.x.mol:needle.bore	1	0	0.0	0.056	0.812511	
temp:DCM.x.mol:needle.length	1	0	0.1	0.367	0.544746	
temp:PCL.x.mol:needle.length	1	0	0.1	0.287	0.592451	
temp:humidity:flow.rate	1	3	3.3	10.118	0.001473	**
temp:DCM.x.mol:flow.rate	1	11	11.3	34.777	3.82E-09	***
humidity:DCM.x.mol:flow.rate	1	1	1.2	3.817	0.050774	.
DCM.x.mol:chloro.x.mol:flow.rate	1	28	28.4	87.064	< 2e-16	***
temp:PCL.x.mol:flow.rate	1	3	2.8	8.724	0.003147	**
humidity:PCL.x.mol:flow.rate	1	0	0.0	0.043	0.836061	
DCM.x.mol:PCL.x.mol:flow.rate	1	0	0.0	0.005	0.944834	
temp:humidity:voltage	1	2	1.7	5.267	0.02175	*
temp:DCM.x.mol:voltage	1	3	2.9	8.984	0.002731	**
humidity:DCM.x.mol:voltage	1	39	38.5	118.221	< 2e-16	***
humidity:PCL.x.mol:voltage	1	3	3.2	9.792	0.001758	**
temp:needle.bore:voltage	1	0	0.1	0.306	0.580055	
chloro.x.mol:needle.bore:voltage	1	3	2.7	8.199	0.0042	**
PCL.x.mol:needle.bore:voltage	1	2	2.2	6.824	0.009009	**
temp:needle.length:voltage	1	1	1.1	3.326	0.068243	.
chloro.x.mol:needle.length:voltage	1	0	0.1	0.201	0.653529	
temp:flow.rate:voltage	1	14	14.2	43.712	4.00E-11	***
humidity:flow.rate:voltage	1	1	1.3	3.934	0.047348	*
chloro.x.mol:flow.rate:voltage	1	0	0.0	0.027	0.869056	
temp:humidity:y	1	0	0.0	0.042	0.837831	
humidity:DCM.x.mol:y	1	0	0.5	1.413	0.234553	
humidity:chloro.x.mol:y	1	21	20.7	63.364	1.91E-15	***
DCM.x.mol:chloro.x.mol:y	1	8	7.8	23.826	1.07E-06	***
humidity:PCL.x.mol:y	1	0	0.1	0.383	0.536249	
chloro.x.mol:PCL.x.mol:y	1	3	3.4	10.381	0.001277	**
temp:flow.rate:y	1	5	5.1	15.677	7.57E-05	***
humidity:flow.rate:y	1	0	0.0	0.107	0.74346	
chloro.x.mol:flow.rate:y	1	1	1.0	2.929	0.087058	.
temp:voltage:y	1	0	0.0	0.005	0.945375	
DCM.x.mol:voltage:y	1	0	0.1	0.303	0.58232	

PCL.x.mol:voltage:y	1	1	0.9	2.846	0.091649	.
temp:humidity:DCM.x.mol:needle.bore	1	0	0.4	1.199	0.273604	
temp:humidity:chloro.x.mol:needle.bore	1	0	0.0	0.030	0.861728	
temp:DCM.x.mol:chloro.x.mol:needle.bore	1	1	0.7	2.182	0.139625	
temp:humidity:PCL.x.mol:needle.bore	1	0	0.5	1.448	0.228905	
temp:DCM.x.mol:PCL.x.mol:needle.bore	1	0	0.2	0.581	0.445769	
temp:chloro.x.mol:PCL.x.mol:needle.bore	1	0	0.0	0.114	0.735586	
humidity:chloro.x.mol:PCL.x.mol:needle.bore	1	0	0.3	0.982	0.321732	
humidity:DCM.x.mol:chloro.x.mol:needle.length	1	0	0.3	0.941	0.33204	
humidity:DCM.x.mol:PCL.x.mol:needle.length	1	0	0.0	0.071	0.790343	
temp:chloro.x.mol:PCL.x.mol:needle.length	1	0	0.1	0.441	0.506526	
humidity:chloro.x.mol:PCL.x.mol:needle.length	1	0	0.1	0.170	0.680139	
chloro.x.mol:PCL.x.mol:needle.bore:needle.length	1	1	1.0	3.040	0.081242	.
temp:humidity:chloro.x.mol:flow.rate	1	0	0.4	1.359	0.243752	
temp:DCM.x.mol:chloro.x.mol:flow.rate	1	3	3.3	10.081	0.001503	**
temp:humidity:PCL.x.mol:flow.rate	1	0	0.3	0.905	0.341573	
temp:chloro.x.mol:PCL.x.mol:flow.rate	1	0	0.1	0.373	0.541426	
DCM.x.mol:chloro.x.mol:PCL.x.mol:flow.rate	1	0	0.2	0.649	0.420561	
DCM.x.mol:chloro.x.mol:needle.bore:flow.rate	1	1	0.7	2.194	0.138598	
temp:PCL.x.mol:needle.bore:flow.rate	1	0	0.0	0.009	0.923682	
DCM.x.mol:PCL.x.mol:needle.bore:flow.rate	1	0	0.1	0.235	0.627566	
temp:DCM.x.mol:needle.length:flow.rate	1	1	0.5	1.575	0.20949	
humidity:DCM.x.mol:needle.length:flow.rate	1	0	0.0	0.110	0.740421	
DCM.x.mol:chloro.x.mol:needle.length:flow.rate	1	2	1.7	5.272	0.021688	*
temp:PCL.x.mol:needle.length:flow.rate	1	1	0.9	2.641	0.104202	
temp:humidity:DCM.x.mol:voltage	1	0	0.4	1.178	0.277886	
temp:humidity:chloro.x.mol:voltage	1	0	0.1	0.316	0.5739	
humidity:DCM.x.mol:chloro.x.mol:voltage	1	1	0.9	2.784	0.095255	.
DCM.x.mol:chloro.x.mol:needle.bore:voltage	1	1	0.5	1.655	0.198283	
DCM.x.mol:PCL.x.mol:needle.bore:voltage	1	0	0.0	0.114	0.73516	
chloro.x.mol:PCL.x.mol:needle.bore:voltage	1	0	0.1	0.347	0.55556	
temp:humidity:needle.length:voltage	1	0	0.0	0.120	0.729224	
humidity:DCM.x.mol:needle.length:voltage	1	0	0.0	0.016	0.90077	
temp:chloro.x.mol:needle.length:voltage	1	0	0.0	0.114	0.736178	
DCM.x.mol:chloro.x.mol:needle.length:voltage	1	0	0.1	0.341	0.559208	
temp:PCL.x.mol:needle.length:voltage	1	1	0.9	2.612	0.10611	
DCM.x.mol:PCL.x.mol:needle.length:voltage	1	0	0.0	0.082	0.774691	
temp:humidity:flow.rate:voltage	1	2	2.1	6.348	0.011767	*
temp:DCM.x.mol:flow.rate:voltage	1	0	0.1	0.356	0.550813	
temp:PCL.x.mol:flow.rate:voltage	1	2	2.1	6.367	0.011643	*
humidity:PCL.x.mol:flow.rate:voltage	1	0	0.0	0.000	0.999514	
DCM.x.mol:PCL.x.mol:flow.rate:voltage	1	0	0.0	0.040	0.841037	
chloro.x.mol:needle.bore:flow.rate:voltage	1	0	0.3	0.853	0.355589	
temp:needle.length:flow.rate:voltage	1	0	0.3	0.834	0.361265	
chloro.x.mol:needle.length:flow.rate:voltage	1	5	4.9	14.946	0.000111	***
needle.bore:needle.length:flow.rate:voltage	1	0	0.0	0.055	0.814572	
temp:humidity:DCM.x.mol:y	1	4	3.9	11.814	0.00059	***
humidity:DCM.x.mol:chloro.x.mol:y	1	1	1.1	3.344	0.067482	.
DCM.x.mol:chloro.x.mol:PCL.x.mol:Scaffold$y	1	2	2.2	6.760	0.009336	**
temp:humidity:needle.bore:y	1	3	3.1	9.525	0.002033	**
chloro.x.mol:PCL.x.mol:needle.bore:y	1	0	0.3	0.897	0.343603	
temp:DCM.x.mol:needle.length:y	1	3	3.0	9.262	0.002346	**
DCM.x.mol:chloro.x.mol:needle.length:y	1	1	0.6	1.919	0.165985	
temp:humidity:flow.rate:y	1	8	8.2	25.136	5.44E-07	***
humidity:DCM.x.mol:flow.rate:y	1	0	0.1	0.251	0.616298	
temp:chloro.x.mol:flow.rate:y	1	0	0.4	1.135	0.286684	
temp:needle.bore:flow.rate:y	1	0	0.0	0.047	0.828958	
temp:needle.length:flow.rate:y	1	1	0.7	2.138	0.143716	
DCM.x.mol:needle.length:flow.rate:y	1	2	1.6	4.925	0.026493	*
needle.bore:needle.length:flow.rate:y	1	0	0.0	0.075	0.783991	
temp:DCM.x.mol:voltage:y	1	1	0.9	2.838	0.092086	.
temp:PCL.x.mol:voltage:y	1	0	0.1	0.334	0.563564	
chloro.x.mol:PCL.x.mol:voltage:y	1	0	0.4	1.145	0.284705	
temp:needle.length:voltage:y	1	0	0.1	0.235	0.628082	
chloro.x.mol:flow.rate:voltage:y	1	3	2.8	8.626	0.003322	**
needle.length:flow.rate:voltage:y	1	0	0.1	0.292	0.588999	
temp:humidity:DCM.x.mol:chloro.x.mol:PCL.x.mol	1	0	0.0	0.031	0.860002	
temp:humidity:DCM.x.mol:PCL.x.mol:needle.bore	1	0	0.0	0.095	0.757889	
temp:DCM.x.mol:chloro.x.mol:PCL.x.mol:needle.length	1	0	0.0	0.053	0.817923	
temp:DCM.x.mol:chloro.x.mol:needle.bore:needle.length	1	1	1.3	3.936	0.047299	*
temp:chloro.x.mol:PCL.x.mol:needle.bore:needle.length	1	0	0.0	0.017	0.89619	
humidity:chloro.x.mol:PCL.x.mol:needle.bore:needle.length	1	0	0.1	0.331	0.564968	
temp:humidity:DCM.x.mol:chloro.x.mol:flow.rate	1	0	0.4	1.287	0.256714	
temp:humidity:DCM.x.mol:PCL.x.mol:flow.rate	1	3	3.2	9.939	0.001623	**
temp:humidity:chloro.x.mol:PCL.x.mol:flow.rate	1	3	2.7	8.369	0.003826	**
temp:DCM.x.mol:chloro.x.mol:PCL.x.mol:flow.rate	1	3	2.5	7.819	0.005179	**
humidity:DCM.x.mol:chloro.x.mol:needle.bore:flow.rate	1	0	0.0	0.058	0.809695	
humidity:DCM.x.mol:PCL.x.mol:needle.bore:flow.rate	1	1	0.7	2.064	0.15089	
temp:chloro.x.mol:PCL.x.mol:needle.bore:flow.rate	1	0	0.1	0.257	0.612081	
temp:humidity:DCM.x.mol:needle.length:flow.rate	1	1	0.6	1.856	0.173128	
temp:DCM.x.mol:chloro.x.mol:needle.length:flow.rate	1	0	0.1	0.313	0.576052	
temp:humidity:PCL.x.mol:needle.length:flow.rate	1	1	0.9	2.636	0.104517	
temp:DCM.x.mol:PCL.x.mol:needle.length:flow.rate	1	0	0.0	0.027	0.869471	
temp:chloro.x.mol:PCL.x.mol:needle.length:flow.rate	1	0	0.3	1.056	0.304098	
humidity:DCM.x.mol:needle.bore:needle.length:flow.rate	1	2	2.4	7.211	0.00726	**
temp:chloro.x.mol:needle.bore:needle.length:flow.rate	1	3	2.8	8.488	0.003582	**
DCM.x.mol:chloro.x.mol:needle.bore:needle.length:flow.rate	1	2	2.1	6.527	0.010639	*
temp:PCL.x.mol:needle.bore:needle.length:flow.rate	1	1	0.9	2.903	0.088424	.
DCM.x.mol:PCL.x.mol:needle.bore:needle.length:flow.rate	1	0	0.0	0.020	0.886909	
temp:humidity:chloro.x.mol:PCL.x.mol:voltage	1	1	1.1	3.499	0.061422	.
temp:DCM.x.mol:chloro.x.mol:PCL.x.mol:voltage	1	6	5.5	16.892	3.99E-05	***
temp:humidity:DCM.x.mol:needle.bore:voltage	1	1	0.7	2.070	0.150207	
temp:humidity:chloro.x.mol:needle.bore:voltage	1	0	0.3	0.956	0.328114	
temp:DCM.x.mol:chloro.x.mol:needle.bore:voltage	1	0	0.2	0.656	0.417922	
temp:DCM.x.mol:PCL.x.mol:needle.bore:voltage	1	1	1.2	3.794	0.051465	.

temp:humidity:chloro.x.mol:needle.length:voltage	1	2	1.9	5.831	0.015767	*
temp:DCM.x.mol:PCL.x.mol:needle.length:voltage	1	0	0.0	0.021	0.885352	
humidity:DCM.x.mol:PCL.x.mol:needle.length:voltage	1	1	0.5	1.613	0.204086	
temp:chloro.x.mol:PCL.x.mol:needle.length:voltage	1	0	0.3	0.815	0.366783	
humidity:chloro.x.mol:PCL.x.mol:needle.length:voltage	1	0	0.1	0.320	0.571753	
temp:humidity:needle.bore:needle.length:voltage	1	0	0.1	0.155	0.693507	
DCM.x.mol:chloro.x.mol:needle.bore:needle.length:voltage	1	0	0.0	0.016	0.900171	
temp:humidity:DCM.x.mol:flow.rate:voltage	1	0	0.2	0.655	0.418199	
humidity:DCM.x.mol:chloro.x.mol:flow.rate:voltage	1	0	0.1	0.174	0.676245	
humidity:chloro.x.mol:PCL.x.mol:flow.rate:voltage	1	0	0.1	0.174	0.676443	
DCM.x.mol:chloro.x.mol:PCL.x.mol:flow.rate:voltage	1	0	0.5	1.509	0.219394	
humidity:DCM.x.mol:needle.bore:flow.rate:voltage	1	0	0.0	0.055	0.814043	
temp:chloro.x.mol:needle.bore:flow.rate:voltage	1	0	0.0	0.073	0.786319	
temp:DCM.x.mol:needle.length:flow.rate:voltage	1	0	0.1	0.253	0.614998	
temp:chloro.x.mol:needle.length:flow.rate:voltage	1	0	0.4	1.284	0.257169	
DCM.x.mol:chloro.x.mol:needle.length:flow.rate:voltage	1	0	0.0	0.109	0.740951	
humidity:PCL.x.mol:needle.length:flow.rate:voltage	1	0	0.4	1.303	0.253748	
DCM.x.mol:PCL.x.mol:needle.length:flow.rate:voltage	1	2	2.0	6.018	0.014179	*
DCM.x.mol:needle.bore:needle.length:flow.rate:voltage	1	1	0.6	1.773	0.183085	
PCL.x.mol:needle.bore:needle.length:flow.rate:voltage	1	0	0.1	0.396	0.529178	
temp:humidity:PCL.x.mol:needle.bore:y	1	0	0.1	0.296	0.586602	
temp:chloro.x.mol:PCL.x.mol:needle.bore:y	1	0	0.1	0.458	0.498805	
DCM.x.mol:chloro.x.mol:PCL.x.mol:needle.bore:y	1	0	0.0	0.016	0.898341	
temp:humidity:DCM.x.mol:needle.length:y	1	4	3.5	10.879	0.000976	***
temp:DCM.x.mol:chloro.x.mol:needle.length:y	1	1	1.4	4.311	0.037884	*
humidity:chloro.x.mol:PCL.x.mol:needle.length:y	1	1	0.5	1.600	0.205956	
temp:DCM.x.mol:needle.bore:needle.length:y	1	1	0.5	1.599	0.206087	
DCM.x.mol:chloro.x.mol:needle.bore:needle.length:y	1	1	1.1	3.476	0.06228	.
temp:chloro.x.mol:PCL.x.mol:flow.rate:y	1	1	1.4	4.211	0.040198	*
DCM.x.mol:chloro.x.mol:needle.bore:flow.rate:y	1	1	0.8	2.406	0.120891	
DCM.x.mol:PCL.x.mol:needle.bore:flow.rate:y	1	2	2.3	7.186	0.007359	**
chloro.x.mol:PCL.x.mol:needle.bore:flow.rate:y	1	5	5.2	15.965	6.50E-05	***
temp:DCM.x.mol:needle.length:flow.rate:y	1	1	1.4	4.364	0.036721	*
temp:PCL.x.mol:needle.length:flow.rate:y	1	0	0.0	0.141	0.707671	
chloro.x.mol:needle.bore:needle.length:flow.rate:y	1	0	0.2	0.477	0.489629	
temp:humidity:DCM.x.mol:voltage:y	1	2	2.4	7.500	0.00618	**
temp:DCM.x.mol:chloro.x.mol:voltage:y	1	1	1.5	4.478	0.034349	*
temp:humidity:PCL.x.mol:voltage:y	1	0	0.1	0.195	0.658453	
temp:DCM.x.mol:needle.bore:voltage:y	1	2	1.8	5.579	0.018198	*
temp:chloro.x.mol:needle.bore:voltage:y	1	0	0.0	0.000	0.99227	
DCM.x.mol:chloro.x.mol:needle.bore:voltage:y	1	0	0.0	0.054	0.816719	
chloro.x.mol:PCL.x.mol:needle.bore:voltage:y	1	0	0.0	0.013	0.908312	
humidity:DCM.x.mol:needle.length:voltage:y	1	2	2.1	6.304	0.012062	*
temp:chloro.x.mol:needle.length:voltage:y	1	0	0.1	0.280	0.596549	
DCM.x.mol:PCL.x.mol:needle.length:voltage:y	1	0	0.3	0.800	0.37126	
temp:needle.bore:needle.length:voltage:y	1	2	1.8	5.559	0.018401	*
DCM.x.mol:needle.bore:needle.length:voltage:y	1	0	0.2	0.579	0.44655	
chloro.x.mol:needle.bore:needle.length:voltage:y	1	0	0.2	0.760	0.383297	
PCL.x.mol:needle.bore:needle.length:voltage:y	1	0	0.2	0.553	0.457115	
temp:needle.bore:flow.rate:voltage:y	1	2	1.7	5.229	0.022234	*
chloro.x.mol:needle.bore:flow.rate:voltage:y	1	3	3.2	9.837	0.001716	**
temp:needle.length:flow.rate:voltage:y	1	6	6.3	19.206	1.19E-05	***
humidity:needle.length:flow.rate:voltage:y	1	0	0.0	0.151	0.69797	
chloro.x.mol:needle.length:flow.rate:voltage:y	1	0	0.2	0.481	0.487783	
needle.bore:needle.length:flow.rate:voltage:y	1	0	0.0	0.038	0.846304	
temp:humidity:DCM.x.mol:chloro.x.mol:PCL.x.mol:needle.bore	1	1	0.7	2.044	0.152859	
temp:humidity:DCM.x.mol:chloro.x.mol:PCL.x.mol:needle.length	1	0	0.2	0.540	0.462601	
temp:humidity:DCM.x.mol:chloro.x.mol:needle.bore:needle.length	1	0	0.4	1.352	0.244995	
temp:humidity:DCM.x.mol:PCL.x.mol:needle.bore:needle.length	1	0	0.2	0.501	0.479057	
humidity:DCM.x.mol:chloro.x.mol:PCL.x.mol:needle.bore:needle.length	1	0	0.0	0.081	0.775683	
temp:humidity:DCM.x.mol:chloro.x.mol:PCL.x.mol:flow.rate	1	0	0.0	0.141	0.707521	
temp:humidity:DCM.x.mol:chloro.x.mol:needle.bore:flow.rate	1	1	0.9	2.677	0.101858	
temp:humidity:DCM.x.mol:PCL.x.mol:needle.bore:flow.rate	1	0	0.3	1.000	0.317377	
temp:humidity:chloro.x.mol:PCL.x.mol:needle.bore:flow.rate	1	0	0.4	1.199	0.273503	
temp:humidity:DCM.x.mol:chloro.x.mol:needle.length:flow.rate	1	0	0.0	0.124	0.72485	
temp:humidity:DCM.x.mol:PCL.x.mol:needle.length:flow.rate	1	0	0.0	0.044	0.833567	
temp:humidity:chloro.x.mol:PCL.x.mol:needle.length:flow.rate	1	0	0.4	1.219	0.269672	
temp:humidity:chloro.x.mol:needle.bore:needle.length:flow.rate	1	0	0.1	0.346	0.556502	
temp:DCM.x.mol:PCL.x.mol:needle.bore:needle.length:flow.rate	1	1	1.3	4.121	0.042388	*
temp:humidity:DCM.x.mol:chloro.x.mol:needle.bore:voltage	1	2	2.0	5.993	0.01438	*
temp:humidity:DCM.x.mol:PCL.x.mol:needle.bore:voltage	1	2	1.7	5.100	0.023948	*
temp:humidity:chloro.x.mol:PCL.x.mol:needle.bore:voltage	1	0	0.2	0.614	0.433191	
humidity:DCM.x.mol:chloro.x.mol:PCL.x.mol:needle.bore:voltage	1	1	1.0	2.932	0.086851	.
temp:humidity:DCM.x.mol:PCL.x.mol:needle.length:voltage	1	0	0.0	0.046	0.830578	
temp:DCM.x.mol:chloro.x.mol:PCL.x.mol:needle.length:voltage	1	0	0.1	0.432	0.511221	
temp:humidity:chloro.x.mol:needle.bore:needle.length:voltage	1	1	1.0	3.138	0.076509	.
temp:DCM.x.mol:chloro.x.mol:needle.bore:needle.length:voltage	1	1	0.6	1.692	0.193381	
temp:humidity:PCL.x.mol:needle.bore:needle.length:voltage	1	0	0.3	0.818	0.365741	
temp:DCM.x.mol:PCL.x.mol:needle.bore:needle.length:voltage	1	0	0.0	0.038	0.845788	
temp:chloro.x.mol:PCL.x.mol:needle.bore:needle.length:voltage	1	0	0.0	0.080	0.776792	
humidity:chloro.x.mol:PCL.x.mol:needle.bore:needle.length:voltage	1	0	0.3	0.811	0.367988	
temp:humidity:chloro.x.mol:PCL.x.mol:flow.rate:voltage	1	2	2.1	6.446	0.011137	*
temp:DCM.x.mol:chloro.x.mol:PCL.x.mol:flow.rate:voltage	1	0	0.5	1.415	0.234297	
temp:humidity:chloro.x.mol:needle.bore:flow.rate:voltage	1	1	1.2	3.722	0.053714	.
humidity:DCM.x.mol:chloro.x.mol:needle.bore:flow.rate:voltage	1	2	1.5	4.662	0.030858	*
temp:humidity:PCL.x.mol:needle.bore:flow.rate:voltage	1	1	0.9	2.810	0.093724	.
humidity:chloro.x.mol:PCL.x.mol:needle.bore:flow.rate:voltage	1	0	0.1	0.316	0.573935	
DCM.x.mol:chloro.x.mol:PCL.x.mol:needle.bore:flow.rate:voltage	1	1	1.1	3.331	0.068022	.
temp:DCM.x.mol:chloro.x.mol:needle.length:flow.rate:voltage	1	3	2.5	7.682	0.005589	**
temp:DCM.x.mol:PCL.x.mol:needle.length:flow.rate:voltage	1	0	0.1	0.434	0.509914	
humidity:chloro.x.mol:PCL.x.mol:needle.length:flow.rate:voltage	1	1	1.0	3.031	0.081697	.
DCM.x.mol:chloro.x.mol:PCL.x.mol:needle.length:flow.rate:voltage	1	1	1.1	3.371	0.066402	.
temp:DCM.x.mol:needle.bore:needle.length:flow.rate:voltage	1	0	0.0	0.147	0.701424	
temp:chloro.x.mol:needle.bore:needle.length:flow.rate:voltage	1	0	0.0	0.095	0.758445	
temp:humidity:DCM.x.mol:chloro.x.mol:PCL.x.mol:y	1	0	0.1	0.318	0.572755	

temp:DCM.x.mol:chloro.x.mol:PCL.x.mol:needle.bore:y	1	0	0.1	0.242	0.622696	
temp:humidity:DCM.x.mol:chloro.x.mol:needle.length:y	1	1	0.5	1.641	0.200207	
temp:humidity:DCM.x.mol:PCL.x.mol:needle.length:y	1	3	2.5	7.791	0.00526	**
temp:DCM.x.mol:chloro.x.mol:PCL.x.mol:needle.length:y	1	1	1.1	3.231	0.072307	.
humidity:DCM.x.mol:chloro.x.mol:PCL.x.mol:needle.length:y	1	0	0.3	0.893	0.344641	
temp:humidity:PCL.x.mol:needle.bore:needle.length:y	1	0	0.0	0.007	0.933407	
temp:DCM.x.mol:PCL.x.mol:needle.bore:needle.length:y	1	1	0.7	2.213	0.136886	
temp:chloro.x.mol:PCL.x.mol:needle.bore:needle.length:y	1	0	0.0	0.010	0.921664	
humidity:chloro.x.mol:PCL.x.mol:needle.bore:needle.length:y	1	7	6.6	20.387	6.40E-06	***
DCM.x.mol:chloro.x.mol:PCL.x.mol:needle.bore:needle.length:y	1	0	0.1	0.330	0.565437	
temp:humidity:DCM.x.mol:PCL.x.mol:flow.rate:y	1	0	0.0	0.053	0.817452	
temp:DCM.x.mol:PCL.x.mol:needle.bore:flow.rate:y	1	1	0.8	2.393	0.121948	
temp:humidity:DCM.x.mol:needle.length:flow.rate:y	1	0	0.1	0.446	0.504345	
temp:chloro.x.mol:PCL.x.mol:needle.length:flow.rate:y	1	1	0.5	1.649	0.199059	
humidity:DCM.x.mol:needle.bore:needle.length:flow.rate:y	1	1	1.2	3.544	0.059798	.
humidity:PCL.x.mol:needle.bore:needle.length:flow.rate:y	1	1	0.5	2.584	0.2082	
DCM.x.mol:PCL.x.mol:needle.bore:needle.length:flow.rate:y	1	2	2.0	5.988	0.014418	*
chloro.x.mol:PCL.x.mol:needle.bore:needle.length:flow.rate:y	1	3	2.7	8.153	0.004309	**
temp:humidity:DCM.x.mol:PCL.x.mol:voltage:y	1	1	0.9	2.764	0.096445	.
temp:humidity:PCL.x.mol:needle.bore:voltage:y	1	1	1.0	2.956	0.085587	.
humidity:DCM.x.mol:PCL.x.mol:needle.bore:voltage:y	1	0	0.1	0.286	0.592878	
humidity:DCM.x.mol:PCL.x.mol:needle.length:voltage:y	1	0	0.3	0.824	0.364004	
DCM.x.mol:chloro.x.mol:PCL.x.mol:needle.length:voltage:y	1	1	1.2	3.662	0.055705	.
temp:DCM.x.mol:needle.bore:needle.length:voltage:y	1	1	0.5	1.572	0.21001	
chloro.x.mol:PCL.x.mol:needle.bore:needle.length:voltage:y	1	2	1.8	5.577	0.018219	*
temp:humidity:DCM.x.mol:flow.rate:voltage:y	1	1	0.9	2.700	0.100401	
temp:humidity:PCL.x.mol:flow.rate:voltage:y	1	5	5.3	16.265	5.55E-05	***
temp:humidity:needle.bore:flow.rate:voltage:y	1	0	0.1	0.389	0.532634	
temp:chloro.x.mol:needle.bore:flow.rate:voltage:y	1	1	0.7	2.085	0.14874	
humidity:DCM.x.mol:needle.length:flow.rate:voltage:y	1	1	0.9	2.737	0.098082	.
temp:chloro.x.mol:needle.length:flow.rate:voltage:y	1	3	3.0	9.263	0.002344	**
DCM.x.mol:chloro.x.mol:needle.length:flow.rate:voltage:Scaffold$y	1	0	0.0	0.009	0.924405	
DCM.x.mol:PCL.x.mol:needle.length:flow.rate:voltage:y	1	2	2.3	6.939	0.008446	**
chloro.x.mol:needle.bore:needle.length:flow.rate:voltage:y	1	4	3.6	10.927	0.000951	***
temp:humidity:DCM.x.mol:chloro.x.mol:PCL.x.mol:needle.bore:needle.length	1	0	0.3	0.802	0.370461	
temp:humidity:DCM.x.mol:chloro.x.mol:PCL.x.mol:needle.bore:flow.rate	1	0	0.4	1.123	0.289356	
temp:humidity:DCM.x.mol:chloro.x.mol:needle.bore:needle.length:flow.rate	1	0	0.3	0.835	0.360897	
temp:humidity:chloro.x.mol:PCL.x.mol:needle.bore:needle.length:flow.rate	1	1	0.8	2.406	0.12087	
temp:DCM.x.mol:chloro.x.mol:PCL.x.mol:needle.bore:needle.length:flow.rate	1	0	0.2	0.644	0.422407	
temp:DCM.x.mol:chloro.x.mol:PCL.x.mol:needle.bore:needle.length:voltage	1	3	3.5	10.736	0.001054	**
humidity:DCM.x.mol:chloro.x.mol:PCL.x.mol:needle.bore:needle.length:voltage	1	1	0.7	2.073	0.150083	
temp:humidity:chloro.x.mol:PCL.x.mol:needle.bore:flow.rate:voltage	1	1	0.6	1.936	0.164141	
humidity:DCM.x.mol:chloro.x.mol:PCL.x.mol:needle.bore:flow.rate:voltage	1	0	0.0	0.118	0.731716	
temp:humidity:DCM.x.mol:PCL.x.mol:needle.length:flow.rate:voltage	1	4	4.1	12.436	0.000423	***
temp:humidity:chloro.x.mol:PCL.x.mol:needle.length:flow.rate:voltage	1	1	0.8	2.496	0.114204	
humidity:chloro.x.mol:PCL.x.mol:needle.bore:needle.length:flow.rate:voltage	1	1	0.7	2.203	0.137737	
temp:humidity:DCM.x.mol:chloro.x.mol:PCL.x.mol:needle.bore:y	1	1	1.2	3.810	0.050973	.
temp:humidity:DCM.x.mol:chloro.x.mol:needle.bore:needle.length:y	1	1	0.6	1.753	0.18558	
temp:humidity:DCM.x.mol:PCL.x.mol:needle.bore:needle.length:y	1	0	0.2	0.603	0.437267	
humidity:DCM.x.mol:chloro.x.mol:PCL.x.mol:needle.bore:needle.length:y	1	0	0.2	0.701	0.402549	
temp:humidity:DCM.x.mol:needle.bore:needle.length:flow.rate:y	1	0	0.2	0.651	0.41964	
temp:DCM.x.mol:chloro.x.mol:needle.bore:needle.length:flow.rate:y	1	0	0.0	0.041	0.838718	
temp:humidity:PCL.x.mol:needle.bore:needle.length:flow.rate:y	1	6	5.5	16.875	4.02E-05	***
temp:DCM.x.mol:PCL.x.mol:needle.bore:needle.length:flow.rate:y	1	0	0.0	0.002	0.965381	
temp:chloro.x.mol:PCL.x.mol:needle.bore:needle.length:flow.rate:y	1	7	7.4	22.774	1.85E-06	***
temp:DCM.x.mol:chloro.x.mol:PCL.x.mol:needle.bore:voltage:y	1	0	0.4	1.159	0.281621	
temp:DCM.x.mol:chloro.x.mol:PCL.x.mol:needle.length:voltage:y	1	1	0.7	2.156	0.142037	
temp:DCM.x.mol:PCL.x.mol:needle.bore:needle.length:voltage:y	1	1	0.8	2.312	0.12839	
humidity:DCM.x.mol:PCL.x.mol:needle.bore:needle.length:voltage:y	1	0	0.0	0.004	0.950048	
temp:DCM.x.mol:chloro.x.mol:PCL.x.mol:flow.rate:voltage:y	1	1	1.2	3.827	0.050452	.
humidity:DCM.x.mol:chloro.x.mol:PCL.x.mol:flow.rate:voltage:y	1	0	0.2	0.688	0.406998	
temp:DCM.x.mol:chloro.x.mol:needle.bore:flow.rate:voltage:y	1	0	0.0	0.059	0.808142	
temp:chloro.x.mol:PCL.x.mol:needle.bore:flow.rate:voltage:y	1	0	0.1	0.172	0.67864	
temp:humidity:DCM.x.mol:needle.length:flow.rate:voltage:y	1	0	0.2	0.668	0.41368	
temp:humidity:PCL.x.mol:needle.length:flow.rate:voltage:y	1	3	2.7	8.385	0.003792	**
DCM.x.mol:PCL.x.mol:needle.bore:needle.length:flow.rate:voltage:y	1	0	0.3	0.799	0.371439	
temp:humidity:DCM.x.mol:chloro.x.mol:PCL.x.mol:needle.bore:needle.length:voltage	1	0	0.1	0.357	0.549956	
temp:humidity:chloro.x.mol:PCL.x.mol:needle.bore:needle.length:flow.rate:voltage	1	2	1.9	5.861	0.015449	*
temp:DCM.x.mol:chloro.x.mol:PCL.x.mol:needle.bore:needle.length:flow.rate:voltage	1	1	0.6	1.894	0.168783	
temp:DCM.x.mol:chloro.x.mol:PCL.x.mol:needle.bore:flow.rate:voltage:y	1	1	1.3	4.090	0.04316	*
temp:humidity:DCM.x.mol:needle.bore:needle.length:flow.rate:voltage:y	1	2	1.8	5.635	0.017629	*
temp:humidity:PCL.x.mol:needle.bore:needle.length:flow.rate:voltage:y	1	0	0.1	0.191	0.66201	
temp:DCM.x.mol:PCL.x.mol:needle.bore:needle.length:flow.rate:voltage:y	1	0	0.3	0.961	0.326899	
temp:chloro.x.mol:PCL.x.mol:needle.bore:needle.length:flow.rate:voltage:y	1	1	1.2	3.551	0.059527	.
DCM.x.mol:chloro.x.mol:PCL.x.mol:needle.bore:needle.length:flow.rate:voltage:y	1	1	0.9	2.748	0.097401	.
Residuals	9901	3228	0.3			

Signif. codes: 0 ‘***’ 0.001 ‘**’ 0.01 ‘*’ 0.05 ‘.’ 0.1 ‘ ’ 1

C. Multivariate ANOVA of greatest known reductions of electrospinning parameters

	Df	Sum Sq	Mean Sq	F value	Pr(>F)	
Scaffold$D.elect	1	3	2.9	7.661	0.00565	**
Scaffold$rho.q	1	1065	1064.6	2855.898	< 2e-16	***
Scaffold$Re	1	241	241.2	647.047	< 2e-16	***
Scaffold$y	1	583	583.2	1564.535	< 2e-16	***
Scaffold$P.diff	1	131	131.4	352.46	< 2e-16	***
Scaffold$D.elect:Scaffold$rho.q	1	8	7.6	20.276	6.78E-06	***
Scaffold$D.elect:Scaffold$Re	1	1	0.6	1.605	0.20521	
Scaffold$rho.q:Scaffold$Re	1	11	10.9	29.161	6.81E-08	***
Scaffold$D.elect:Scaffold$y	1	0	0.1	0.198	0.65659	
Scaffold$rho.q:Scaffold$y	1	126	125.6	337.023	< 2e-16	***
Scaffold$Re:Scaffold$y	1	21	20.7	55.568	9.76E-14	***
Scaffold$D.elect:Scaffold$P.diff	1	61	61.5	164.914	< 2e-16	***
Scaffold$rho.q:Scaffold$P.diff	1	268	268.3	719.657	< 2e-16	***
Scaffold$Re:Scaffold$P.diff	1	13	12.8	34.45	4.51E-09	***
Scaffold$y:Scaffold$P.diff	1	15	15.3	41.075	1.53E-10	***
Scaffold$D.elect:Scaffold$rho.q:Scaffold$Re	1	8	8.5	22.752	1.87E-06	***
Scaffold$D.elect:Scaffold$rho.q:Scaffold$y	1	31	30.7	82.373	< 2e-16	***
Scaffold$D.elect:Scaffold$Re:Scaffold$y	1	29	28.6	76.838	< 2e-16	***
Scaffold$rho.q:Scaffold$Re:Scaffold$y	1	47	46.9	125.801	< 2e-16	***
Scaffold$D.elect:Scaffold$rho.q:Scaffold$P.diff	1	1	1.3	3.563	0.05912	.
Scaffold$D.elect:Scaffold$Re:Scaffold$P.diff	1	1	0.7	1.848	0.17407	
Scaffold$rho.q:Scaffold$Re:Scaffold$P.diff	1	12	11.9	31.801	1.75E-08	***
Scaffold$D.elect:Scaffold$y:Scaffold$P.diff	1	25	25.5	68.358	< 2e-16	***
Scaffold$rho.q:Scaffold$y:Scaffold$P.diff	1	19	19.3	51.691	6.95E-13	***
Scaffold$Re:Scaffold$y:Scaffold$P.diff	1	19	18.9	50.782	1.10E-12	***
Scaffold$D.elect:Scaffold$rho.q:Scaffold$Re:Scaffold$y	1	7	6.8	18.345	1.86E-05	***
Scaffold$D.elect:Scaffold$rho.q:Scaffold$Re:Scaffold$P.diff	1	3	3.4	9.048	0.00264	**
Scaffold$D.elect:Scaffold$rho.q:Scaffold$y:Scaffold$P.diff	1	6	5.8	15.461	8.48E-05	***
Scaffold$D.elect:Scaffold$Re:Scaffold$y:Scaffold$P.diff	1	16	15.9	42.614	6.98E-11	***
Scaffold$rho.q:Scaffold$Re:Scaffold$y:Scaffold$P.diff	1	0	0.3	0.785	0.37555	
Scaffold$D.elect:Scaffold$rho.q:Scaffold$Re:Scaffold$y:Scaffold$P.diff	1	86	86	230.678	< 2e-16	***
Residuals 10222	3811	0.4				

Signif. codes: 0 ‘***’ 0.001 ‘**’ 0.01 ‘*’ 0.05 ‘.’ 0.1 ‘ ’ 1